A study of the dynamic performance of the multi-system involved in the offshore floating type wind turbine

This thesis is submitted for the degree of

Doctor of Philosophy

School of Mechanical and Mechatronic Engineering, FEIT

University of Technology Sydney, PO Box 123, Broadway, NSW 2007, Australia

Ph.D Candidate: Kan Ye

Supervisor: Jinchen Ji

Co-supervisor: Li Li

Year of submission: Spring 2018

This page intentionally left blank

Certificate of original authorship

I, Kan Ye declare that this thesis, submitted in fulfilment of the requirements for the award of Doctor of Philosophy, in the School of Mechanical and Mechatronic Systems, FEIT at the University of Technology Sydney. And this research is supported by the Australian Government Research Training Program.

I also certify that the thesis has been written by me. Any help that I have received in my research work and the preparation of the thesis itself has been acknowledged. In addition, I certify that all information sources and literature used are indicated in the thesis.

Signature of Student: Production Note:
Signature removed prior to publication.

Date: ***06/02/2019***

Acknowledgment

I would like to express my gratitude to all those who helped me during the journey of my Ph.D study. I gratefully acknowledge the help of my supervisor A/Prof Jinchen Ji, for all the support and encouragement he provided to me, during my entire Ph.D program. His constant guidance has walked me through all the stages of my Ph.D study. His encouragement and unwavering support has also sustained me through frustration and depression. Under his unselfish guidance, I am growing up to not only an eligible Ph.D student but a person of courage and honesty in life. I would also like to thank him for giving me the opportunity to participate in lecturing and tutoring during the period of my research, which has been a great experience to me, and I believe such experience would help my early academic career in many ways. Furthermore, I am grateful for the opportunity given by him to participate in an industry project (jointly supported by the Dept. of Industry, Innovation and Science), applying my knowledge and skills to solve real world problems.

I would also like to extend my sincere gratitude to my co-supervisor, A/Prof Li Li, for his instructive advice and useful suggestions on my research progress. I also owe a special debt of gratitude to all my good friends and colleagues from whose happiness shared with me in daily life and enlightening brainstorming in study I have benefited a lot.

Contents

Nomenclature

For Chapter 5

c	damping coefficient of the bearing
dr	displacement of the rotor
f_m	nonlinear unbalanced magnetic pull force
m, m_r, m_h, m_s	total mass of the rotor system, and masses of its three components
h	length of the air-gap
I	moment of inertia of the drive train system
I_p	polar moment of inertia of the rotating system
k	stiffness of the bearing
L	length of the shaft
l_i	distance from the centre of gravity to a specific position along the shaft
p	number of pole pairs of the generator
Δr	average air-gap between the rotor and stator
R_r	outer radius of the rotor
R_s	inner radius of the stator
S_s	linear current density in the stator

u_r	displacement of the centre of the rotor from its rotating axis
U_r	displacement of the centre of the stator from its rotating axis
x, y, θ_y, θ_x	displacements and rotating angles of the rotor system
μ	permeability of the magnet in the air-gap
Δe	relative eccentricity
β	angle between the principal axis and the direction of the unbalanced mass
ω	rotating speed of the rotor system
τ	skew angle of the rotor unbalanced mass

For Chapter 6

X, Y, Z	moving-local coordinate system (the rotor)
$y, z,$ θ_y, θ_z	displacements and rotating angles of the moving-local coordinate system
X', Y', Z'	fixed-global coordinate system (the platform)
$x', y',$ $\theta_x{}', \theta_y{}'$	displacements and rotating angles of the fixed-global coordinate system

m	total mass of the rotor system
L	length of the shaft
Rs	inner radius of the stator
Δr	average air-gap
h	length of the magnet
Ip	polar moment of inertia
I	moment of inertia
p	number of the pole pair
$l_{oo'}$	horizontal distance between the CG of the drive-train system and the CG of the platform
$h_{oo'}$	vertical distance between the CG of the drive-train system and the CG of the platform
$V_{(z)}$	mean wind speed at the altitude z
V_H	reference wind velocity at the reference altitude H (normally $H = 10$ m)
α	wind shear exponent ($\alpha = 0.11$)
F_w	drag force of fluids passing through structure
ρ_a	air density
$V_{r(z)}$	relative velocity of the wind and the structure

C_d	drag coefficient of the structure
$A_{(z)}$	equivalent characteristic surface area
$E(H_s)$	expected value of the significant wave height
$E(T_p)$	expected value of the peak period
$S_{\eta\eta}(\omega)$	JONSWAP spectrum
η	function of water surface elevation
γ	peak enhancement factor ($\gamma = 3.3$ for deep-sea)
ω_p	peak wave frequency
ω	circular wave frequency
T_m	mean wave period
T_z	zero-up-crossing wave period
T_p	peak period
$p(z,t)$	wave force acting on the structure at location z at time t
$f_{wave}(t)$	total wave force acting on the spar-support
d_w	water depth
z	vertical coordinate axis
C_m	inertia coefficient of the spar structure

d_e	equivalent characteristic diameter of spar-support
ρ_w	sea water density
k	wave number
λ	wave length
$v(z,t)$	horizontal velocity of the sea wave
$\dot{v}(z,t)$	acceleration of the sea wave
V_c	average current velocity of the sea wave
$F_c(z)$	force per unit length acting on the spar platform structure
$F_{buoyancy\_z'}$	buoyancy force acting on the structure in the z direction
$M_{buoyancy\_x'}$	buoyancy moment acting on the structure about the x direction
$M_{buoyancy\_y'}$	buoyancy moment acting on the structure about the y direction
l_{b-CG}	distance of the buoyancy force to the CG of the spar platform structure in the z direction
$F_{interaction\_z'}$	total interaction acting on the structure in the z direction
m'	total mass of the wind turbine including the nacelle
θ_{wc}	angle between the wind and the surge direction

For Chapter 7

$EI_{(z)}$	bending stiffness of the tower
$N_{(z)}$	normal force in the vertical direction
$m_{(z)}$	mass density per unit length of the tower
$r_{(z)}$	radius of gyration
$f_{(z,t)}$	resultant force of various loadings applied on the tower
ω_e	angular frequency
ω_n	nth natural frequency
$w_{(z)}$	displacement in the horizontal direction at the tower height z
$\dot{w}_{(z)}$	slope of the tower at the tower height z
k_1	torsion spring stiffness
α_1	rotating angle
L	tower length
D	tower average diameter
t	thickness
M_1	total mass of the platform
I_1	moment of inertia of the platform about its centre gravity (CG)

I_{01}	moment of inertial of the platform about the bottom end of the tower
g_1	distance between the CG of the platform to the bottom end of the tower structure
θ_1	fixed angle between the longitudinal axes of the platform and the undeformed tower
M_2	total mass of the nacelle
I_2	moment of inertia of the nacelle about its axis passing through its CG
I_{02}	moment of inertial of the nacelle about the top end of the tower
g_2	distance between the CG of the nacelle and the top end of the tower structure
$l_{oo'}$	horizontal distance between the CG of the nacelle and the top end of the tower structure
$h_{oo'}$	vertical distance between the CG of the nacelle and the top end of the tower structure
θ_2'	fixed angle between the rotating axis in the nacelle and the undeformed tower

List of figures

List of tables

Abstract

As the utilization of the renewable energy sources has significantly increased over the past decades, offshore wind turbines have been noted for their advantages of more power output and less space limitation than the onshore wind turbines. New prototypes of offshore wind turbines have been developed; not only has the power output been increased but also their sizes have become larger. However, the distinct offshore environmental loads may significantly affect the performances of the offshore wind turbine. The aims of this Ph.D research are to investigate the vibration behaviours of the multi-system involved in a spar type offshore direct-drive wind turbine. First of all, the overview of the main components involved in the offshore direct-drive wind turbine and their dynamic performances related to the mechanical vibration behaviour are presented. Different types of topology of the direct-drive wind turbines are briefly discussed and a comparison of all generator topologies is made based on the criteria of their efficiency, weight and cost. The supporting structures for the wind turbine have been developed from land to transitional-water, then the deep-water. Complex designs have been used to meet the environment requirements. Moreover, the consideration of the nacelle-blade system has been developed from a non-rotating mass to a rotating system with interaction when studying the tower response. The excitation conditions have become more complex. Not only the environmental excitations, such as the aerodynamics and hydrodynamic excitations should be considered, but also the internal excitations, such as the unbalanced magnetic pull force in the generator or tower shadow can be involved.

Three new models about the main components: direct-drive drive-train system, floating platform and the tower structure are presented in this thesis. To start with, the effect of

rotor position and weight adjustment on the vibration behaviour of the drive-train system within a 5 MW direct-drive wind turbine is studied by considering the unbalanced magnetic pull forces. The direct-drive wind turbine, different from the standard geared wind turbine, uses a direct-drive generator to avoid the gearbox failures, in which the direct-drive permanent-magnet generator has been widely used. The unbalanced magnetic pull (UMP) force which is caused by the eccentricity of both rotor and stator of the generator can have an impact on the vibration behaviour of its drive-train system, an up to 30% difference of the tolerance allowable for a safe operation in the generator can be found from the simulation results. The drive-train system which consists of the main shaft, rotor, hub and blades is modelled as a four degree-of-freedom (DOF) nonlinear system. In the present drive-train system, the location of its centre of gravity can be moved along its rotating axis by doing the rotor adjustment in terms of rotor position and mass ratio. Both rotor displacement and bearing forces are obtained for a wide range of rotor positions and weight under different rotating speeds. Such results would provide optimized rotor position and mass ratio to improve the performance of the drive-train system. Then a combined model of a spar-type floating platform wind turbine under deep-sea conditions is developed. The spar-type supporting platform with tower structure is modelled as a rigid body, while the nacelle is considered as a point mass attached on the top of the tower. Then the dynamic interaction between the drive-train system and the nacelle is considered by incorporating the modelling of the direct-drive drive-train system. The hydrodynamic and aerodynamic excitations on the structures are considered, including current, wave, and wind excitations as well as buoyant forces. With the help of the time history and FFT spectrum, the effects of both hydrodynamic and aerodynamic excitations along with the dynamic interaction between the drive-train system and tower structure on the

dynamic behaviour of the spar-type floating platform are investigated under different operating sea conditions. At last, the tower structure is developed using a flexible model. An analytic solution for the free-vibration of the tower structure based on Euler-Bernoulli beam-column theory is presented. The tower structure is modelled as a free-free beam with two end mass components. The platform and the nacelle are considered as two large mass rigid components connected by torsion springs at two tower ends. The stiffness at the connections can be different due to the different joint conditions between the tower and two mass components, such as joint type or crack. The effects of system parameters on the natural frequencies are investigated under a range of variables, including the tower structure parameters, platform and nacelle parameters, and the connecting types. Uniform tower model is presented firstly and then the non-uniform structure is discussed. The non-linear relationships between those variables and the natural frequency of the whole system are numerically found and some design issues are discussed for the spar-type floating wind turbines.

1. Introduction

As the utilization of the renewable energy sources has significantly increased over the past decades, new prototypes of the wind turbines have been developed to increase their power outputs. Over the last 40 years, the power yield of a single wind turbine has grown from 30kW to over 5 MW [1]. Constant speed wind turbines with power rated under 1.5MW were mostly used until the late 1990s. Then the variable speed wind turbines were developed as they could increase the power level and maximise the efficiency at all wind velocities by using control systems [2]. Both constant speed and variable speed wind turbines used a multistage gearbox to increase rotational speed for the generator [3-5]. Since 1991, gearless generator systems, or the so-called direct-drive wind turbines, have been recognized by the wind turbine manufacturers. A 5kW direct-drive generator wind turbine called "Torus" was designed by Spooner and Chalmers [6]. It was a slotless, toroidal-stator, double sided disc type, axial flux permanent magnet generator and was probably the largest one in such a configuration until 1998 [7]. Polinder *et al.* [3] listed five different generator systems and compared their costs and annual energy yields. The doubly-fed induction generator with three-stage gearbox (DFIG3G) was most widely used in wind turbines due to its lowest weight and cost; however it has high energy losses in the gearbox. The direct-drive synchronous generator with electrical excitation (DDSGEE) was the heaviest and most expensive one but Enercon, one of the largest wind turbine manufacturers, claimed the benefits of such a generator. The most attractive direct-drive generator would be the direct-drive permanent magnet generator (DDPMG), as it has a better torque density, higher energy yield, higher reliability, less constraint on the air-gap, and higher potential on cost optimization than the electrically-excited counterpart. Generally speaking, the direct-drive wind turbine, which is different from a standard geared wind turbine, has no gearbox used in the drive-train system to increase

the rotational speed, and thus has no gearbox failure and less failure in the brake [8]. It has greater reliability than the indirect-drive wind turbine due to its fewer rotating parts and wear components [9]. The main disadvantages of using the direct-drive generators in wind turbines are the cost and weight when compared with the geared wind turbines. Since most horizontal axis wind turbines operate in a small tip-speed ratio range (the ratio of the blade-tip speed to the wind speed) [10], the rotor system in a direct-drive generator rotates at a lower speed than the geared one when both types of wind turbines are exposed to the same wind speed. Thus the direct-drive wind turbines operating at the lower rotating speed require larger-scale generators than that of the geared one (which results in much heavier generators). However, given the fact that the increase of the generator's electricity power output is not linearly proportional to the increase of the size of the direct-drive generator, a further increase of the generator size seems not a viable and practical option [11]. On the other hand, a larger and heavier generator (or the whole wind turbine) means an increase of material, transportation, construction and maintenance costs. The construction, operation and maintenance costs for a wind turbine are about 10-15% of the total income in its life cycle, while for offshore wind turbines the cost could even reach 20-25% of the total income [12-14]. Moreover, although the wind energy is a renewable energy source with socioeconomic benefits, there are other environmental issues which should be considered while using wind turbines. Dai *et al.* [15] listed various environmental issues when building wind farms, such as impact on bats or birds, noise and visual impact, and discussed the mitigation strategies to improve the wind energy technologies.

The land-based wind turbines have been the world's fastest growing energy source on a percentage basis for over a decade. The interest in offshore wind turbines has been growing due to the limitation of land-based wind turbines and an abundant offshore wind

source. The advantages of installing offshore wind turbines include more power output (produced by higher wind speed and larger size of the generator), less limitation of land space and less complaints on the visual and noise annoyances near residential areas. The disadvantages of the offshore wind turbines are the higher capital investment on the support structure, maintenance and material cost. However, offshore environmental loads, which not only come from the wind but also from sea wave and current, can induce the vibrations of wind turbine structures. Excessive vibrations may produce variable stress, shorten the fatigue life of the structure and reduce the power output of the wind turbines [16-20].

1.1. Research objectives

The large offshore direct-drive wind turbines are subjected to not only the environmental excitations such as the aerodynamic and hydrodynamic excitations, but also the internal excitations such as the unbalanced magnetic pull force and the interactions between main subsystems, including tower-blade interaction (tower shadow effect) and tower-nacelle interactions. The consideration of the nacelle-blade system has been developed from a non-rotating mass to a rotating system with interaction when studying the tower response, so the excitation condition has become more complex. Not only the environmental excitations, such as the aerodynamics and hydrodynamic excitations should be considered, but also the internal excitations, such as the unbalanced magnetic pull force in the generator or tower shadow have to be taken into account. The aerodynamic and hydrodynamic excitations on offshore wind turbines are generated from wind, wave and sea current. The internal excitations include the tower-blade interaction, tower-nacelle (rotating system) interaction, and the UMP in the generator.

The overview of the multi-system within the wind turbines indicates the importance of the study on the vibration behaviour for such structures under the excessive excitations.

Thus, the objectives of the current research are to:

1) Investigate the vibration behaviour of the drive-train system in a large direct-drive wind turbine. The direct-drive drive-train has eliminated the gearbox to avoid failures, but this has also increased its structure size. The excitations, such as bearing forces and the magnetic pull force then should be included when studying the dynamic vibration of the system, with the consideration of changing its structural parameters, such as component position and weight. The obtained forces and moments within the system can not only provide useful information on the optimizations of its structure, but can also be considered as an interaction excitation to other systems involved in the wind turbine.
2) Study the dynamic response of a spar-type direct-drive wind turbine in an offshore environment. Both external and internal excitations are considered, where the external excitations are subjected to the environment loads and the internal excitations are subjected to the interactions between different systems. The deep-sea environment normally means higher wind speed and larger hydrodynamic excitations applied on the structure than onshore conditions. The performance of the wind turbine due to each excitation and the relationship between them can be an interesting and important topic during the designing or optimizing processes.
3) Investigate the optimizations of a spar-type offshore wind turbine tower structure. The natural frequency of the whole wind turbine and the mode shapes are studied for the entire system. Due to the increased size of the nacelle and support platform components, a new model for the tower structure is raised. The considerations at

the joint sections between the tower and other components are simple using torsional springs. Using a more complex structure connection, such as yaw bearing connections, or considering special conditions, such as corrosion crack, can be of interest for further study.

This research aims to develop a deep understanding of the excitations on the wind turbines. The proposed dynamic models can be used to study the multi-system involved in the wind turbine. The research results would provide information on how those excitations affect the wind turbines and useful information for the design of wind turbine structures.

1.2. Thesis outline

Chapter 1 introduces the background and challenges of the wind turbine, and presents the objectives of the current Ph.D research.

Chapter 2 discusses the multi-system involved in the wind turbines. In this chapter, the overview of the relevant researches on the main components involved in offshore direct-drive wind turbines (DDWT) and their dynamic performances is conducted. In the first part, different types of topology of the direct-drive wind turbines are briefly discussed, including the cooling system and condition monitoring system corresponding to the drive-train system, and the braking and bearing system involved in the nacelle. A brief introduction of the direct-drive generator used in wind turbines is given and a comparison of all generator topologies is made based on the criteria of their efficiency, weight and cost.

Chapter 3 presents the literature reviews regarding the development of all possible excitations on/in the wind turbine. The model for each excitation has been developed for a better simulation result. Constant-value models are normally used in the early stage, and then shaped model and stochastic component are applied in order to obtain a simulation result closer to the reality. However, the accuracy of the excitation model is normally conditionally considered as the high accuracy model requires a longer simulation time, but may lead to little difference.

Chapter 4 presents the previous studies on the dynamic effects of the excitations on the different systems of the wind turbine. The structure models of different components were developed according to their wind turbine types. Both mathematical method and finite element analysis (FEA) method were used. The main excitations related to this thesis due to the environment and within the drive-train system are listed.

Chapter 5 presents a new mathematical method of the drive-train system within a 5MW direct-drive wind turbine by considering the unbalanced magnetic pull force to study the effect of its rotor position and weight adjustment on the vibration behaviour. These adjustments can change the location of the centre of gravity of the drive-train system. The drive-train system, which consists of the main shaft, rotor, hub and blades is modelled as a four degree-of-freedom nonlinear system. Both rotor displacement and bearing forces are obtained. The simulation results would be variable for a wide range of rotor position and weight under different rotating speeds. The optimized rotor position and mass ratio would be helpful to improve the performance of the drive-train system.

Chapter 6 develops a new free-free end model for the wind turbine with a spar type floating platform under deep-sea conditions. The contributions of this section lie in two aspects: First of all, the effects of aerodynamic and hydrodynamic excitations on the spar

type direct-drive wind turbine structure are investigated by carrying out a series of time domain numerical simulations. The response of the platform system with the current induced only, the current and wave induced, and the current, wave and wind induced are compared to show the dominant effects under different types of excitation. The misalignment of the wind, wave and current directions is also considered to show its effect. Secondly, a dynamic model of the direct-drive drive-train system is incorporated into the dynamic model of the platform system to show the interaction effect between the drive-train system and the platform system along with the tower structure. The nacelle is considered as a point mass attached on the top of the tower firstly. Then, the dynamic interaction between the drive-train system and the nacelle is considered to form a combined model for the spar-type supporting platform wind turbine.

Chapter 7 constructs a new analytic solution of the free-vibration of a spar-type offshore wind turbine tower structure. The components at two ends of the tower, the platform and the nacelle, are no longer considered as mass points, their truly sizes and locations of the centre of gravity are used to describe the large mass components. A flexible tower structure is considered as a free-free beam tower connected to the end components by torsion springs at its ends. The torsional stiffness at the connecting locations of the platform and nacelle are different due to different physical requirements of supports. The natural frequencies of the tower structure are derived from the characteristic equation. The effects of system parameters on the natural frequencies are examined under a range of variables, including the tower structure parameters, platform and nacelle parameters, and connecting types. Some design issues related to the natural frequencies are discussed for the floating type wind turbines.

Chapter 8 gives the conclusion by summarising all findings and points the further research direction.

Chapter 9 presents the appendices which include more details of the data analysis and plots.

2. Multi-system involved in a wind turbine

A wind turbine usually consists of three main mechanical components; the nacelle, tower and the substructure (or say support structure or foundation), as shown in Figure 2-1. This section briefly discusses the main components involved in a wind turbine.

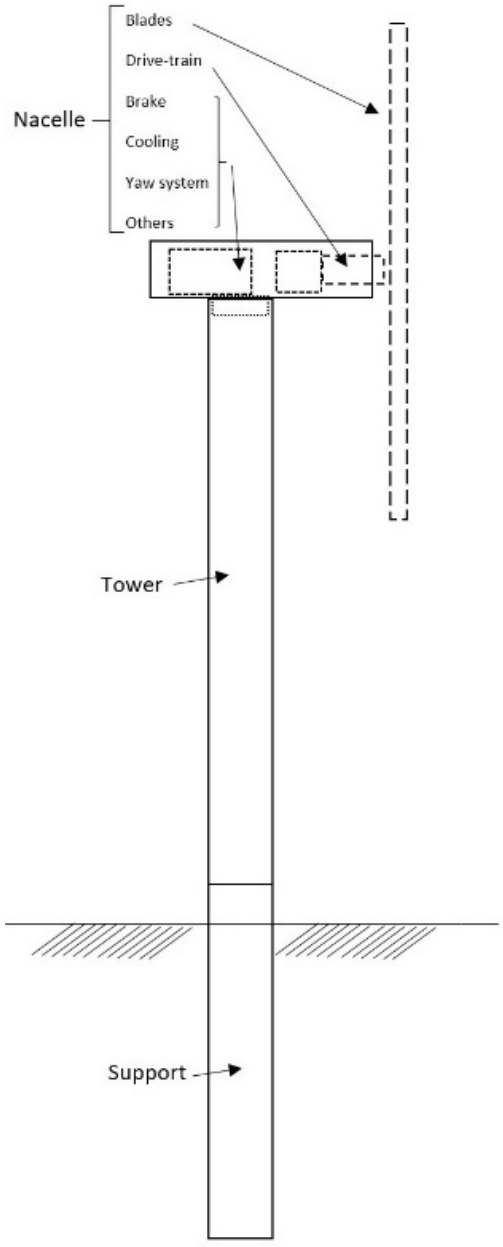

Figure 2-1 Main mechanical components of a wind turbine

2.1. Nacelle

A typical model of the nacelle is shown in Figure 2-2 , several important components have been involved. Blades and pitch control system are used to catch the wind and convert wind energy into the kinematic energy (torque). Drive-train system and the generator transform the kinematic energy into the electrical energy. The electrical power is then sent out to the grid through the converters and cables. The gearbox is used to meet the requirement of the generator but it can be eliminated while in a direct-drive wind turbine. Other subsystems, such as the condition monitoring and control system, cooling system, and brake system, are used to ensure the whole system to operate safely and sustainably.

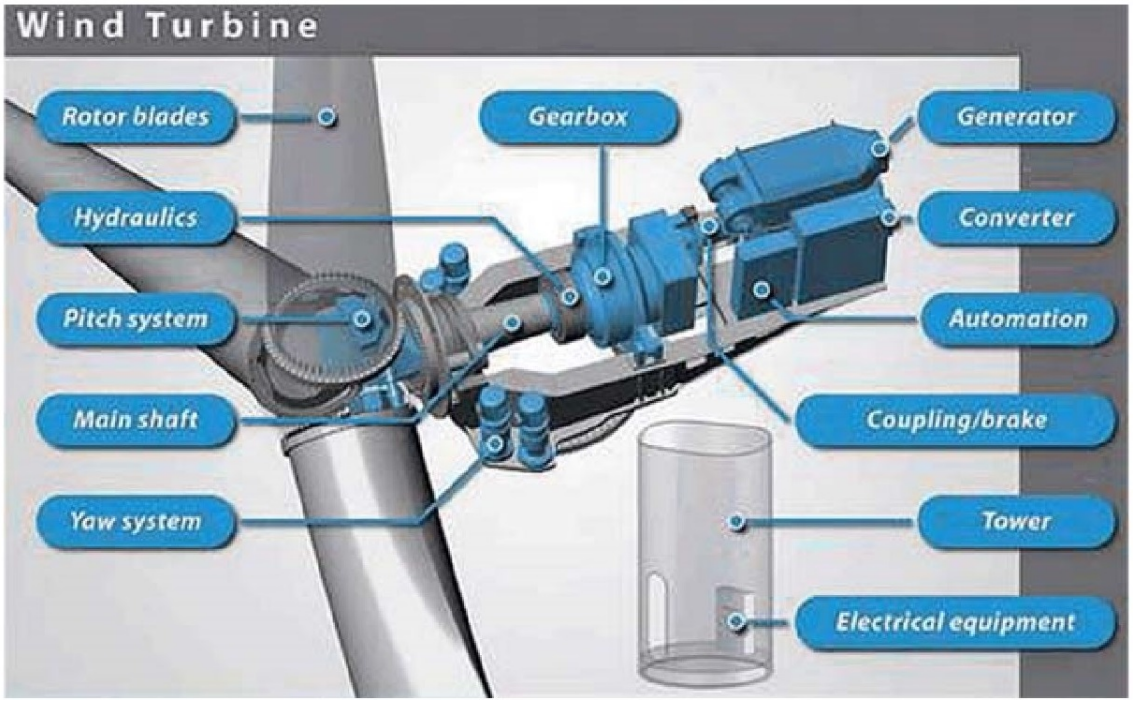

Figure 2-2 Typical model of the wind turbine nacelle [21]

When studying the vibration behaviour of wind turbine, the nacelle was first considered as a rigid non-rotating lumped mass placed on the top of the tower. Static and seismic loadings on the tower structure were considered to examine the effects of gravity,

aerodynamic conditions and possible site-dependent seismic motions [22, 23]. The finite element analysis showed that the natural frequency of the tower could increase as the blade rotating frequency increases [24-28]. The motion of the rotating parts, such as blades, was then recognised as important in studying the motion of the tower and the drive-train system within the nacelle, by developing a rotating model instead of the non-rotating mass attached on the top of the tower [29, 30]. A deep understanding of the dynamics of main subsystems involved in the nacelle is important for the dynamic behaviour of wind turbines.

2.1.1. Direct-drive generator and drive-train system

There are three basic topologies of direct-drive generators used in wind turbines namely; squirrel cage induction generator(SCIG), electrically excited synchronous generator(EESG) and permanent magnet synchronous generator(PMSG) [31], of which, PMSGs hold the largest market share [9].

In the early stage of the development of wind turbine at low power level, SCIG was widely used as a constant speed direct-drive generator. The main advantages of such a generator included low cost, robustness and high reliability [2, 32-35]. Even though nowadays DFIG or PMSG generators are used in MW-scale wind turbines, SCIG generator can still be a good solution in some cases, such as in an isolated power system [35]. However, the low generator speed range limits the applications of most of the SCIG, which can only be used in low power level direct-drive wind turbines or requires a small gearbox to meet the rotor speed [2, 32, 34]. Compared with a variable speed PMSG, it is more difficult to build a multipolar SCIG and the cost will increase [34].

The electrically excited synchronous generators can be either switched reluctance generators or with electrical excitation controls [36]. The largest variable-speed EESG wind turbine manufacturer, Enercon, produced their large commercial wind turbine with the power rate of 1.8 MW and developed a new prototype for 4.5 MW in 2002. However about 75% of their products was available only in German market and the concept was not widely represented until 2003 [36].

Compared with the electrically excited synchronous generator, the PMSG would be more suitable for a direct-drive wind turbine due to the advantage of less constraint on the air gap and higher reliability than the electric-excited counterparts [8, 37]. The PMSG machines have a better torque density than the EESG in a radial flux generator, however they are more difficult to assembly [38].

2.1.1.1. Flux type of the PMSGs

According to the flux type, the PMSG can be realised by three concepts; radial flux (RF), axial flux (AF) and transverse flux (TF) [39-42]. Given examples of different PMSGs are shown in Figure 2-3 to Figure 2-5.

Radial flux: From both economical consideration and design concept, a radial flux generator was a good choice for large direct-drive wind turbines [38, 40]. Leban *et al.* stated that radial flux and transverse flux PMSGs have greater optimising potential [43]. The common structure of the radial-flux consists of a cylindrical stator with coils and an internal cylindrical rotor with magnets. Its flux density in the air gap is required above an acceptable value, at least around 1T [40, 44, 45]. According to the rotor position, there are two types of rotor configurations; the inner rotor and the outer rotor. Normally an inner rotor machine would have a higher air gap flux density and better thermal management than the outer rotor type [9]. However, the inner rotor is heavier than the

outer rotor machine in terms of the active material weight [42]. Compared with an axial or transverse flux, the radial flux type has the advantages of a simpler structure, easier air-gap control and shorter load path [46].

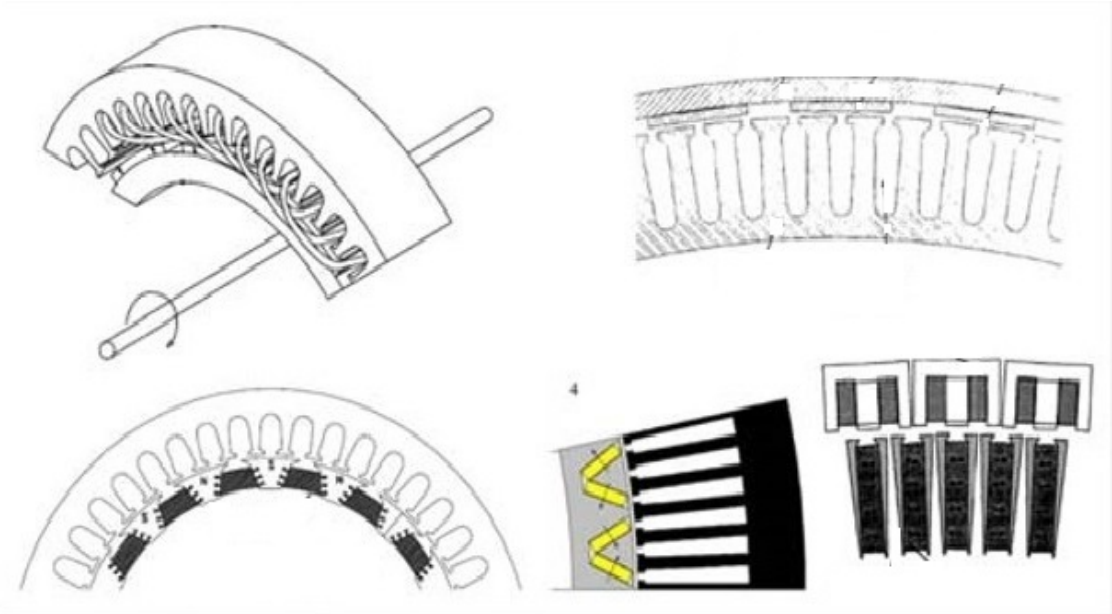

Figure 2-3 Examples of the RF PMSGs [42]

Axial flux: The common axial flux generator has a toroidal stator, an air gap winding and two rotor-disc with magnets [36]. Either by using a multiple disc machine to increase the flux density [42], or by using a different magnet arrangement [7, 36, 47] such as surface-mounted magnets with a large remanent flux density or embedded low cost ferrite magnets, can result in a larger total torque. The flux density in the air gap is normally easier to be controlled than that in a radial-flux design [10]. Compared with the RFPMs, the AFPMs have simpler winding and higher torque/volume ratio, but they are normally much heavier and more complicated in construction [42].

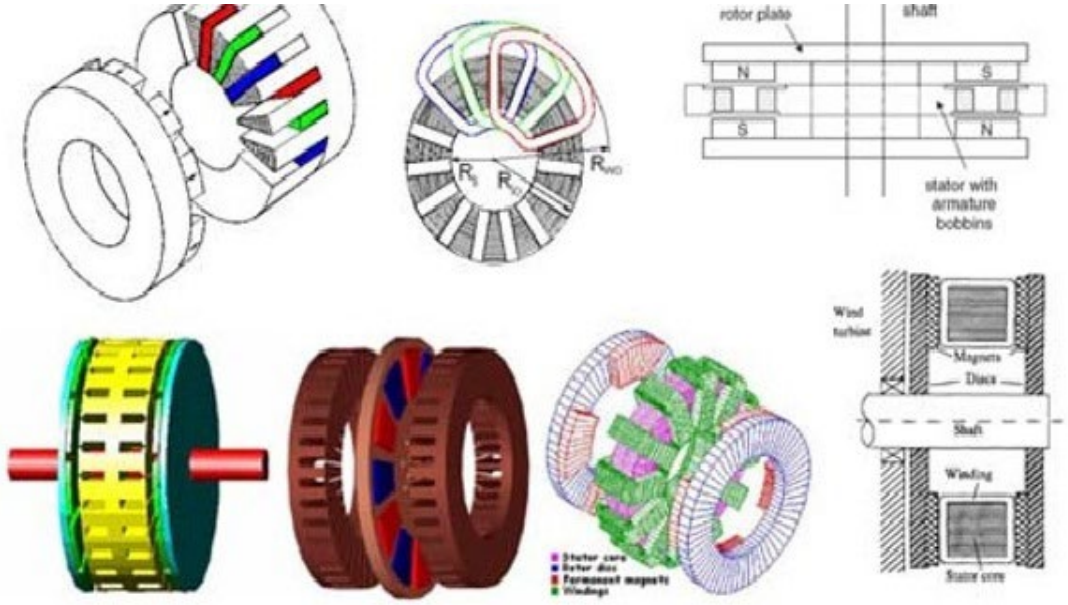

Figure 2-4 Examples of the AF PMSGs [42]

Transverse flux: The transverse flux can have the air gap type similar to either axial flux or radial flux [40, 44]. The main difference is that the transverse flux could increase the winding space while remaining the main flux space [36]. The flux path of the TFPM can be in three dimensions, which would lead to large air gaps and complicated constructions. For this reason, even TFPM has the advantages in high force density, low copper losses and simple winding, the disadvantages of complicated constructions and increased costs make it less attractive than the RFPM or AFPM [42].

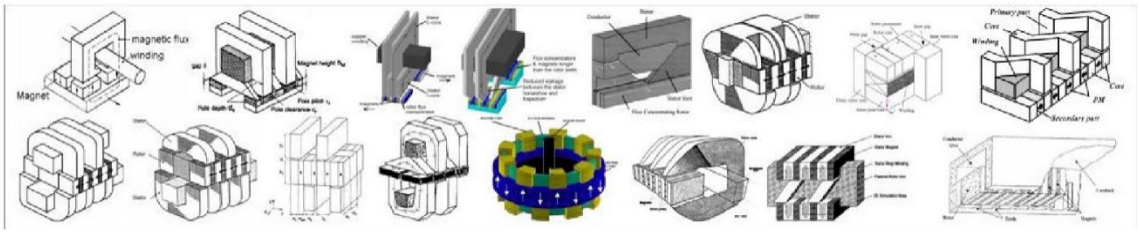

Figure 2-5 Examples of the TF PMSGs [42]

Not only is the permanent magnet used in the direct-drive generator, but also the ferrite magnet and rare earth PM are [42]. The use of magnets may be limited by the mounting

mode of the magnets. For either RF, AF or TF generator, magnets can be embedded or surface mounted. The embedded magnets, the so-called inset-PMs, or flux-concentrating magnetic circuits are placed inside the rotor construction and are able to concentrate the flux density in the air gap [36]. Thus the low cost ferrite magnet can be used. The inset-PM type can be slightly lighter than the surface mounted ones. When excited by surface-mounted magnets, the larger remanence flux density of the magnetic material is required than the flux density in the air gap, thus the low cost ferrite magnets cannot be used, more effective and expensive magnets should be chosen. The advantages of the surface mounted magnets are simpler and cheaper [40, 44]. The surface mounted permanent magnets (SMPMs) have the highest predicted efficiency, although they are heavier than the ferrite magnets in a transverse flux generator(TFFM) or rare earth PMs in a transverse flux generator(TFREPM) [10].

It seems to be an impossible task to compare the different topology generators since there are a number of criteria. Dubois *et al.* [31] made a comparison based on two criteria, the torque density and mass of the active material, which are possible for every topology. The power density of a given topology can be easily modified by only changing the rotational speed, thus the torque density is chosen as one of the criteria as it is independent of the rotational speed. For the same reason, instead of cost/power, the cost/torque can be the criteria for the comparison. From the practical experiences, The TFPM and AFIPM (axial flux interior permanent magnet) are the generators to meet the requirements of smaller machine diameters and lower material costs. A larger diameter of the generator would lead to a higher torque density and a lower cost/torque.

2.1.1.2. State-of-the-art of the generator

Since the use of direct-drive generator may lead to a heavy weight and high cost of a wind turbine, Shrestha *et al.* [48] proposed a new concept by using magnetic bearings to reduce the structural weight in 2010 and found that the structural weight can be reduced by 45% for a 5MW generator. In 2012, Paulsen *et al.* [49] investigated a 5MW transverse flux direct-drive generator. Borgen [50] studied the ironless generator in order to enable a higher efficiency of the generator for the floating wind turbines. Kirschneck *et al.* [51] indicated the importance to reduce the weight within the offshore direct-drive wind turbine and the difficultly using density based method for optimisation in 2015. The optimisation of the structure shape was carried out by analysing the dynamic energy in certain frequencies within the rotor frame. However, the result of using the new structure showed a limited improvement. Stander *et al.* [52] optimized the shape and size of a direct-drive PMSG to reduce the overall weight. The displacement of the three-dimensional generator model with isotropic and orthotropic materials was obtained under linear static extreme loads and magnetic stresses. Chew *et al.* [53] indicated that the analytical gradient-based method could produce a higher accuracy and efficiency when optimizing the offshore wind turbine support structures. The numerical artifacts due to the discontinuities of ultimate limit state (ULS) utilization factors can be avoided during numerical analysis. A type of direct-drive wind turbine called high–temperature superconducting generator (HTSG) was proposed for potential application in the offshore wind turbines [54-59]. It was claimed that the HTSG is lighter than the DDPMG in large size wind turbine and is more reliable than the alternative power-takeoff system in the renewable energy market. Wang *et al.* [60] developed a topology of the generator for the offshore direct-drive wind turbines, called superconducting synchronous wind generator. This generator has advantages over the normal PMWG on its weight reduction and the

reduced initial cost of installation, but the disadvantage of high maintenance costs. Arand and Ardebili [61] designed a low cogging torque axial-flux PM generator and considered different combination configurations of the poles and stator segments for small-scale direct-drive, with an attempt to increasing the working efficiency and reducing the material cost. The simulation results and experimental results showed good performances of the new designed generator and large reduction of the cogging torque in comparison with the referenced yokeless and segmented armature generator.

2.1.2. Condition monitoring and control system

According to the review of Lu *et al.* [62] in 2009 on the wind turbine condition monitoring, the elimination of the gearbox in gearless wind turbines leads to the reduction of failure rate in gearbox but increases the failure rate of all electrical related subsystems. The direct-drive wind turbines still have a higher availability than the geared ones as the mean time on repairing the electronic subassemblies is lower. The condition monitoring system (CMS), control system and fault diagnosis are important in the development of the direct-drive wind turbines. The electrical signal analysis-based CMS was reported as a potentially applicable to all types of turbines due to the less requirement on the additional hardware [8]. The normal condition monitoring systems, such as vibration, generator current analysis or temperature, cannot show their effectiveness on wind turbine due to their peculiarities. Yang [1] introduced a cost-effective condition monitoring for wind turbines in 2010 by using a continuous-wavelet-transform based (CWT) energy tracking method to extract the fault features instead of using discrete wavelet transform. Due to the unstable wind and varying operation conditions, the CM signals are usually nonlinear, nonstationary and hard to be analysed. Yang [8] developed a condition

monitoring system for the direct-drive wind turbine by using instantaneous variance, empirical mode decomposition and Teager-Huang transform (THT). The instantaneous variance criterion was used to evaluate the generator electrical signals, and potentially alert the defects on both rotor and stator windings. Then the fault detection capability would be enhanced with the aid of empirical mode decomposition. Kazemtabrizi and Hogg [63] presented a PMSG wind turbine with back-to-back fully rated converter link and energy storage system integration. The back-to-back converter link is used to extract the maximum power of the wind, and consists of two fully rated AC/DC voltage source converters linked by a DC link. The control of the converters can affect the power control of the system and enhance the reliability of the subsystems such as direct voltage support and frequency support [64]. Due to the varying wind speed, the energy storage system is normally used in the wind turbines to allow for efficient smoothing of output power without losses [65, 66]. A super-capacitor energy storage system was used to attenuate output power fluctuations and enhance fault ride through response at low power rate. Gong and Qiao [67] proposed a current-based fault detection technique to monitor the mechanical fault in the variable-speed direct-drive wind turbines, by using the synchronous sampling algorithm to convert the variable frequencies of the current signals in the generator to constant values. The fault signal was extracted by using an impulse detection method. Qiao and Lu [21, 68] conducted a survey on the condition monitoring systems and fault diagnosis for wind turbines. Chowdhury *et al.* [69] presented simple methods to monitor the parameters of the magnet flux and inductance for an interior permanent magnet synchronous generator.

2.1.3. Cooling system of the DDPMG

Since direct-drive wind turbines operate at low rotational speed, usually in the range of 10-30 rpm, the copper losses of the generator (wings) is much higher than the iron losses, which means the main function of the cooling system in the direct-drive wind turbines would be the removal of the heat from the stator windings [70]. The ability of heat removed from the stator windings has limited the size reduction of a wind turbine generator. Typically, there are two kinds of cooling systems used in wind turbines: the liquid cooling and air-cooling. Compared with an air-cooling generator in the same size, a direct liquid cooling system enables a higher output of the generator, or say, the liquid cooled generator can be smaller than the air cooled generator for the same rated power [71]. Alexandrova *et al.* [71] discussed the thermal behaviour of the direct liquid cooling direct-drive permanent magnet synchronous generators in 2014. Similar results from both analytical thermal model and the finite element analysis model showed the technical feasibility of the design of such a liquid cooling system. However, the liquid cooling system may be limited by its high cooling requirement of a large amount of water [72]. The performance of the modern neodymium-iron-boron (NdFeB) permanent magnets in the PMSGs would be better in a lower temperature under all operating conditions as the remanence flux density decreases when the magnet temperature is increased [73]. Moreover, the high temperature of the magnet can cause the irreversible demagnetization on the material. The forced air-cooling system is typically used in the direct-drive permanent magnet synchronous generators. Nerg and Ruuskanen [74] pointed out that the double-radial cooling system was mainly used in large wind turbine generator having a large air gap diameter, and studied the thermal model by using the lumped parameters, in the absence of the thermal convection coefficients and the equivalent air gaps in the generator.

2.1.4. Brake system

Usually under a normal operating condition, the rotating speed of the generator can be controlled by using the aerodynamic control system (the blade pitch control system). The combination of the mechanical disk brake system is designed to stop the wind turbine in an emergency condition, such as extreme weather conditions and hurricane. For indirect (geared) wind turbines, the mechanical disk brake is normally located on the high speed shaft for high efficiency. On the contrary, for direct-drive wind turbine, the brake system is mostly located directly on the rotating part (shaft or rotor).

2.1.5. Bearing system

Different types of bearings have been used in several locations through the nacelle, blade pitch, yaw system, main shaft support, generator and inside the gearbox. The types and sizes of the bearings depend on their locations and loading conditions. For example, two main bearings for the drive-train system used in the NREL 5MW direct-drive offshore wind turbine are different. In particular, a double row tapered roller bearing with inner race close to the centre of gravity of the drive-train system is designed to carry both the axial and radial loads, while the other is a cylindrical roller bearing designed to take radial loads only. Other types of bearings, such as the slewing ring bearings are typically used in the yaw system.

2.1.5.1. Mounting system with misalignment

It is known that the wind directions can be variable with time. The misalignment between the wind direction and the rotating axis would result in heavy loading and large strain on the structure, which may cause the energy loss and shorten the working life of wind turbines. The mounting system includes the blade pitch system and the yaw system, which

are designed to change the facing direction of the nacelle in order to reduce the undesired or harmful loads and moments.

2.2. Tower

The tower structure should be able to provide easy access for the maintenance of the rotor components and its sub-components, easy transportation and erection. The structural design of the tower should ensure efficient, safe and economic operation for the whole wind turbine system. A good design would also incorporate aesthetic features of the overall machine shape. In fact, there are no simple criteria to identify the above-mentioned objectives [75]. However, the success of tower structural design should be largely judged by the extent to which the wind turbine main function is achieved.

2.3. Substructures

Different structures of the tower support technology have been developed for offshore wind turbines [76], and naturally progressed from land-based to shallow-water and transitional-water, and then to the deep-water with floating platform, as shown in Figure 2-6. The foundations for the offshore wind turbines are operationally challengeable in offshore harsh environment and typically cost 25%-35% more in an overall offshore wind farm project [77]. Carroll *et al.* [78] summarized the failure conditions of about 360 offshore wind turbines throughout Europe in 2016 for better operation and maintenance of planners and managers.

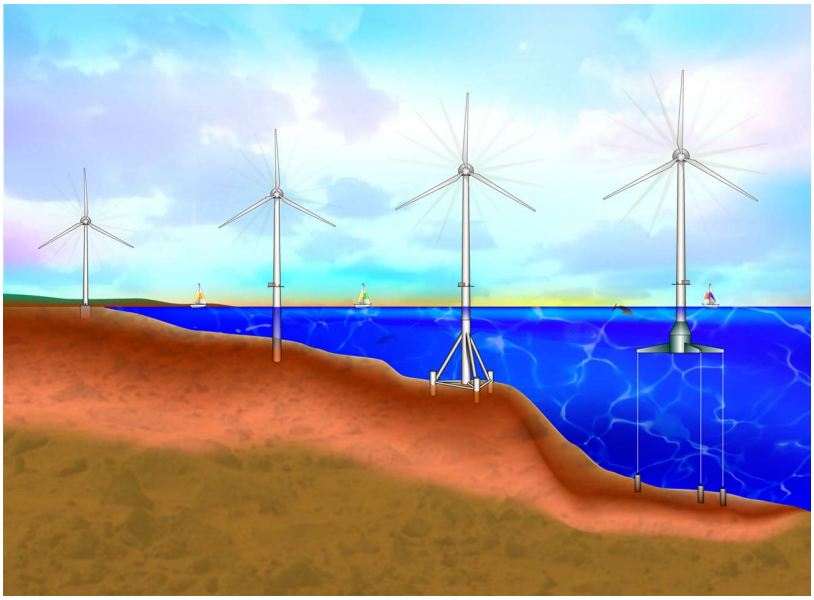

Figure 2-6 Natural progression of support structure from land-based to floating-based[76]

Perez-Collazo *et al.* [79] presented the technologies and substructures to integrate the offshore wind and wave energy. Different from the land-based wind turbine, the support substructure for offshore wind turbines can be classified according to the water depth, from shallow water (0-30m), transitional water (20-80m), to deep water (over 80m). Fixed-based and floating-based substructures can be chosen depending on the site conditions. Most substructures used in shallow water or transitional water are fixed-based supporting system, as shown in Figure 2-7. The most representative technologies used in shallow water are the monopiles and gravity based structures. More complex technologies, such as the jacket frames and multi-piles, have been used in the transition water due to the increase of the water depth. By the end of 2014, 99.9% of the substructures installed for offshore wind turbine in Europe were fixed-bottom, which included the monopiles (78.8%), jackets (4.7%), tripods (4.1%) and tri-piles (1.9%). The floating substructures only comprised 0.1% of all installed foundations [80]. However, the floating type offshore wind turbines have a great potential to be a reliable source of electricity generation.

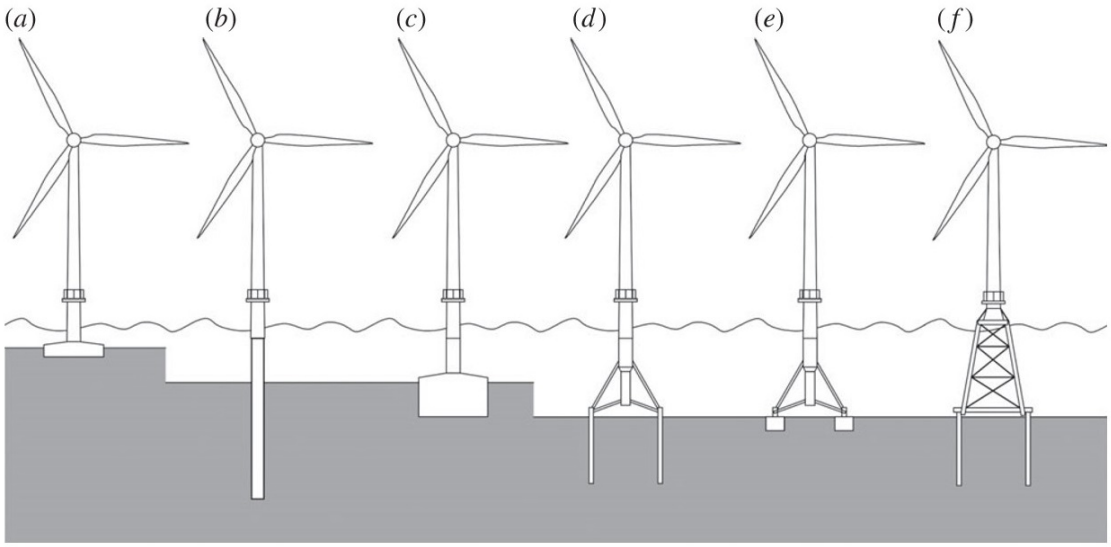

Figure 2-7 Fixed-based offshore wind turbine;(a) gravity based,(b)monopile, (c)caisson foundation,(d)multi-piles, (e)multi caisson, and (f) jacket[81]

2.3.1. Types of floating substructures

The floating substructures are considered under deeper-water conditions. Different prototypes of floating foundations are still under testing and prototyping as they are still in the early stage of development. Musial *et al.* [82] discussed the advantages and disadvantages of the platform topologies. The floating platform topologies can be classified in terms of single- or multiple-turbine floaters, or the mooring method. A floating system consisting of multi turbines could possibly reduce the total weight for the large system (>20MW per system structure) but normally has higher construction cost than single-turbine floaters. Thus, the single-turbine concept has been considered in most published papers. The mooring method can dictate much of the platform architecture. There are three commonly used mooring systems; catenary moorings, taut-leg moorings and vertical tension legs, in which the vertical tension legs can be considered to be a subset of taut-leg moorings, as shown in Figure 2-8. Pecher et al. [83] conducted a

comparison study of a single anchor leg mooring and a three-legged catenary anchor leg system under the same reference load case, by using the quasi-static analysis to find the system size and stiffness required. Guo *et al.* [84] developed a quasi-static analysis on the multi-component mooring line, and investigated the performances of both segments contained within water column and soil column during pretension and under service conditions.

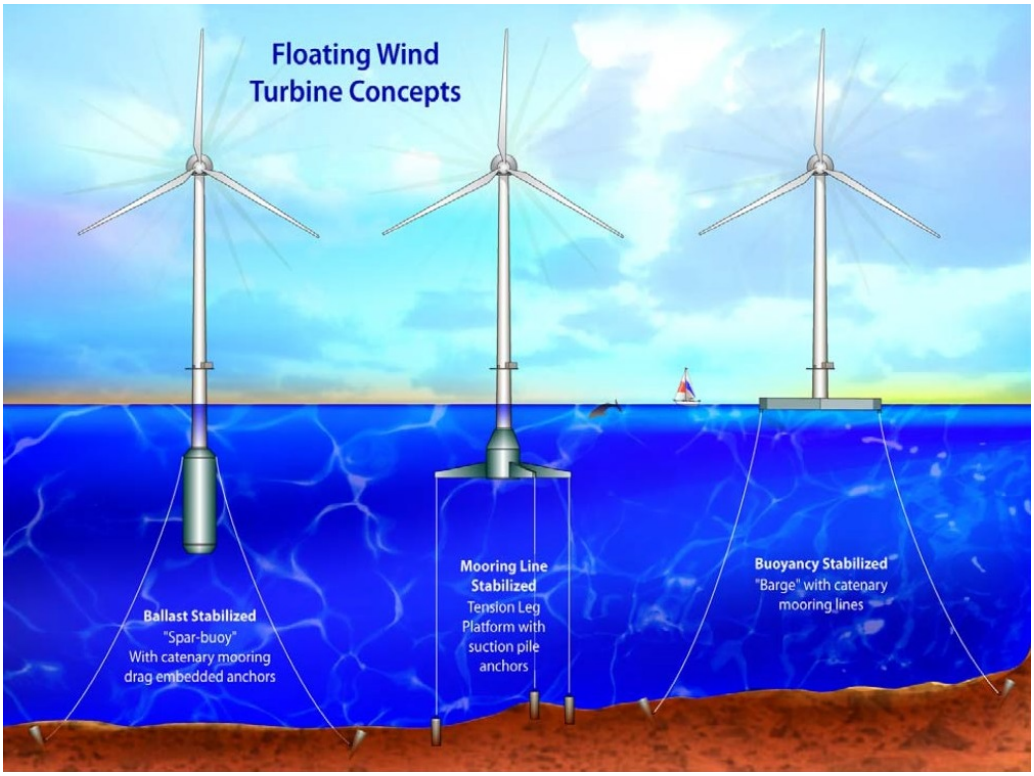

Figure 2-8 Floating-based wind turbines[76]

Platform architectures with the mooring methods are commonly known as spar floater with catenary moorings, tensioned-leg platform with taut-leg moorings, and semi-submersible platform (moveable platform, which requires further development). Henderson *et al.* [85] gave the initial evaluation for the floating platform, such as the yaw mechanism and the number of turbines per floater. They briefly discussed various floating concepts and studied the tri-floater with its preliminary designed mooring. Butterfield *et*

al. [86] provided a framework for different platform architectures on the basis of their static stability criteria. The NREL 5 MW wind turbine has been widely chosen when studying the vibration behaviour for the offshore direct-drive wind turbines [9, 19, 87, 88]. It is a catenary moored spar-type direct-drive wind turbine. There are three sets of mooring lines attached on the circumference of the spar with two segments for each. The segments are used to provide yaw stiffness. Each adjacent line is 120 degree apart, with different stiffnesses in surge and sway motion directions [19]. The force-displacement relation of such a mooring system acting on the spar-support can be simulated by using the software, DEEPC.

2.3.2. Trends and challenges for offshore wind turbines

Snyder and Kaiser [89] discussed the feasibility of using offshore wind energy to replace the fossil-fuelled electricity or the onshore wind energy through the ecological and economic cost-benefit analysis. The offshore wind energy has the same potential ecological impacts as the onshore wind energy. In some cases, offshore wind power can be cheaper and have less environmental impacts. Laura and Vicente [90] used the life-cycle cost system to evaluate the cost breakdown structure of three different floating platforms for offshore wind farms. The key cost variables in each of the six phases, namely definition, design, manufacturing, installation, exploitation and dismantling, were obtained for the optimization of wind turbines. Kaldellis *et al.* [91] stated the situation of the offshore wind turbine techniques until 2015 and discussed their effects on the environmental and social impacts. There were obvious differences between the onshore and offshore environment. Since the offshore environment is variable depending on the

site condition, knowledge on the local environment and social conditions is required in the future development of offshore wind turbines.

3. Internal and environmental excitations on the offshore direct-drive wind turbines

Offshore environmental loads, which not only come from the wind but also from sea wave and current, can induce the vibrations of wind turbine structures. To reduce the overall costs and design the next generation wind turbines and their substructures, the general dynamic model for each wind turbine and the specific site condition for installation and operation in the marine environment should both be taken into account. The understanding of the excitations applied on and within the whole turbine system can thus be helpful for studying the dynamic behaviours.

3.1. The UMP force in the generator

One main source of internal excitations in the generator is the magnetic force distribution within the air-gap between the rotor and stator [92]. Such a force distribution, which has been referred to as the unbalanced magnetic pull (UMP) force, is mainly caused by the eccentricity of both rotor and stator in the generator, and can also be caused by the bearing defect, manufacturing defect, unbalanced mass and the non-uniform magnetic field distribution in the air-gap [92-96]. The UMP force can potentially lead to the damage to the rotor system through the induced vibrations if the rotor system experiences severe vibrations.

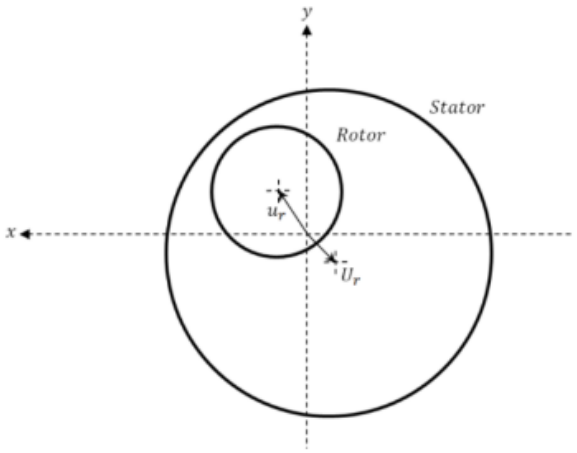

Figure 3-1 Stator eccentricity and rotor eccentricity in the generator

Figure 3-1 illustrates explicitly the air-gap eccentricity, where u_r is the displacement of the rotor centre from its rotating axis and U_r is the displacement of the stator centre from the rotating axis. If R_s represents the inner radius of the stator, R_r denotes the outer radius of the rotor, then the average air-gap between the rotor and stator Δr can be calculated by using the inner radius of the stator and the outer radius of the rotor. The UMP force is nonlinearly proportional to the air-gap and the direction of the UMP force is the same as the smallest air-gap vector. Structural integrity of wind turbines and design criteria as specified in current standards require the eccentricity less than 10% of the average air-gap for a safe operation of the direct-drive generator [97-99].

The calculation of the UMP was based on the empirical formulas and theoretical study in early papers [100-102], on the fundamental magnetomotive force wave using a Fourier series air-gap permeance [103-105], and on finite element analysis [106, 107]. Only few researchers have studied the vibratory characteristics of the rotor system due to the UMP in the early stage [96]. One simplified expression for UMP, which was given by Gustavsson and Aidanpää [94], is very convenient in analytically performing dynamic analysis of the drive-train system and can be expressed as

$$f_m = \frac{\mu}{2}\frac{S_s^2}{p^2}\frac{R_s^2 h\pi}{\Delta r^2}\frac{\Delta e}{\sqrt{(1-\Delta e^2)^3}} \qquad (3.1)$$

where μ is the permeability of the magnet in the air-gap, S_s is the linear current density in the stator, p is the number of pole pairs, R_s is the inner radius of the stator, h is the length of the air-gap, and Δe is the relative eccentricity which is defined as $\Delta e = \frac{u_r + U_r}{\Delta r}$.

3.2. Aerodynamic excitation

The main aerodynamic excitation acting on wind turbines is in the form of wind excitations, which have two components, the deterministic and stochastic components. The deterministic component is normally described by a common wind shear model which can be expressed as, $V_{(z)} = V_H(\frac{z}{H})^{\alpha}$, where $V_{(z)}$ is the mean wind speed at the altitude z, V_H is the reference wind velocity at the reference altitude H, α is the wind shear exponent. The drag force of fluids passing through structure can be calculated by using $F_w = \frac{1}{2}\rho_a {V_{r(z)}}^2 C_d A_{(z)}$, where ρ_a is the air density, $V_{r(z)}$ is the relative velocity of the wind and the structure, C_d is the drag coefficient of the structure and $A_{(z)}$ is the equivalent characteristic surface area. It is normally assumed that the tower motion is small when studying the tower vibration of the wind turbine, thus the relative velocity at elevation z is close to its wind velocity $V_{r(z)} \approx V_{(z)}$. The wind loads on the tower and at different locations of the blades can be different from those expressions due to the variable wind speeds at different altitudes. The wind speed profile considering the wind shear instead of using the mean wind speed at the hub height of the wind turbine would provide more accurate evaluation of the power output. Wagner *et al.* [108] calculated the wind power flux using wind speed profiles with lidar measurements and pointed out that the use of

the wind shear model can actually improve the accuracy of the energy production estimation.

The stochastic component also known as the turbulence wind can be significant compared to the deterministic component, however its mean value was considered to be zero [109]. Colwell and Basu [110] used a discrete Fourier series with zero mean to represent the arbitrary fluctuating component of the wind drag force on the offshore wind turbine. Karimirad and Moan [19] discussed the effect of the turbulence wind on its power performance and response. The turbulence effect was highlighted by comparing the constant and turbulent wind cases in the same offshore environment. It was found that the turbulence did not significantly affect the mean power output, but the power fluctuations would be notably increased under the below-rated wind speed condition.

Wind excitations acting on the wind turbines can be discussed in two parts, the blades and the tower, which could also lead to the interactions between the different components within the wind turbine.

For the wind excitation on the blades, not only a thrust force is generated but also a high torque in the generator would be produced. The thrust force can be transformed directly to the tower through the drive-train system in the direct-drive wind turbine, while radial forces can be produced due to the high torque rotating. The radial forces of the drive-train system are normally generated at the bearings (bearing forces) and rotor-stator position (UMP). In order to control the torque operation, blade-pitch control system is used to limit the above-rated rotating speed. For the above-rated wind speed, the rotating speed will be limited at the rated speed by using a blade-pitch control system. When the wind speed is over the cut-out speed, the drive-train system would be stopped in order to survive by using both blade-pith control system and the brake system. Sethuraman *et al.*

[9, 88] and Karimirad *et al.* [19] simplified the blade model and implemented the parameters of the blade into the software HAWC2.

For the wind excitation on the tower part, most papers use a mean wind shear model to calculate the long-term wind force and take the tower shadow into account. The tower shadow effect is the torque variations caused by the wind speed changes when the blades pass through the tower region. For the upwind wind turbines, the torque would change as the wind is redirected when the blades are in the tower region. For the downwind wind turbines, the wind speed would decrease due to the tower obstruction. Murtagh [30] stated that the blade and tower interaction can be ignored in some cases, however in other cases, the tower shadow effects need to be considered.

3.3. Hydrodynamic excitation

3.3.1. Wave

Waves in deep-water environment can be assumed as a nearly linear superposition of harmonic components according to the linear theory of waves. The linear wave theory describes the linear gravity waves on the surface of a homogeneous fluid layer, and assumes the fluid layer has a uniform mean depth. The surface elevation measured relative to the mean fluid level is a representative parameter. Orbital fluid motions under the surface around their average position are associated with the free motion of the wave when the surface elevation is propagated. According to the linear dispersion relationship, the wave property, such as the velocity potential, dispersion relation, wave length, dynamic pressure, group velocity, particle velocity in the horizontal and vertical directions, can be different under shallow-water, transitional-water (intermediate-water), and deep-water conditions.

Based on the linear wave theory, the waves with longer periods have a higher celerity than the waves with shorter periods. A complex three-dimensional short-crested surface elevation can be generated within or close to the area where the waves are generated. Most of the standard models of the sea waves are wind generated and can usually be characterized by the power spectral density function (PSDF). The sea surface elevation is a representative parameter of the sea state. The distribution of the sea waves is Gaussian random, which is regarded as an infinite number of independent waves with different wave height and wave periods.

A fetch condition, which the wind blows over an uninterrupted distance without a significant direction change, was considered to approximate the sea surface elevation spectrum [111]. The Pierson-Moskowitz (PM) spectrum was first developed to define the relationship of the energy with wave frequency, by assuming that the wave is in equilibrium with the wind when it blows steadily over a large area for a long time, which has been referred as fully developed sea [112]. The Pierson-Moskowitz spectrum can be expressed as

$$S(f) = \alpha g^2 (2\pi)^{-4} f^{-5} \exp\left[-\frac{5}{4}\left(\frac{f_m}{f}\right)^4\right] \qquad (3.2)$$

where α is Phillips constant, g is the gravity constant, f and f_m define the wave natural frequency and peak frequency.

However, the sea wave was never to be fully developed from the data which were collected and analysed in the Joint North Sea Wave Project (JONSWAP) [110]. The JONSWAP spectrum (under a fetch condition) was then used by introducing additional factors to improve the performance. The peak increase in the spectrum and the frequency

shift of the maximum spectrum were considered [113]. The JONSWAP spectrum can be written as

$$S_j(f) = S(f)\gamma^r \qquad (3.3)$$

where $r = \exp\left[-\frac{(f-f_m)^2}{2\sigma^2 f_m^2}\right]$, γ and σ are free parameters.

The long-term variability of wave loads can be defined by using two wave spectral parameters, the significant wave height (H_s), and the peak period (T_p). Johannessen *et al.* [114] used a Weibull distribution to describe the significant wave height and a lognormal distribution to introduce its peak period, which was correlated with the given mean wind speed at 10 m height and the significant wave height. The expected values of the significant wave height and the peak period are

$$E(H_s) = \beta\Gamma\left(\frac{1}{\alpha}+1\right), \qquad (3.4)$$

$$E(T_p) = (4.883 + 2.68H_s^{0.529}) \times \left\{1 - 0.19\left[\frac{v-(1.764+3.426H_s^{0.78})}{1.764+3.426H_s^{0.78}}\right]\right\} \qquad (3.5)$$

where α, β, v are free parameters.

A JONSWAP spectrum using the significant wave height and the peak period to describe the wave can take the form of

$$S_{\eta\eta}(\omega) = \frac{5}{16}H_s^2\omega_p^4\omega^{-5}\exp\left[-\frac{5}{4}\left(\frac{\omega_p}{\omega}\right)^4\right]\gamma^{\exp\left[-\frac{(\omega-\omega_p)^2}{2\sigma^2\omega_p^2}\right]} \qquad (3.6)$$

There are other wave spectra which can be used in marine construction. Nie *et al.* [115] introduced the Doppler spectrum based on the JONSWAP-type nonlinear waves to study the microwave backscattering in a mixed ocean environment. Molander and Garcia-

Gabin [116] compared the Ochi-Hubble spectrum, a double-peaked wave with the Torsethaugen spectrum [117].

3.3.2. Sea current

The sea current is an important source of hydrodynamic damping of the floating platform [76]. It is usually assumed as a primary horizontal water movement and can be represented by using the viscous-drag term in the Morison's equation. The sea current direction and strength are only related to the site condition but can be different due to the change of water temperature over time.

3.4. Earthquake

For the wind turbine locates in or near the actively seismic regions, the earthquake should also be taken into account for the safety issues. The interaction between earthquake, soil and support structure could have direct effects on the vibration performance of a fixed-based wind turbines. Moreover, indirect effects may also exist on the floating type wind turbines as there is an interaction among the earthquake, waves and currents. Currently, the simulation results using a simple superposition of those excitations are unable to obtain reasonable combined structural responses with the experimental results, since there is still an unclear interaction among the wind, wave, current and seismic excitations.

4. Vibration performance and structure optimization

4.1. Tower vibration

The wind turbine tower was considered as uniform tubular segments with the variables of cross-sectional area and gyration radius in earlier studies. Negm and Maalawi [75] studied five optimization strategies for the land-based tower to reduce the vibration level of the tower by using uniform segments. The cross-section area, radius of gyration and the heights of the uniform segments were considered as design variables in optimization analysis. Lavassas *et al.* [23] used two different finite element models to perform the analysis of a steel 1-MW wind turbine tower having a tubular shape under extreme wind and earthquake loads, and pointed out that the dynamic characteristics are critical for the overall design of the tower structure. In order to minimise the cost of the tower structure for a land-based wind turbine, Uys *et al.* [118] investigated a 45 m steel shell wind turbine tower formed as cylindrical shapes. Wind excitations obtained from the Eurocode and the buckling constraints from the ring-stiffeners were included in the optimization algorithm to find a cost-effective tower structure. Murtagh *et al.* [30] incorporated a three rotating blade model into a multi-degree-of-freedom model of a flexible annular tower. The resultant shear forces from the blades were applied at the top of the tower. The displacement response at the top of the tower was found to decrease as the blade rotation frequency increases. Adhikari and Bhattacharya [119] considered the subsea foundation structures for the shallow water offshore wind turbines and used the Euler-Bernoulli beam-column theory to develop an elastic end support model to study the dynamic behaviour of the foundation structure. The natural frequency of the tower was found to decrease with a decrease of foundation stiffness and an increase of axial load.

Unlike the tower structure of fixed (land)-based wind turbines, for the floating type wind turbines, the boundary condition of the turbine structure is under a free-free end condition, instead of a free-fixed end condition. Recently flexible towers were considered by using the NREL-developed FAST servo-elastic software coupled with other modules in studying the dynamic behaviour of the floating type offshore wind turbine under excitations [120-124], where they did not focus on the natural frequency analysis of the floating wind turbine tower.

4.2. Substructure performance

4.2.1. Fixed-base substructure

Kallehave *et al.* [81] discussed the potential for the optimization of the monopile support of offshore wind turbines and developed basic understanding of monopole structures from mechanical engineer perspective. Byrne *et al.* [125] proposed a design method for the monopile support of offshore wind turbines by incorporated the advanced geotechnical effects such as cyclic behaviour and densification into the developed 1D (parameterised) monopile model. Prendergast *et al.* [126] found that the scour can have noticeable effect on the natural frequency response of the monopile-supported offshore wind turbine. A scale-model of the monopole support was examined at a dense sand test site to investigate the effect of scour at different offshore environment (different soil densities). However, some other interactions which may affect the frequency response of the model, such as the gyroscopic effects of the blade or the fluid-structure interaction effects, were not considered. The examination of the damping from different sources, such as structural and soil damping to the support, can be helpful for the vibration reduction of offshore wind turbines. Soil damping was found to have the largest discrepancy among all sources

[127]. Carswell *et al.* [128] used a linear elastic two-dimensional finite element model to develop a foundation-damping model for the lumped parameter model by converting the hysteretic energy loss into a viscous, rotational mudline dashpot. Morato *et al.* [129] used the aero-hydro-servo-elastic simulator, FAST to analyse the response of the monopile-supported NREL 5MW prototype wind turbine for the ultimate limit state load cases. The design load cases, extracted from the well-known database based on the IEC 61400-3, were used for checking the structural integrity of the offshore wind turbines. The overturning moment of the support structure and the flapwise and edgewise moment at the blade root, as the key parameters for designing the structure and blade, were obtained from the simulations. Wang *et al.* [130] investigated the performance of multi-pile offshore wind turbine under an earthquake condition coupled with wind, wave and current loads. The interaction of earthquake, hydrodynamic and aerodynamic excitations was considered necessary to obtain the reasonable results. Adhikari *et al.* [119] characterized the subsea foundation structures for the shallow water offshore wind turbines which consist of a single- or multi- monopile. Both wind and wave excitations can lead to large movement of the exposed structure and the upper part of the monopile. An elastic end-support model using the Euler-Bernoulli beam-column theory was developed for the free vibration analysis of the dynamic behaviour of those foundation structures. The natural frequency of the tower was found to decrease with the decrease of the foundation stiffness and the increase of the axial load.

4.2.2. Floating based substructure

Larsen and Hanson [131] pointed out that the lowest structural frequencies of the floating wind turbine tower were lower than those of a normal bottom mounted tower. Colwell

and Basu [110] developed a MDoF tower model to study the response of an offshore wind turbine tower under both moderate and strong wind conditions. The Kaimal spectrum and the JONSWAP spectrum were used to describe the wind and wave excitations. A tuned liquid column damper was introduced as an additional damping system to reduce the peak response of the tower system. It was found that under the same wind and wave conditions, the peak response of the offshore wind turbine tower with a TLCD system could be reduced up to 55% compared to the tower without such a system. The additional damping system in the offshore wind turbine could also increase the fatigue life of the tower and provide optimization opportunity to make the system more efficiently. Karimirad and Moan [19] studied the dynamic response of a spar-type 5MW wind turbine under harsh and operation environmental conditions. The nonlinear aerodynamic forces, hydrodynamic forces, turbulent wind, and relative wind velocity were considered as the primary sources of excitation. By carrying out a comparative study of the wave- and wind-induced response, it was found that the wind can induce the mean values of the dynamic response and the wave generate the standard deviations of the response. Furthermore, it was pointed out that the turbulence wind model was not necessary to be used in fatigue analysis since it did not significantly affect the structural response. Ramachandran *et al.* [18] studied the coupled three-dimensional dynamic response of a tension-leg platform floating offshore wind turbine under wave and wind excitation. The entire wind turbine was formulated using 17 DoFs, of which six for the platform motion and the rest for the wind turbine itself. Morison's equation and the unsteady blade-element-momentum (BEM) theory were used to calculate the three dimensional wind and wave loading. Noticeable influences were found from the platform to the tower due to the wind shear and the turbulence effects. Compared to the simple model, a good agreement was obtained by using an advanced aero-elastic code, Flex5. Zhang *et al*. [132] developed a 13 DOFs

tower-blade-drivetrain offshore wind turbine model. The generator torque was calculated from a 3 DOFs turbulence and then transferred to the nacelle and the tower through the different drive-train systems. An active generator controller was used to reduce the lateral tower vibration due to the aerodynamic (wind) and hydrodynamic (wave) loads applied on the tower. Arany *et al.* [133] presented a simple methodology to calculate the natural frequency of the wind turbine sitting on a monopile. The monopile foundation was modelled by the lateral, rotational and cross coupled springs. The natural frequencies were numerically found from the transcendental equation. It was shown that the flexibility factor of the foundation was sensitive to its rotational stiffness and the effect of its lateral stiffness was limited to the natural frequency.

There are other subsystems in the wind turbine helping to control the vibration behaviours of the structure. Shresyha *et al.* [48] employed a FE model to verify their new design by using the magnetic bearings in 2010. Both magnetic forces and gravitational forces were considered. Muliawan *et al.* [17] combined a wave energy converter (WECs) and a spar-type floating wind turbine (FWT) to increase the density of the power output. The dynamic response of the wind turbine was studied in the time domain by using SIMO/TDHMILL3D, the mooring tension in the new concept was also compared with that of the spar-type FWT. The WECs in the spar FWT was found to increase the total energy output by 10-15%. Basu *et al.* [20] introduced a circular liquid column damper to suppress the edgewise vibrations in wind turbine blades. Dezvareh *et al.* [16] applied a tuned liquid column gas damper onto a jacket-type offshore wind turbine, and found that the vibration absorber could reduce the nacelle motion's standard deviation and acceleration by over 45% from simulation. Sopanen *et al.* [134] combined an electro-mechanical design of the control system and condition monitoring of variable-speed wind turbines to analyse the vibration of the whole direct-drive wind turbine. They claimed that

the method could help to evaluate the maximum value of the cogging torque and the tolerated torque ripple. The PMSG with main shaft was used in the mechanical model based on the details of existing PMSG, which was studied by Pyrhönen *et al.* [135]. It was found that the large part of the inertia of the blades does not play a major role in the high frequency vibration and can be neglected in the analysis. A more detailed model with flexible blades was also developed later [136]. Ruzzo *et al.* [137] carried out a modal analysis for the offshore floating platform by using the frequency domain decomposition method. A simple spar-type structure with lumped-mass nacelle was implemented in ANSYS AQWA for the numerical analysis of natural frequency, model shape and damping ratio. Bae and Kim [138] performed the fully-coupled dynamic analysis of a mono-column-TLP-type floating offshore wind turbine. The uncoupled analysis of the offshore platform was typically used for oil or gas, the whole body were treated as a rigid body and the relative motions among the wind, wave and platform were normally not considered. However, the fully-coupled simulation results showed that the consideration of relative velocity, blades running condition and the flexibility of the body could increase the wave and wind loadings on the structure and affect the pitch resonance and the frequency response.

4.3. Dynamic performance due to excitations

4.3.1. Rotor dynamics within the drive-train system

Struggl *et al.* [139] reviewed the different models used in the study of the drive-train system in wind turbine (mostly for geared wind turbines), in terms of general considerations, modelling methods and useful tools. The dynamic analysis of direct-drive wind turbines has been performed by many researchers [19, 76, 140-142], but less

information has been found on the dynamics of drive-train system [9]. Sethuraman *et al.* [9] developed a fully coupled mechanical model to study a 5MW direct-drive generator for floating spar-type wind turbine. A topology of the generator considered was based on a low-speed radial flux permanent magnet generator with the interior rotor, which was studied by Zavvos *et al.* [143]. The main properties such as the generator, aerodynamics, blade structural and mooring properties used in their study were adopted from other papers [19, 94, 144]. A further study on the drive-train dynamics was conducted recently in 2017 [88]. The response variables, such as shaft displacement and loadings, of land-based and floating-based wind turbines were compared. Teng *et al.* [145] did a comparative analysis of a faulty and normal DDWTG to monitor and diagnose the fault of the rotor bearings. The multiscale enveloping spectrogram, which can manifest the fault modulation information, was introduced to detect the weak bearing faults. Pezzani *et al.* [146] used a resampling vibration signal technique to analyse the bearing faults in PMSG. Unlike the other traditional methods, the rotor position estimation was replaced by using a dual second order generalized integrator phase-locked loop to measure the load and voltage disturbances in the generator. Bearings under both constant and variable speeds were studied to show the performance of the phase-locked loop.

4.3.2. The UMP effect in the generator

The vibratory characteristics of the rotor system due to the UMP force was studied for a three-phase generator at a high rotating speed in 2002 [96]. There are two parts of the UMP force in a three-phase generator with multi-poles, a constant non-linear component and an oscillatory component. The vibration response was compared with low value of the pole pair in the generator. Sandarangani [147] in 2006 showed that the alternating

magnetic force would decrease when the number of pole pair increases. Gustavsson *et al.* [94] stated that for a generator with high number pole pairs the alternating force can be ignored as it is insignificant when comparing to its constant component. Rodriguez *et al.* [92] in 2007 examined the excited vibration frequencies in the generator due to the eccentricity of its rotor, by considering the slotting, saturation and the possible stress distribution. A non-linear relationship between the dynamic eccentricity and the vibration of the rotor system was found by monitoring its low frequency and low order force distributions. Zarko *et al.* [148] in 2012 and Petrinic *et al.* [149] in 2014 studied the effect of both stator and rotor winding and the effect of the load condition on the unbalanced magnetic pull force by using the finite-element method.

4.3.3. Environmental excitation effects

Wang and Coton [150] developed a high resolution tower shadow model for the aerodynamic performance of downwind wind turbines, by using a prescribed wake model and a hybrid method combining the unsteady aerofoil scheme to perform an unsteady prescribed wake model. This method showed some improvement over a blade element-momentum (BEM) method in which it can provide the effect of the shed wake on the blade loading near the tower shadow region. Munduate *et al.* [151] stated the importance of using an unsteady tower shadow model. A wind tunnel test was conducted to measure the pressure on the blade surface for a scaled two-blade wind turbine. It was shown that the unsteady model could predict the characteristics of the aerodynamic response. Dolan and Lehn [152] investigated the effect of the wind shear and tower shadow on a three-blade wind turbine. A 3P pulsation due to the wind shear was found to produce a small DC reduction in the torque oscillation. It was shown that the tower shadow effect is more

dominant than the wind shear effect. The radius of the tower and the independent height were two key parameters in studying the effect of the tower shadow. Chattot [153] presented a helicoidal vortex model to describe the effect of the tower shadow on the blade root flap bending moment. However, there were some discrepancies when comparing the numerical results to the experimental data. Fadaeinedjad *et al.* [154] used a software package to model the aerodynamic aspects on a wind turbine. The effect of tower shadow, wind shears, the yaw error and the turbulence on the power produced were compared on power quality. Bayindir [155] applied a compressive (high-order) spectral method to simulate the nonlinear gravity wave by using a compressive sampling algorithm. The proposed method required fewer spectral components and less computation time than the classical method. By comparing the results using both classical method and compressive model, high accuracy of simulation results for the linear and the fully nonlinear ocean waves were found but with much less computation time required. Slunyaev and Kokorina [156] stated that the probability of high waves in the moderate rough sea conditions could be increased due to the large amplitude soliton-like groups. Raed *et al.* [157] studied the effect of wave force at different sea locations on a semi-submersible wind turbine support structure. The JONSWAP spectrum was used to calculate the wave spectra and the Morison's equation to estimate the wave load on the structure. The numerical results showed that the wave forces could be significantly variable with respect to the wave crests at different columns of the structure body. Dematteis *et al.* [158] used the modified nonlinear Schrödinger equation to investigate the rogue waves under deep-sea condition. Random initial data with available observed data of the rogue waves were implemented in the large deviation theory. The simulation results showed that the rogue waves were mainly caused by the modulational instabilities and have specific precursors which could be used for early detection. Kim *et al.* [159]

studied the effects of the coupled wind, wave and current loads on bottom-supported offshore wind turbines. The characteristics of wind, wave and current under a hurricane condition were investigated firstly, and then the response of both monopile-supported and jacket-supported offshore wind turbines during Hurricanes Ike (2008) and Sandy (2012) were studied. For Hurricane Ike case, the analysis was focused on the wave condition, the effects of the yaw misalignment, blade control and turbine parking strategies. For Hurricane Sandy case, the analysis was on the response of the jacket support and the effects of the coupled hydrodynamic and aerodynamic loads.

5. Rotor dynamics within the direct-drive drive-train system

Direct-drive wind turbines, different from the standard geared wind turbines, usually use a direct-drive permanent-magnet generator to avoid the gearbox failures. In the absence of a gearbox in the drive-train system, the direct-drive generator operates at low rotating speeds. Thus, direct-drive wind turbines require a larger sized generator (higher weight) to transfer the kinetic energy into electrical energy. The inherent unbalanced magnetic pull (UMP) force of the generator can have impact on the vibration behaviour of the drive-train system. The direct-drive drive-train system is normally considered to consist of a uniform hollow shaft which is supported by two roller bearings, a rotor, and the hub with blades. The main shaft and two main bearings are included in the model. Inclusion of the main bearings into the drive-train system is necessary to determine the bearing load fluctuations, as discussed in simulating wind turbine gearboxes [160].

5.1. Modelling of the direct-drive drive-train system

The main components and system parameters of the direct-drive wind turbine studied in this chapter, such as the generator rotor, main shaft, and hub with blades, are adapted from the designed 5 MW wind turbine with DDPMG [9, 19, 144, 161]. Figure 5-1 shows the main structure of the rotor nacelle of a 5MW direct-drive wind turbine [9].

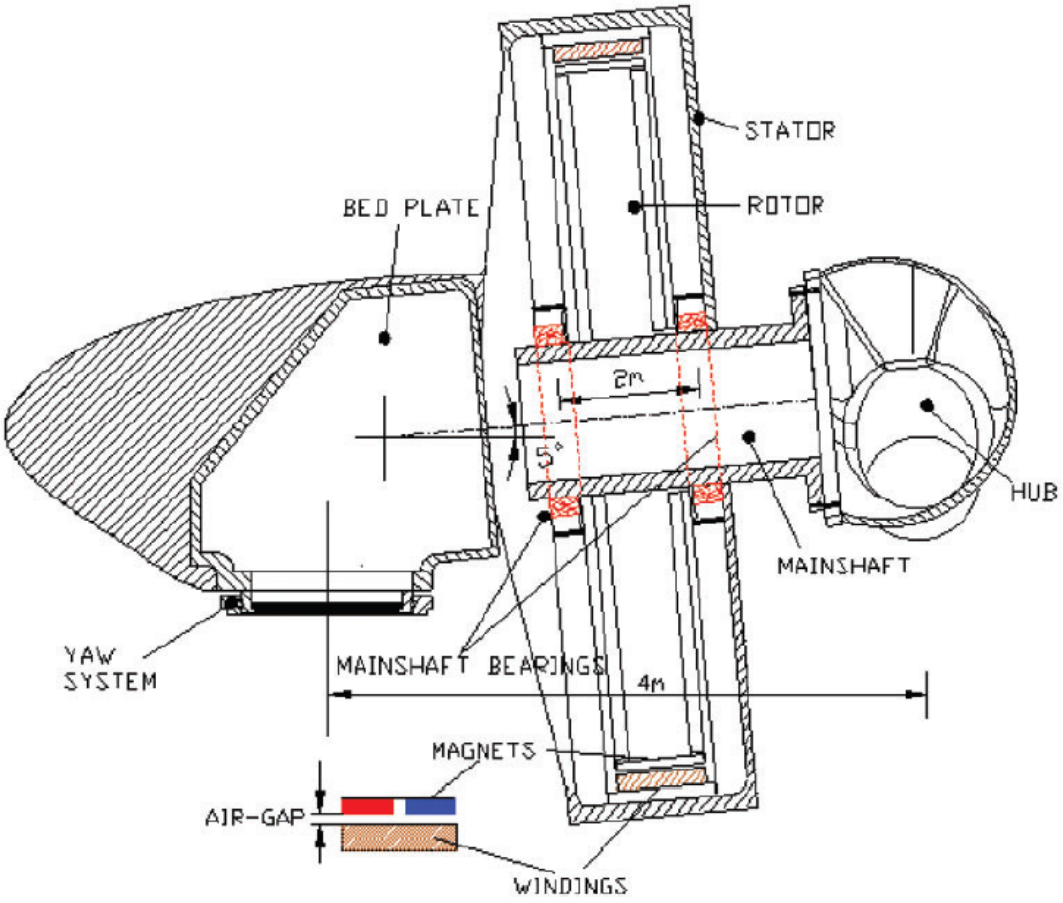

Figure 5-1 Rotor nacelle [9]

The stator is assumed to be fixed and constrained in all directions. The rotor system is held by two different bearings which are fixed with the stator. The bearing types and configurations are chosen based on the requirement of the stiffness-to-mass ratio and the recommendation from the bearing manufacturer TIMKEN [162]. Bearing 1 is referred to here as the one away from the hub, and is designed to take the radial loads only. Bearing 2 (located close to the hub) is designed to carry both the axial and radial loads. Both bearings are assumed to be isotropic with their own stiffness (k), damping coefficients (c) and independent loads. The simplified schematic of the drive-train system is shown in Figure 5-2. Since the rotor, main shaft, and hub with blades are fixed together, the drive-train system would have a total mass m, moment of inertia I and polar moment of inertia I_p.

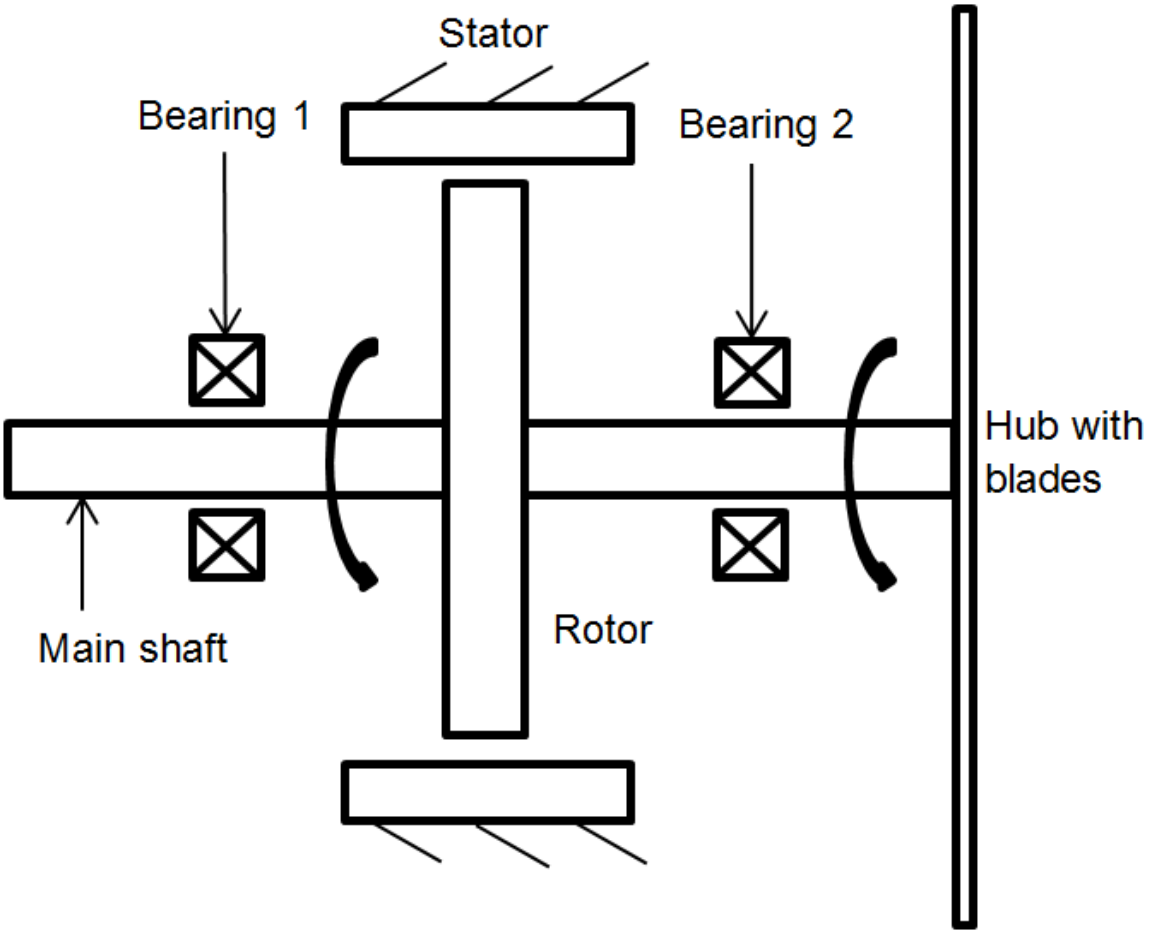

Figure 5-2 Structure sketch of the rotor system with a fixed stator

Given the fact that the direct-drive wind turbine operates at low rotating speed and that the generator has a larger size than the generator in the geared wind turbines, the whole rotor system is thus assumed to be rigid and its dynamic model will be a nonlinear system of 4 degree-of-freedom (DOF) by considering the translational and rotational motion [9, 88]. The force analysis of the rotor system is shown in Figure 5-3 . Let x be the positive displacement in x-direction, θ_y be the rotational angle about y axis and l_i be the distance from the centre of gravity (CG) of the drive-train system to a specific position along the shaft. The displacement with small angle inclination at a specific position in the x -direction is given by $(x + \theta_y \times l_i)$. With the same assumption, if y is the positive

displacement in y-direction and θ_x is the rotation about the x axis, the displacement with small angle inclination at a specific position in y-direction is $(y - \theta_x \times l_i)$. The rotating speed of the whole system ω is defined as the rotating speed about z-axis. The displacement of the rigid rotor outer surface due to the rotor inclination is omitted here for brevity [48].

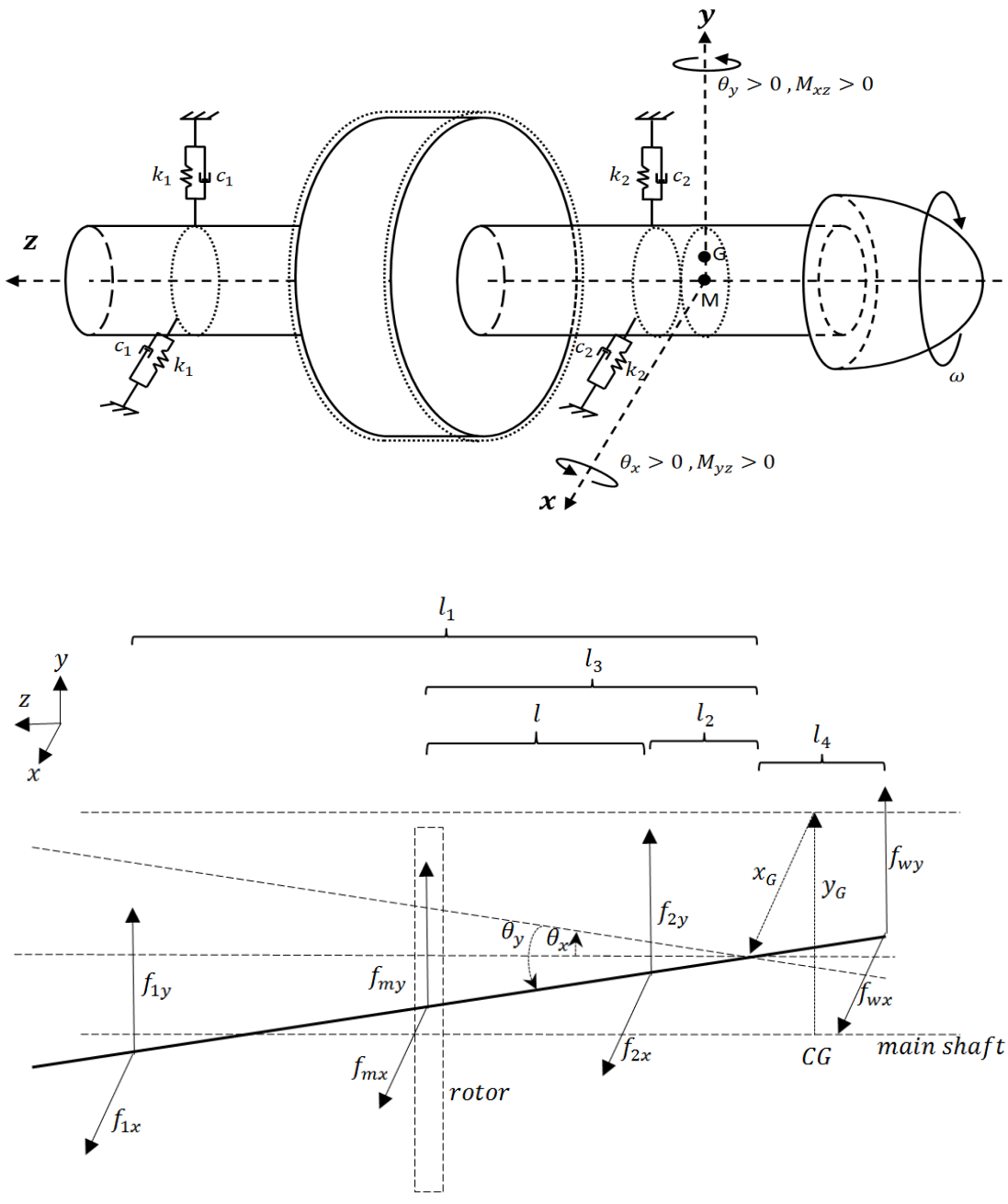

Figure 5-3 Schematic of the rotor system, (a) the drive-train system, (b) the force system.

The displacement of the CG of the rotor system $(\mathrm{x_G}, \mathrm{y_G})$ and the inclination angle $(\theta_{\mathrm{Gy}}, \theta_{\mathrm{Gx}})$ of the rotor system about the CG can be determined by applying Newton's second law of motion using the resultant force $(\mathrm{F_x}, \mathrm{F_y})$ and the resultant moment $(\mathrm{M_x}, \mathrm{M_y})$, as shown in Figure 5-3:

$$\begin{aligned} F_x &= m\ddot{x}_G \\ F_y &= m\ddot{y}_G \\ M_{XZ} &= I\ddot{\theta}_{Gy} + I_p\omega\dot{\theta}_{Gx} \\ M_{YZ} &= I\ddot{\theta}_{Gx} - I_p\omega\dot{\theta}_{Gy} \end{aligned} \qquad (5.1)$$

where M_x and M_y represent the torsional moments in *yz* plane ($M_x = -M_{YZ}$) and *xz* plane ($M_y = M_{XZ}$), respectively.

As shown in Figure 5-3, two bearings provide the spring forces and the damping forces to support the shaft. The UMP force and variable wind force are applied at the rotor centre and the hub centre, respectively. The resultant forces and moments can be obtained as

$$\begin{aligned} F_x &= f_{1x} + f_{2x} + f_{mx} + f_{wx} = (-k_1x_1 - c_1\dot{x}_1) + (-k_2x_2 - c_2\dot{x}_2) + f_{mx} + F_{wx} \\ F_y &= f_{1y} + f_{2y} + f_{my} + f_{wy} = (-k_1y_1 - c_1\dot{y}_1) + (-k_2y_2 - c_2\dot{y}_2) + f_{my} + F_{wy} \\ M_{XZ} &= l_1f_{1x} + l_2f_{2x} + l_3f_{mx} - l_4f_{wx} = l_1\big(-(k_1x_1 + c_1\dot{x}_1)\big) + l_2\big(-(k_2x_2 + c_2\dot{x}_2)\big) \\ &\quad + l_3f_{mx} - l_4F_{wx} \\ M_{YZ} &= l_1f_{1y} + l_2f_{2y} + l_3f_{my} - l_4f_{wy} = l_1\big(-(k_1y_1 + c_1\dot{y}_1)\big) + l_2\big(-(k_2y_2 + c_2\dot{y}_2)\big) \\ &\quad + l_3f_{my} - l_4F_{wy} \end{aligned}$$

(5.2)

where (x_i, y_i) represent the displacements of the rotor at the locations of Bearings 1 and 2 with the relationship $x_i = x + l_i\theta_y$, $y_i = y - l_i\theta_x$, for $i = 1,2$. (f_{mx}, f_{my}) denote the components of the UMP force in *x* and *y* direction according to Eq.(3.1), respectively, and (F_{wx}, F_{wy}) represent the variable wind forces in *x*-axis and *y*-axis directions considered as the external excitation which plays an important role in the rotor dynamics[163].

The wind excitations can be complicated as related to the blade aerodynamics and the control system. Only a simple harmonic force is used to simulate the resultant wind excitation and a similar harmonic form has been widely used in the dynamic analysis of wind turbine systems in the literature. The magnitude and frequency of the fluctuating wind force are adopted from the existing studies [119, 133, 152]. The fluctuating external wind force can be expressed as $F_{wx} = f_{wx}\cos(\omega_w t)$, $F_{wy} = f_{wy}\cos(\omega_w t)$, where f_{wx}, f_{wy} are the magnitudes of the fluctuating force and ω_w is the frequency.

It is known that the CG may not always coincide with the centre of geometry due to the unbalanced mass. Assume that the unbalanced CG has the eccentricity e and the skew angle τ. Eq.(5.1) and (5.2) can be rewritten by using the relationship [164]

$$\begin{aligned} x_G &= x + e\,cos(\omega t) \qquad \theta_{Gy} = \theta_y - \tau\,cos(\omega t + \beta) \\ y_G &= y + e\,sin(\omega t) \qquad \theta_{Gx} = \theta_x - \tau\,sin(\omega t + \beta) \end{aligned} \tag{5.3}$$

where (x, y) represent the displacement of the centre of geometry and (θ_y, θ_x) denote the inclination angles of centre of geometry, ω denotes the rotational speed of the system, and β is the angle between the principal axis and the direction of the unbalanced mass.

By substituting Eq.(5.2) and (5.3) into Eq.(5.1), the equations of motion of the drive-train system can be obtained as

$$\begin{aligned} m\ddot{x} + c_{11}\dot{x} + c_{12}\dot{\theta}_y + k_{13}x + k_{14}\theta_y &= me\omega^2 cos(\omega t) + f_{mx} + f_{wx}\cos(\omega_w t) \\ m\ddot{y} + c_{11}\dot{y} - c_{12}\dot{\theta}_x + k_{13}y - k_{14}\theta_x &= me\omega^2\,sin(\omega t) + f_{my} + f_{wy}\cos(\omega_w t) \\ I\ddot{\theta}_y + I_p\omega\dot{\theta}_x + c_{21}\dot{x} + c_{22}\dot{\theta}_y + k_{23}x + k_{24}\theta_y &= (I_p - I)\tau\omega^2\,cos(\omega t + \beta) + l_3 f_{mx} - l_4 f_{wx} \\ I\ddot{\theta}_x - I_p\omega\dot{\theta}_y + c_{21}\dot{y} - c_{22}\dot{\theta}_x + k_{23}y - k_{24}\theta_x &= (I_p - I)\tau\omega^2\,sin(\omega t + \beta) + l_3 f_{my} - l_4 f_{wy} \end{aligned}$$

(5.4)

where

$$c_{11} = c_1 + c_2 \qquad c_{21} = c_1 l_1 + c_2 l_2$$
$$c_{12} = c_1 l_1 + c_2 l_2 \qquad c_{22} = c_1 l_1^2 + c_2 l_2^2$$
$$k_{13} = k_1 + k_2 \qquad k_{23} = k_1 l_1 + k_2 l_2$$
$$k_{14} = k_1 l_1 + k_2 l_2 \qquad k_{24} = k_1 l_1^2 + k_2 l_2^2$$

The rotor response which depends on the UMP force, unbalanced force and wind force will be studied by performing the numerical simulation using Matlab ODE45 solver, as no analytical solutions can be found for the four second-order nonlinear differential equations.

5.2. Numerical simulation results

Compared to the design of geared wind turbines, the weight adjustment is more important for the direct-drive wind turbines since the total weight of a direct-drive wind turbine has been increased significantly, especially the weight of its generator, which may affect its stability during operation [165, 166]. The adjustment of the rotor weight and position within the direct-drive generator, which will change the location of the CG of the drive-train system. The rotor displacement and bearing forces are discussed under different operating conditions. In performing numerical simulations, the parameters of the drive-train system are selected from the designed DDPMG of a 5 MW NREL wind turbine [9, 88], and are given in Table 5-1. It is known that the DDPMG would operate at a low rotating speed, normally in the range of 5 to 30 rpm. Its average operating speed of the selected model is thus assumed to be 16 rpm.

Table 5-1 System parameters used for the drive-train system [9, 88, 144, 161, 167-169]

Symbol	Description	units	value
m	Total mass of the rotor system	ton	174.68

L	Length of the shaft	m	3
Rs	Inner radius of the stator	m	3.185
Δr	Average air-gap	mm	6.36
h	Length of the magnet	m	1.72
Ip	Polar moment of inertia	$kg \cdot m^2$	3.54×10^7
I	Moment of inertia	$kg \cdot m^2$	1×10^5
p	Number of the pole pairs		60
	Distance along shaft from hub center to Bearing 1	m	2.65
	Distance along shaft from hub center to Bearing 2	m	0.65
	Distance along shaft from hub center to rotor center	m	1.65
$l_{oo'}$	Horizontal distance between the CG of the drive-train system and the CG of the platform	m	2
$h_{oo'}$	Vertical distance between the CG of the drive-train system and the CG of the platform	m	168.61

The numerical simulations are carried out with the rotor system starting from rest (0 rpm) and then accelerating at a constant angular acceleration until it reaches a rated operating speed. After that, it keeps rotating at the rated constant speed to remain a maximum power output. The displacements and the angle inclinations at the initial state (0 rpm) are calculated for the initial values assigned to the variables of the equation. The corresponding initial values in Matlab simulations are not artificially set but calculated

from the initial rest position of the drive-train system (the system is not rotating at the initial state). Specifically, the displacement and angle inclination in the vertical direction (y direction) are calculated by considering the weight and the location of the CG of the drive-train system. The displacement and angle inclination in the horizontal direction (x direction) are set to be 0 because no static loading is applied in these directions. The maximum displacement of the rotor must be not larger than the average air-gap, otherwise, the rotor will have direct contact with the stator and damage the generator. Thus, under a safe operating condition, the displacement of the rotor must be smaller than the average air-gap ($d_r < \Delta r$). However, the displacement of the rotor is unpredictable since it is calculated using the equation $dr = \sqrt{(x + l_3\theta_y)^2 + (y - l_3\theta_x)^2}$, where four variables x, y, θ_y and θ_x are involved. Pitch and other control systems are assumed to be used during the operation of wind turbines, but the interaction of the control systems and the rotor system will not be considered for brevity.

5.2.1. Effect of the rotor position

Since all variables l_{i} are dependent on the location of the CG of the drive-train system, the location of the CG can be an important variable for determining some parameters involved in the equation of motion. The location of the CG can be easily moved by changing the position of the rotor between the two bearings or changing the mass ratio of components within the system. Firstly, the effect of the adjustment on the location of the rotor is studied. As the power level of the studied model is chosen and the size of the wind turbine is determined, the mass of each component included in this model, that is, the rotor mass m_r, main shaft mass m_s, and the mass of hub with blades m_h, is then correspondingly determined. The distance in the axial direction between the centre of the

rotor and the center of Bearing 2 is denoted by l along the z axis. Then l can be analysed from 0 to 2m and the location of the CG and the centre of the rotor have the relationship shown in Figure 5-4. The consideration of 0m and 2m are only for the sake of theoretical analysis, a realistic model would require a specific design for such a condition. For the designed DDPMG, the rotor position is set in the middle of the two bearings, which gives $l = 1.0\text{m}$ and the location of the CG $l_2 = 0.039m$.

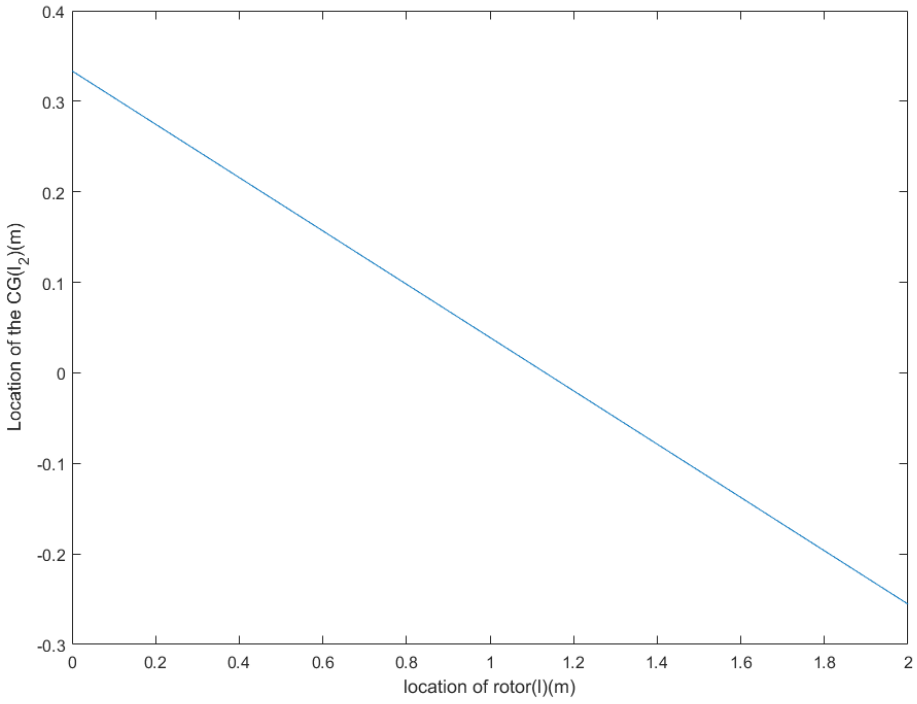

Figure 5-4 Relationship of the rotor position and the location of the CG

Figure 5-5 shows the displacement of the CG and the rotor when $l = 1.0\text{m}$ and the rotating speed is 16 rpm. The rotor displacement decreases after it starts running and converges to small values. The rotor displacement at the steady-state response can be found to be about 0.0204mm, which is within 10% of the average air-gap for a successful operating condition set by the manufacturers. The displacements of the CG and the rotor demonstrate that the steady-state vibration response appears to be a combined spectrum.

Figure 5-6 shows the difference in the rotor response when the UMP force is or not considered in the numerical simulations. An increased response can be clearly found when the UMP force is considered from the figures. The difference between the drive-train system with and without the UMP force considered is found to be around 0.05mm at 16rpm and 0.2mm at 30rpm, which are 7% and 30% of the tolerance allowable (10% of the average air-gap) for a safe operation. Thus, the effect of the UMP is notable and significant in particular at higher speeds, which makes the consideration of the UMP force necessary in vibration analysis. In order to discuss the vibration response due to the adjustment of the rotor position, the variation of the maximum steady-state displacement of the CG and the rotor centre with different locations of the rotor is shown in Figure 5-7. Significant changes can be found in the displacement from Figure 5-7. The peak displacement of the CG when the rotor center moves from Bearing 2 to Bearing 1 is found to have an increase from 0.02mm to 0.21mm, which is approximately increased by 10 times. However, when the rotor center is moving along the shaft from Bearing 2 to Bearing 1, the maximum rotor displacement reduces from 0.12mm and reaches the minimum value of 0.07mm at $l = 0.3\text{m}$, and then is increased to 0.55mm. Since the rotor response is unpredictable, only the FFT spectrum analysis for the displacement in the x direction of the drive-train system's CG is shown in Figure 5-8. The FFT spectrum shows that the vibration of the drive-train system is affected by two main sources. The first peak frequency at 0.267Hz is the response frequency of the unbalanced mass of the rotor system at 16 rpm, the second peak frequency at 0.4807Hz indicates the wind excitation applied in the simulation. Both response frequencies are obviously independent of the rotor position. Thus, the effect of the rotor position adjustment is weak on the change of vibration response frequency and but strong on its displacement amplitude. More detail can be found in Appendix 9.1.

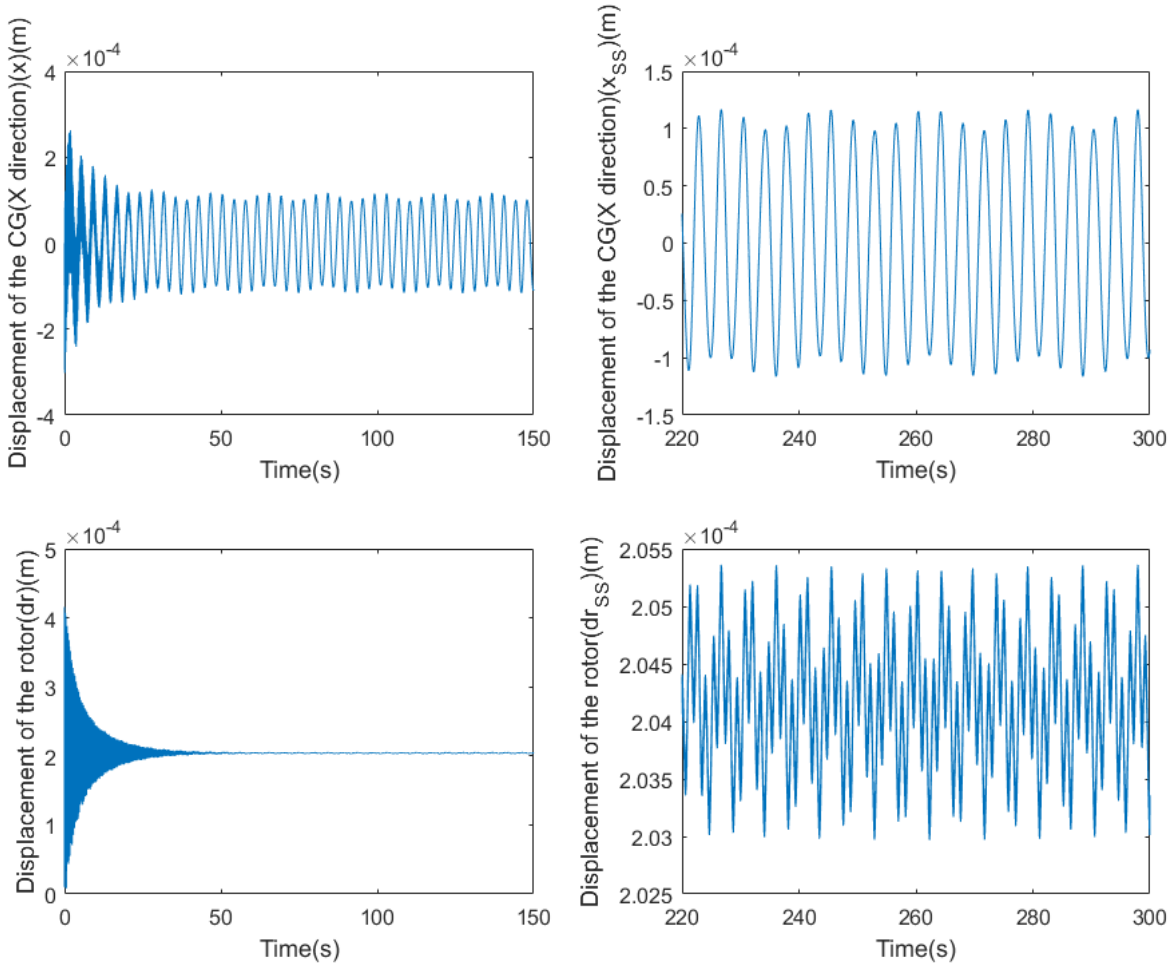

Figure 5-5 Time-history of the displacement of the CG and the rotor when $l = 1.0m$ at 16 rpm. The left and right subfigures show the transient and steady-state response, respectively.

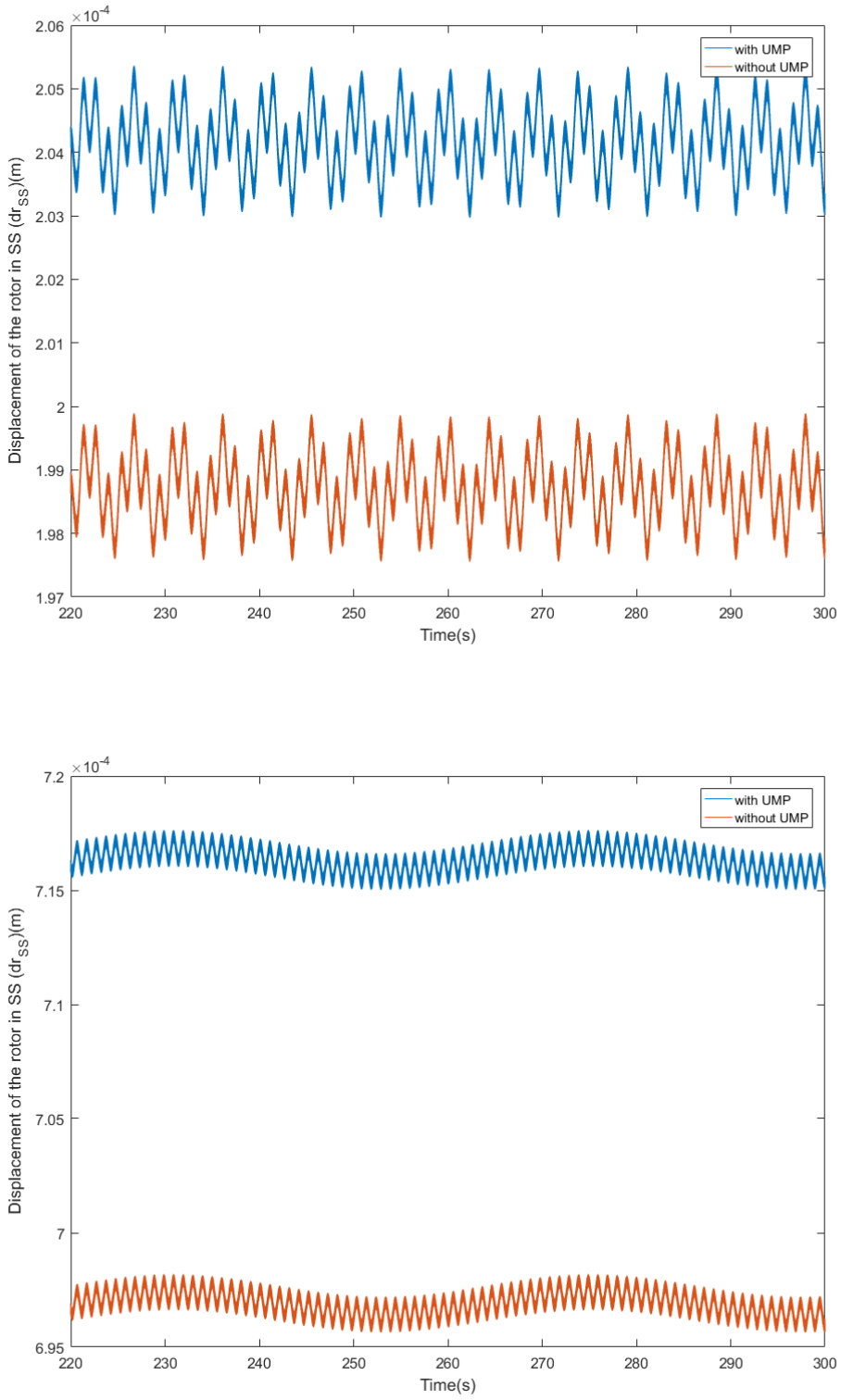

Figure 5-6 Steady state displacement response of the rotor at 16rpm (up) and 30rpm (down) when the UMP force is or not considered.

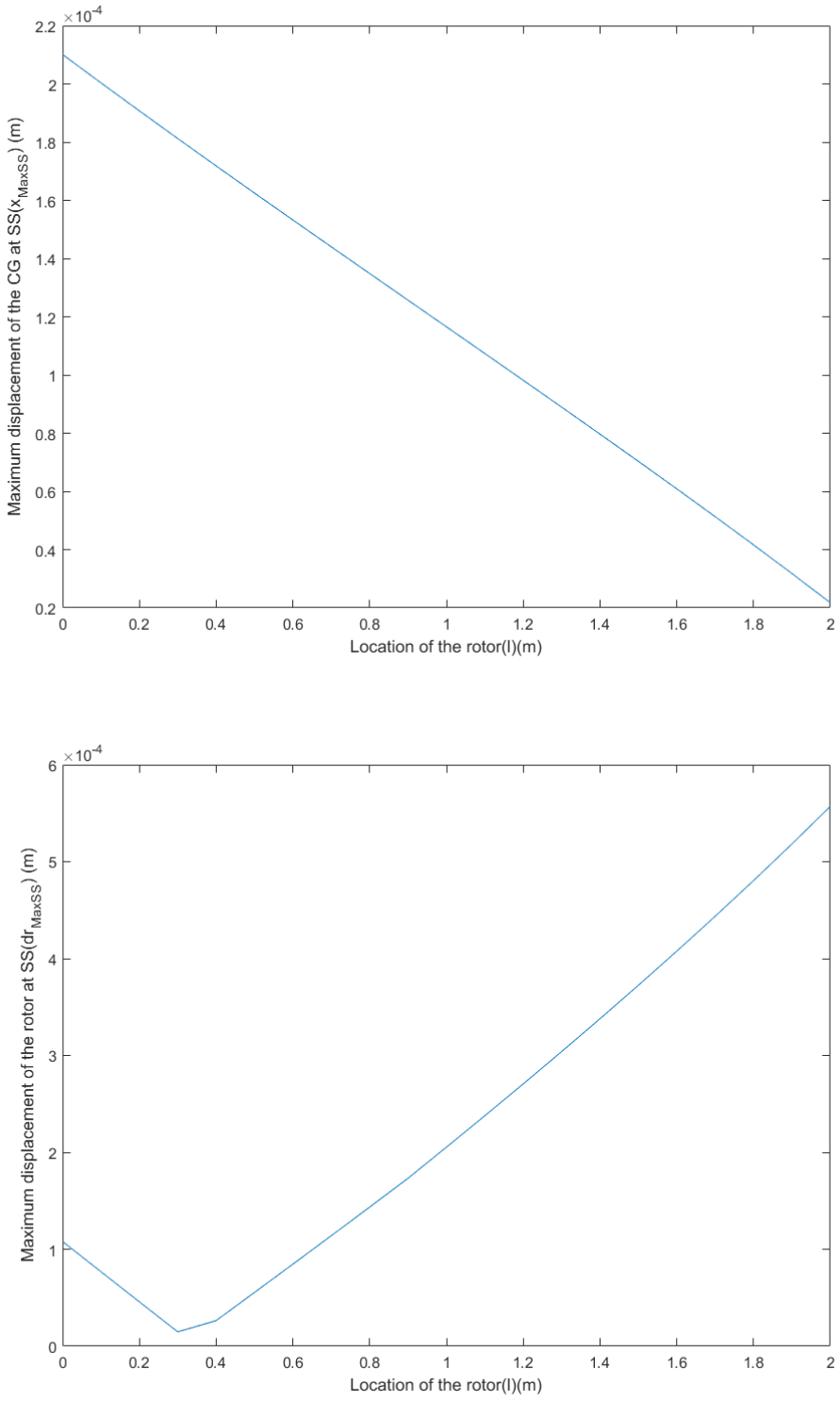

Figure 5-7 Variation of the maximum displacement with different rotor position, (a) the displacement of the CG, (b) the displacement of the rotor centre.

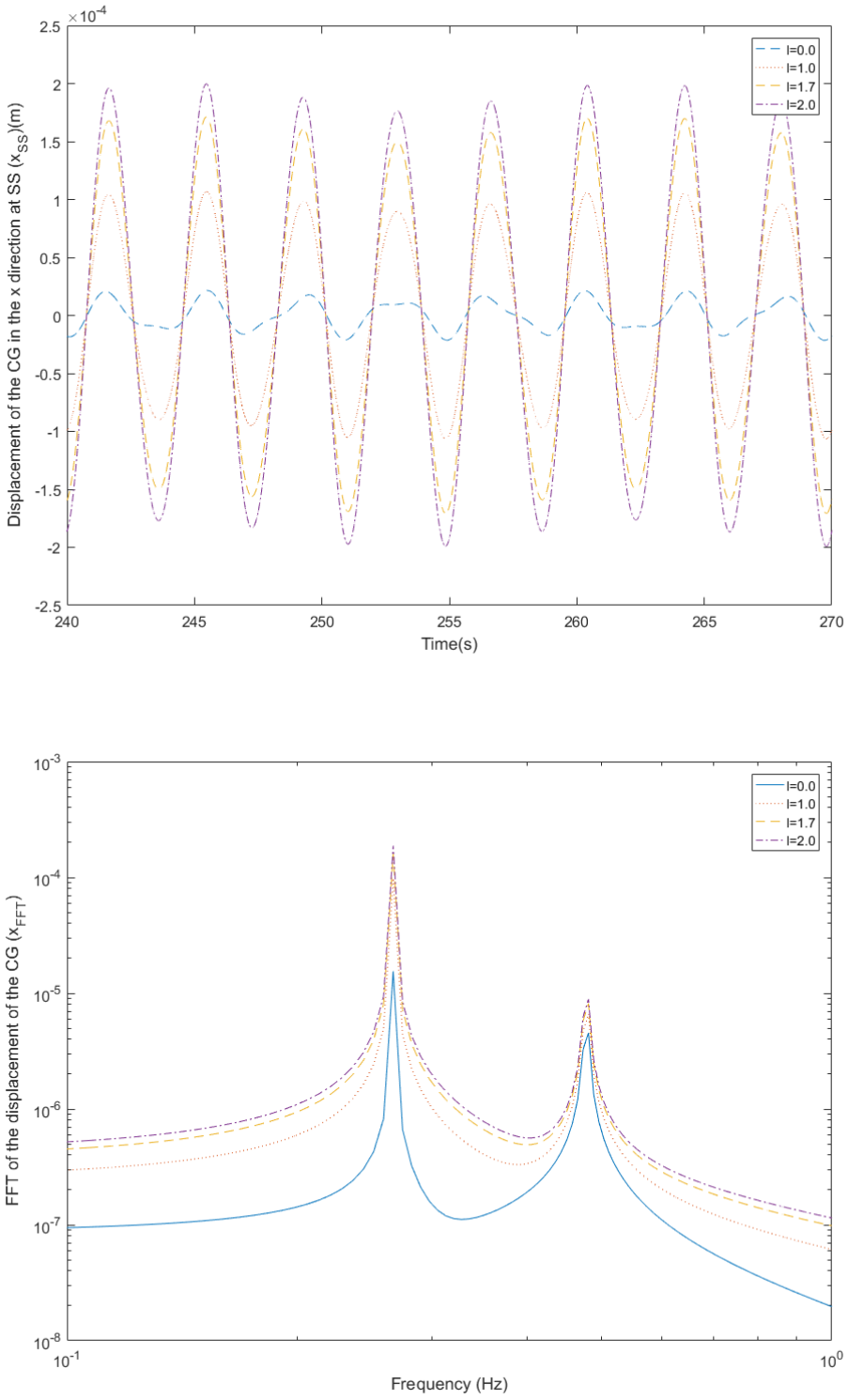

Figure 5-8 Displacements and the corresponding FFT spectra of the CG in the x direction with different length *l*

Figure 5-9 shows the magnitude of the bearing forces acting on Bearings 1 and 2 (BR1 and BR2). It can be seen that the maximum forces on both bearings occur at the beginning stage of the operation and are decreased quickly and settled into the steady-state. The cyclic dynamic loads at the steady-state can be useful for calculating the fatigue life of bearings. A comparison of the peak force magnitudes in the transient state indicates that Bearing 2 takes more radial load than Bearing 1, but the difference between the forces applied on the bearings has been reduced at the steady-state. Both bearings are taking about $1.7 \times 10^7 N$ force at the steady-state. Figure 5-10 demonstrates the change in the maximum bearing force along the rotor position. The maximum force response at Bearing 1 increases approximately in a quadratic manner when the rotor moves along the shaft from Bearing 2 to Bearing 1. For Bearing 2, the maximum bearing force decreases first and then increasing after reaching its minimum value at l=1.2m.

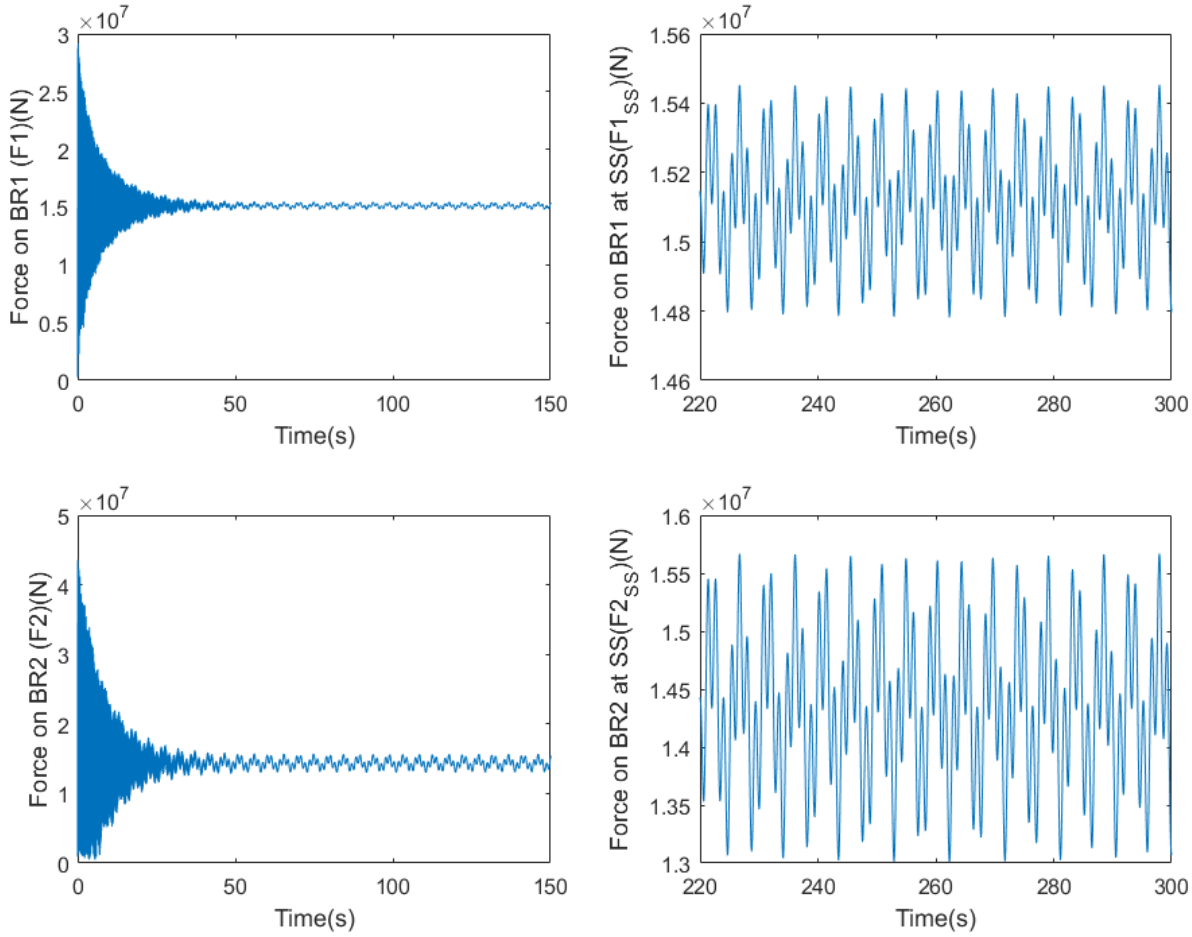

Figure 5-9 Bearing force response at 16 rpm, (a) force on Bearing 1, (b) force on Bearing 2. The left and right subfigures show the transient and steady-state response, respectively.

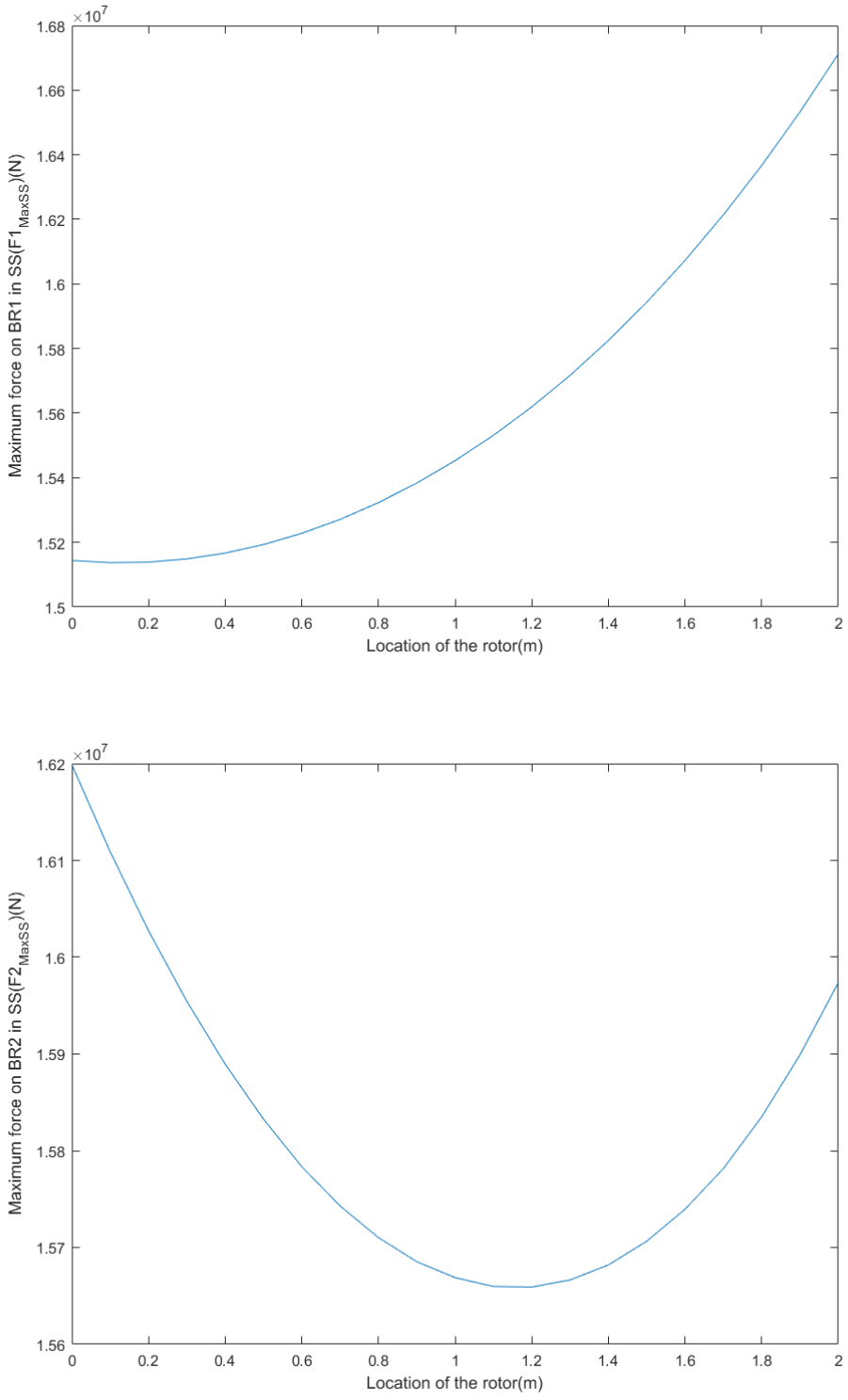

Figure 5-10 Maximum steady-state bearing forces with different l, (a) force on Bearing 1, (b) force on Bearing 2.

One major difference between the direct-drive and indirect-drive (geared) wind turbines is the rotating speed of the generator. The effect of the rotor adjustment will be discussed subsequently under different rotating speeds of the generator of the direct-drive wind turbines. By selecting $l = 1.0m$, the rated operating speed is chosen from 5rpm to 30rpm, both displacement response and bearing forces are analyzed. The maximum displacement and the bearing forces under overall operating conditions are the same from 5rpm to 30rpm as the simulation starts from 0 rpm. The maximum displacement and bearing forces appear at the beginning stage of the operating process. The maximum steady-state displacement and bearing forces with different l are shown in Figure 5-7 and 5-10.

It is rational to compare the vibration response under different conditions by combining the results with the two variables, where the displacement and force responses at the steady-state are shown from Figure 5-11 to 5-14.

Figure 5-11 to 5-13 demonstrate the maximum value of the rotor displacement and bearing forces at the steady-state response at certain speeds with variable l. By considering the limitation of the air-gap between the rotor and stator for a safe operation, the optimized rotor position can be chosen when the rotor centre is 0.3m measured from Bearing 2 along the shaft. However, by considering the bearing loading response, different rotor position can be chosen to minimize the cyclic dynamic load and increase their fatigue life. For Bearing 1, the minimum cyclic loads are found when the rotor is close to Bearing 2, while for Bearing 2, the minimum cyclic loads appear when $l = 1.2$m. It can be seen from Figure 5-14 that the adjustment of rotor position at the higher speeds has larger effect on the displacement response than that at the lower speeds. However, it is also noticed that in some cases the maximum rotor displacements exceed the 10% of the average air-gap (designed value) but still in a workable condition ($\mathrm{d_r} < \Delta r$).

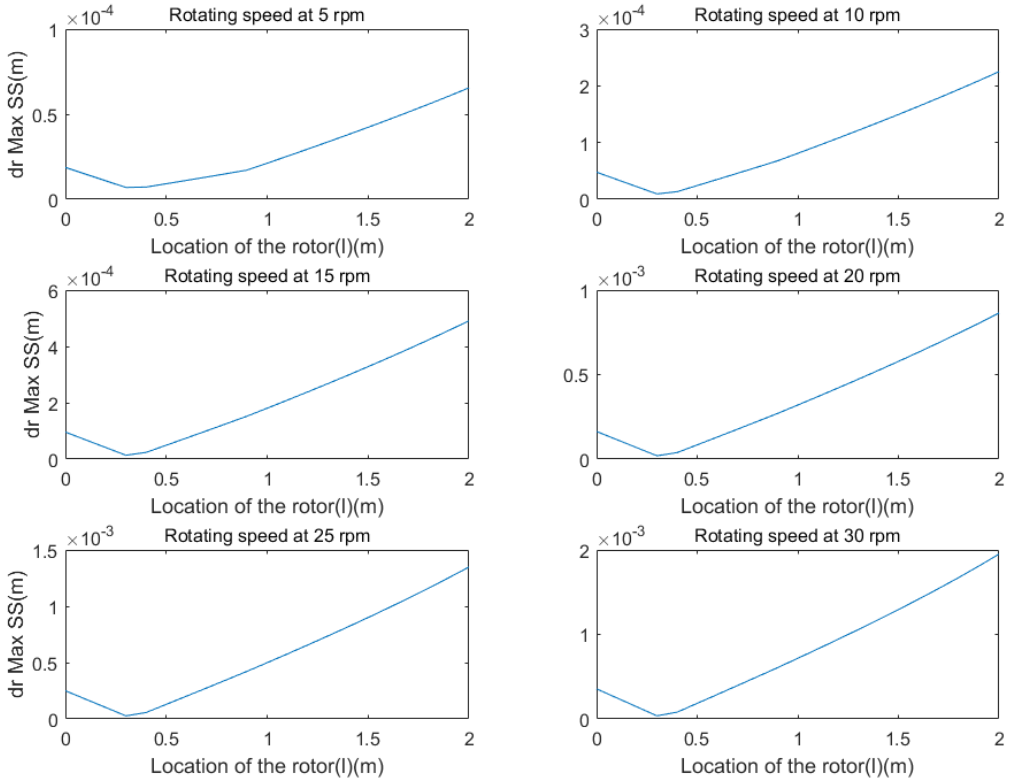

Figure 5-11 Variation of the maximum steady-state displacement response of the rotor at certain speeds with variable l

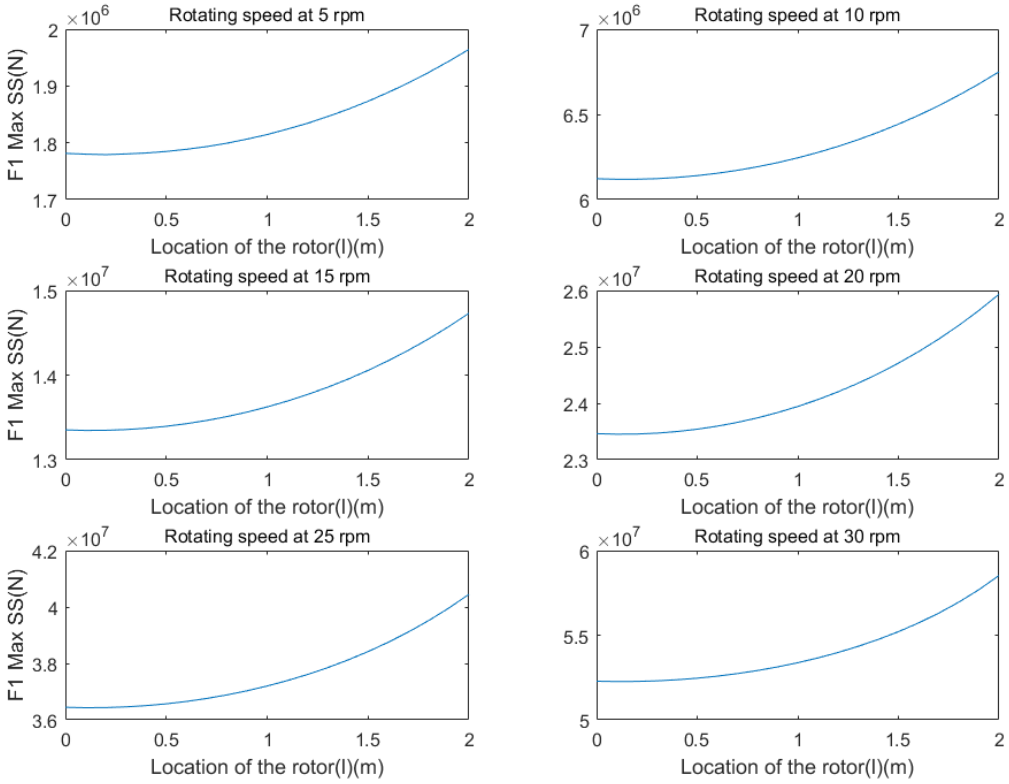

Figure 5-12 Variation of the maximum force response on Bearing 1 at the steady-state at certain speeds with variable l

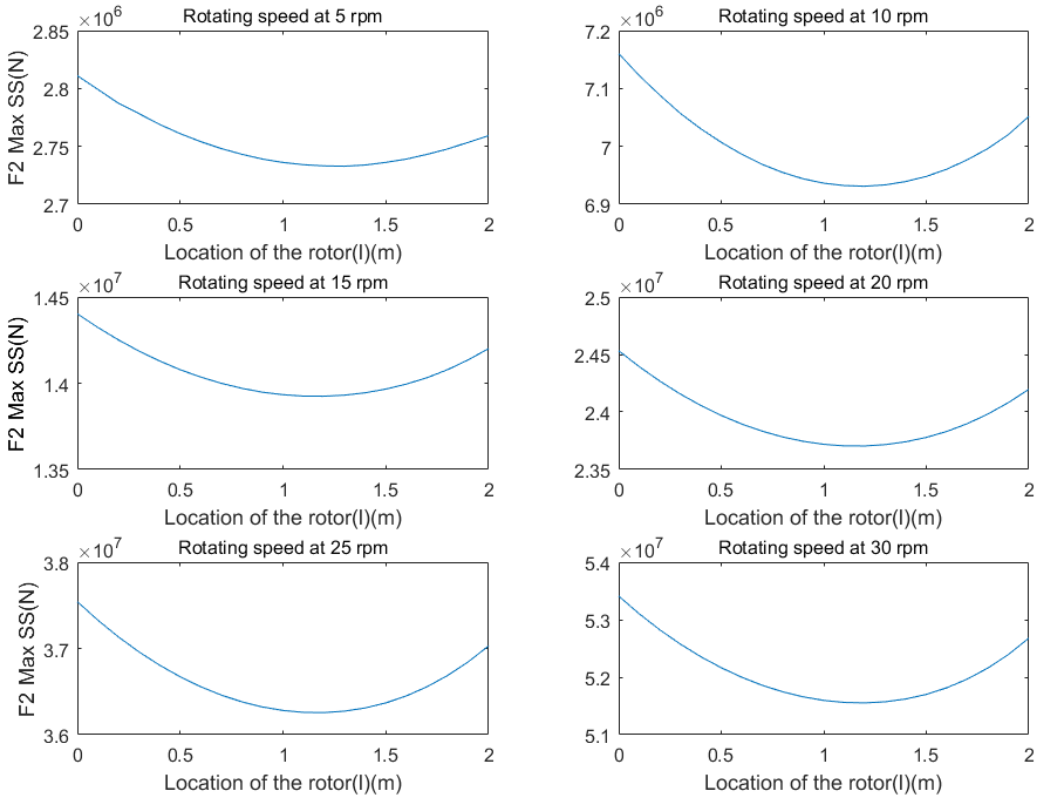

Figure 5-13 Variation of the maximum force responses on Bearing 2 at the steady-state at certain speeds with variable l

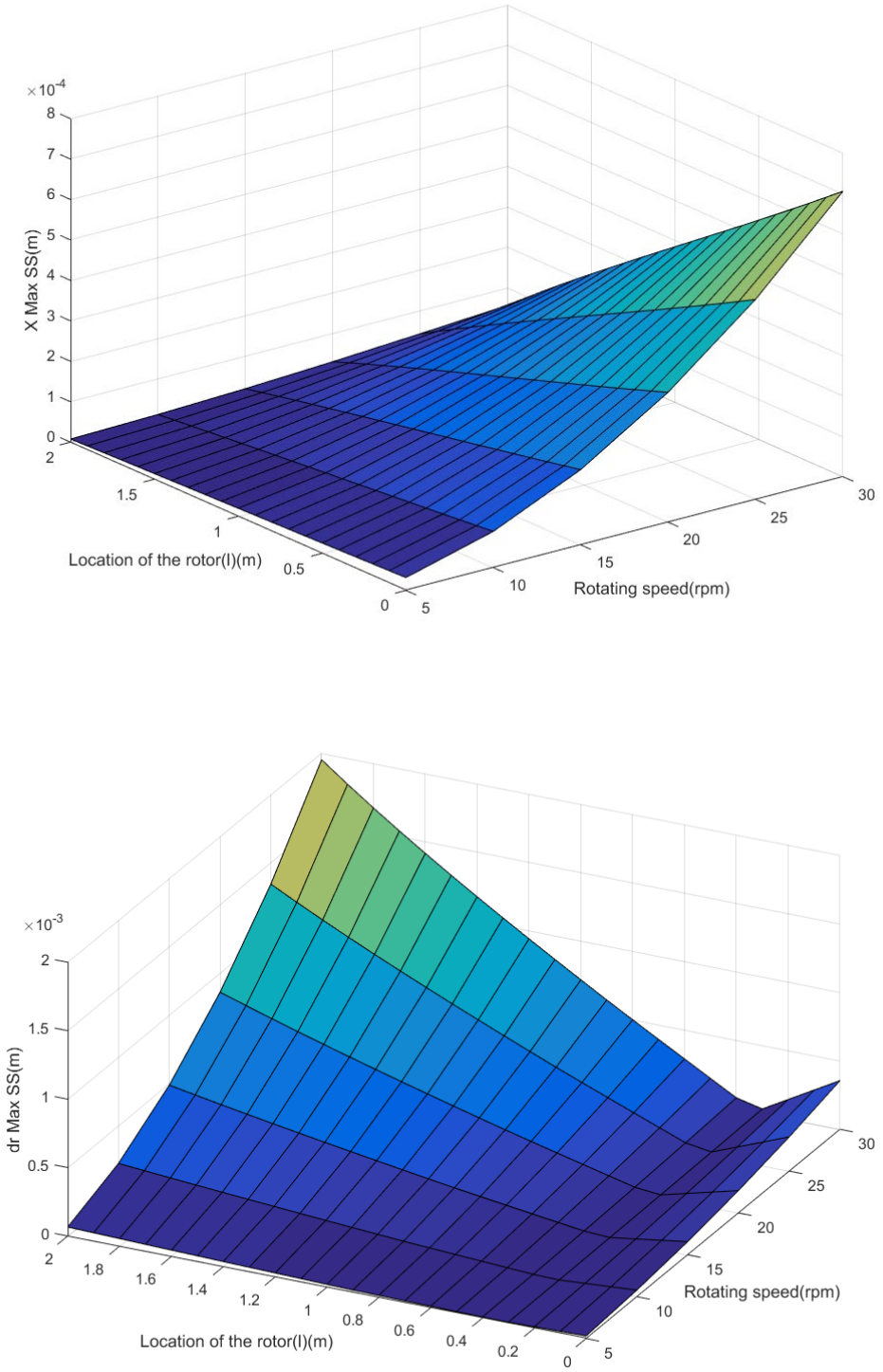

Figure 5-14 Maximum steady-state displacement response of the CG and the rotor under different l and rotating speeds

5.2.2. Effect of the mass ratio

Another method to change the location of the CG within the drive-train system is by changing the mass ratio between the three mass components in the system. As mentioned above, there are three mass components, namely, the rotor mass m_r, main shaft mass m_s and the mass of hub with blades m_h. For the chosen 5MW DDPMG model studied in this thesis, without significant changes of its structure, the blade length is fixed in order to remain the power output. Thus, the mass of hub with blades m_h and main shaft mass m_s are determined and cannot be changed. However, the mass of the rotor m_r can be variable by choosing different structures (for example, rim structure) and materials, thus the location of the CG can be changeable with the rotor mass. The other parameters in the system such as total mass, moment of inertia and even the initial condition will also be changed accordingly. The rotor mass can be found between 30 ton to 90 ton available for the rotor support with a fixed outer radius. The relationship between the mass ratio, $m_r/(m_s+m_h+m_r)$, and the location of the CG can be calculated and is shown in Figure 5-15.

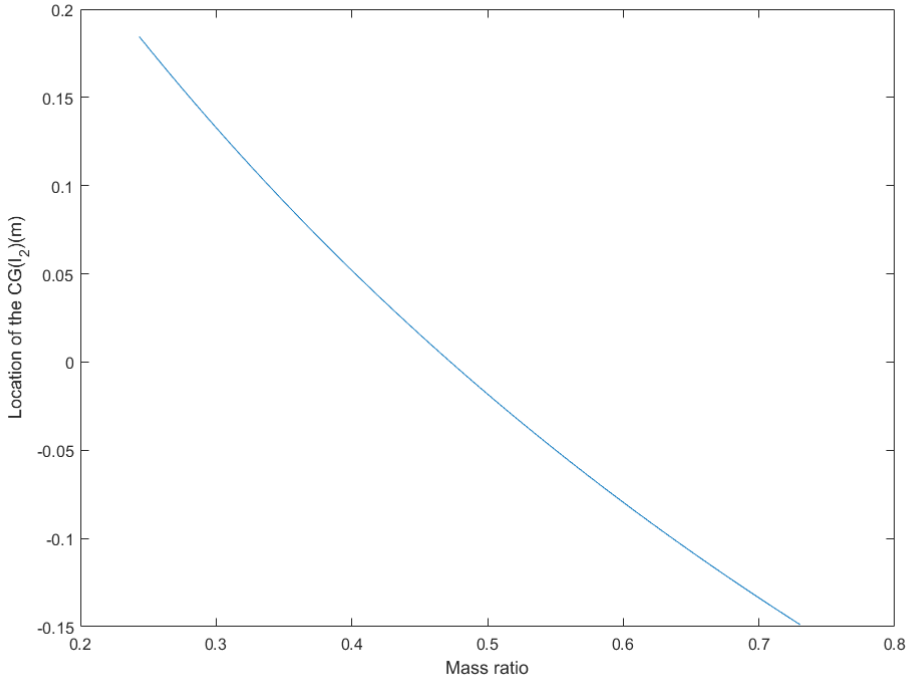

Figure 5-15 Relationship of the mass ratio and the location of the CG of the drive-train system

The maximum displacement and force response at the steady-state with different mass ratios and the related FFT spectra are shown in Figure 5-16 and 5-17. Although the maximum displacement of the CG reduces when the mass ratio increase, the maximum displacement of the rotor increases along with its weight. Figure 5-17 also shows the changes of the maximum bearing forces acting on both bearings with different mass ratios at the steady-state. It is found that an increase of mass ratio (heavier rotor mass) would lead to an increase maximum force response on Bearing 1 but a decrease force response on Bearing 2 at the steady-state. The FFT spectrum analysis for the displacement of the CG in the x direction also shows two frequency peaks. It is also clear that the effect of the mass ratio on the dynamic response at high speeds (about 4% of the average maximum displacement) is higher than its effect at low speeds (about 1% of the average maximum displacement) from Figure 5-18. Although the effect of the rotor mass adjustment is weak when compared to its position adjustment, the simulation results can still give optimized

options on the mass adjustment for a safe operation. A selection of a lighter weight rotor cannot only reduce the maximum displacement of the rotor, but also the force response applied on Bearing 1, however, it will result in an increasing force response on Bearing 2.

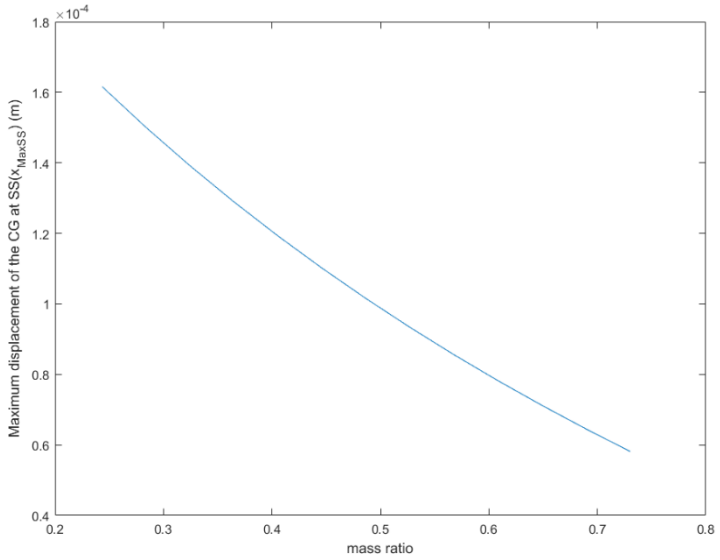

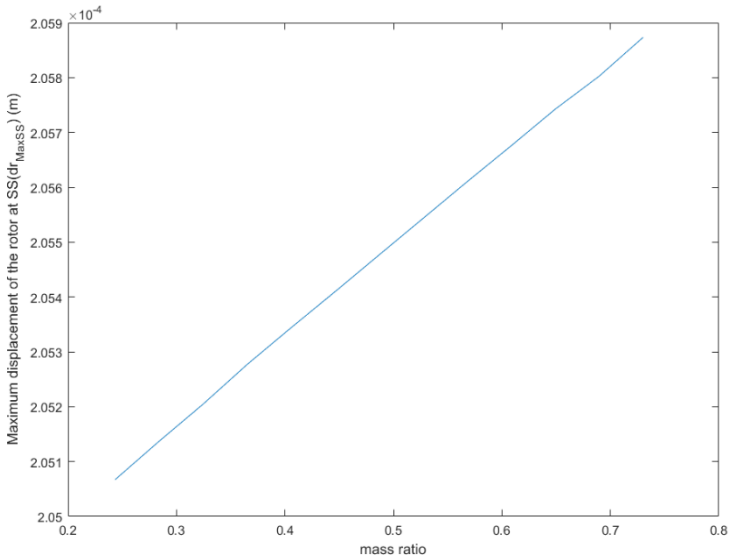

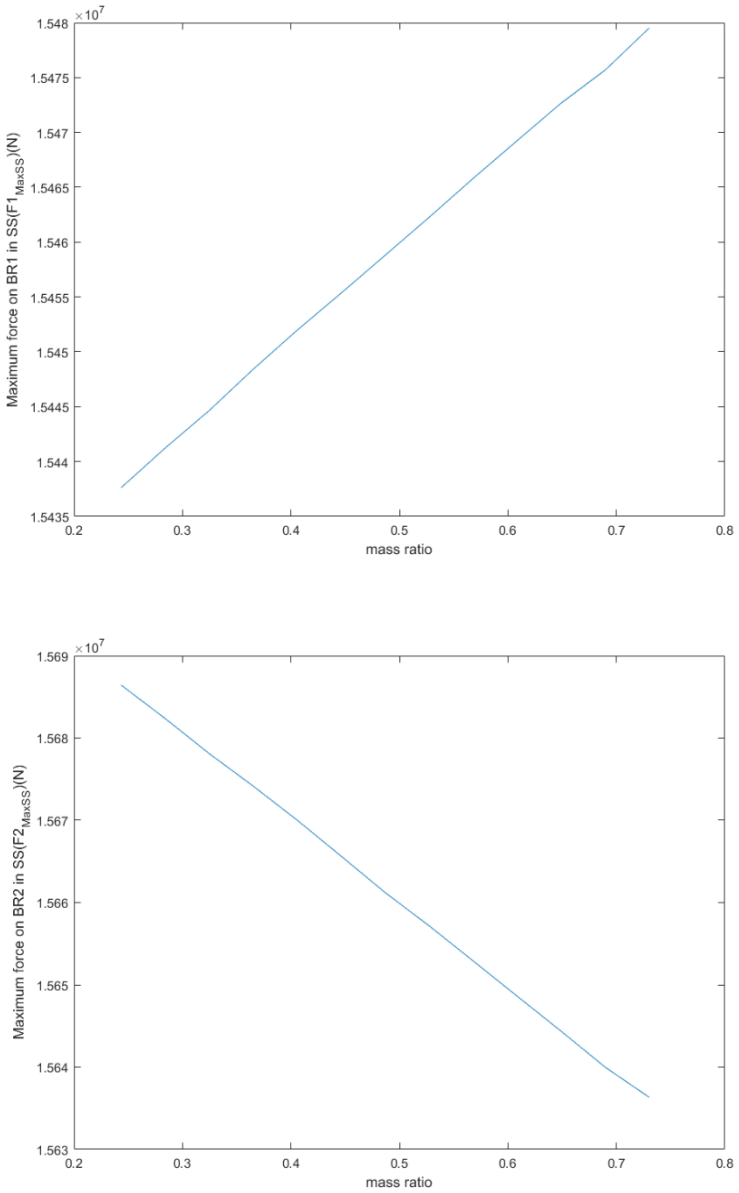

Figure 5-16 Maximum rotor displacement response and the force response on the bearing with different mass ratios

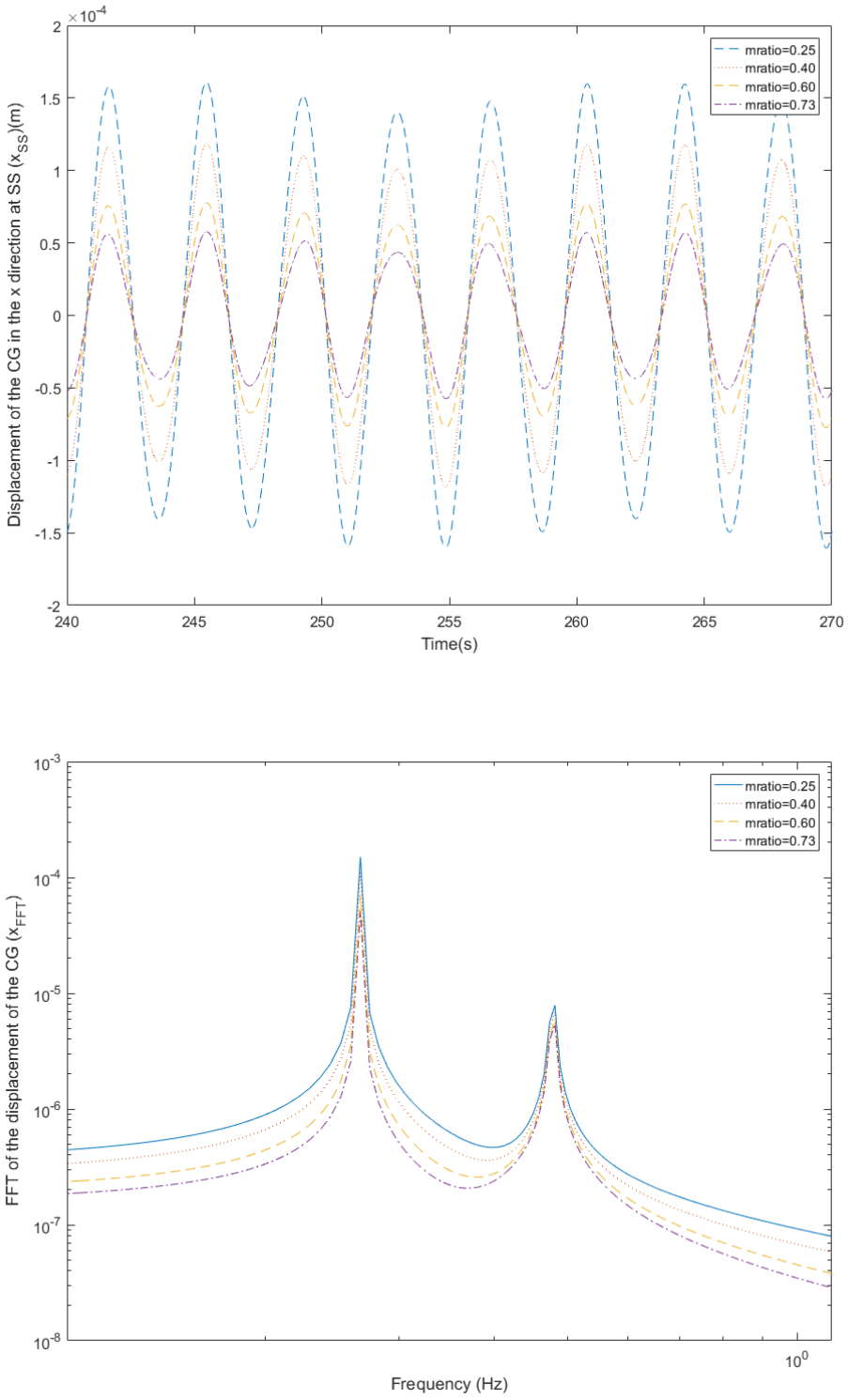

Figure 5-17 Displacement in the x direction of the CG with different mass ratio and the related FFT spectrums at 16rpm rotating speed

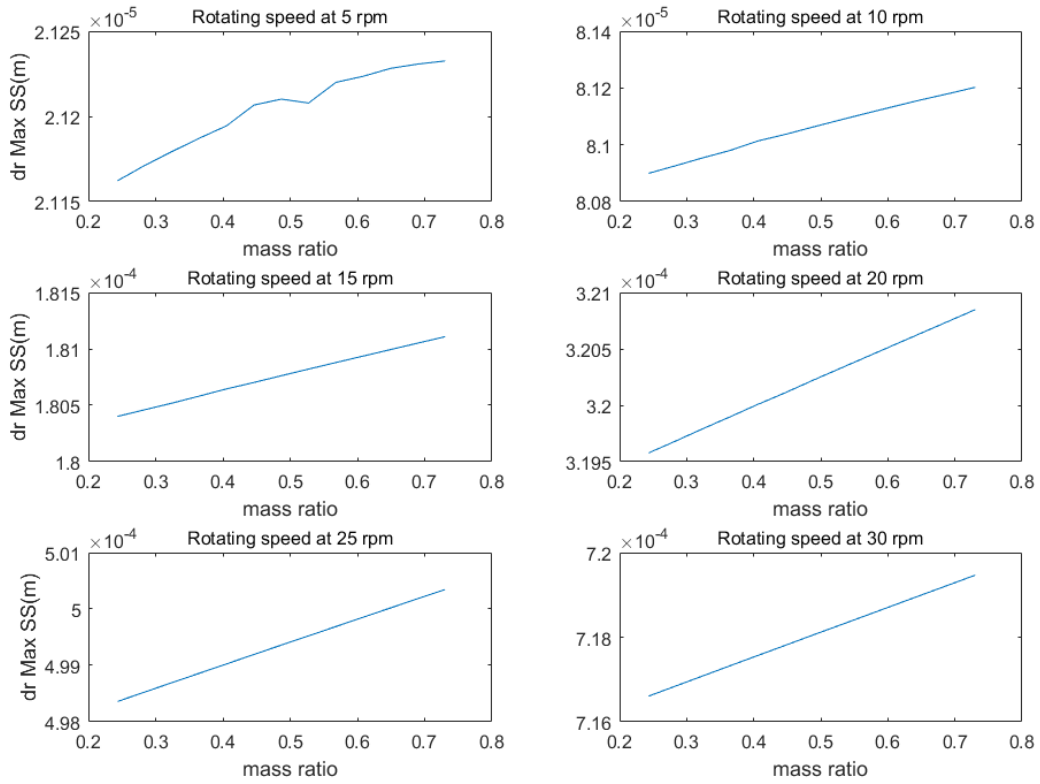

Figure 5-18 Variation of the maximum rotor displacement response with the mass ratio under different rotational speed

5.3. Conclusion

The vibration behaviour of the drive-train system within a direct-drive wind turbine has been studied for different locations of the centre of gravity of the drive-train system, which are caused by the adjustment of rotor position and rotor mass. The dynamic model developed is a 4DOF nonlinear system and includes the wind excitation and the non-linear unbalanced magnetic pull force (UMP force) in the generator. The rotor displacement and bearing loads have been obtained for different rotor positions along the shaft and different rotor mass ratios under different rotating speeds. The maximum rotor

displacement and the maximum cyclic loads on the bearings were discussed for a wide range of operating conditions.

The comparison results of the model with and without the UMP force indicate an up to 30% notable difference in the allowable tolerance of air-gap under a workable operation, which makes the consideration of the UMP force necessary in the dynamic analysis of the drive-train system for direct-drive wind turbines. The effect of the UMP force on the dynamic response of the drive-train system is more significant when the rotational speed of the drive-train system is higher.

The vibration response of the drive-train system was found to be related to its rotor position and mass ratio. According to the simulation results, the effect of the rotor position adjustment could give significant change on its displacement magnitude but less change on the response frequency, while the effect of the rotor mass adjustment is not as significant as the effect of the rotor position adjustment. An optimized design of the adjustment of rotor position and mass ratio would improve the performance of the drive-train system, such as the reduction of bearing loads.

6. Platform vibration of the spar type wind turbines

Different types of offshore wind turbines have been developed for their advantages of more power output and less space limitation than the land-based wind turbines. The distinct offshore environmental loads may significantly affect the dynamic response of the offshore wind turbines.This chapter will study the dynamic response of a spar-type direct-drive wind turbine under different excitations.

6.1. Theoretical model

The NREL 5 MW wind turbine, a catenary moored spar-type direct-drive wind turbine, is chosen as it has been widely used in studying the vibration behaviour of offshore wind turbines [9, 19, 87, 88]. The spar-support platform is a shaped cylinder with ballast inside and mooring system attached on it. A simple sketch of the model is shown in Figure 6-1. A total of 8 DOF system, which consists of 4 DOF free-free end model of the wind turbine structure and 4 DOF model of the drive-train system, will be developed for investigating the effects of hydrodynamic and aerodynamic excitations on the dynamic response of the spar-support floating direct-drive wind turbine. Two coordinate systems, a moving-local (X, Y, Z) coordinate system and a fixed-global (X', Y', Z') coordinate system, are used to describe the motion of the drive-train system and the motion of the floating platform with tower structure. The nacelle is considered as a non-rotating mass point fixed at the top of the tower at first, only the thrust force from the blades will be considered. Then the rotating interaction between the drive-train system and the nacelle will be discussed.

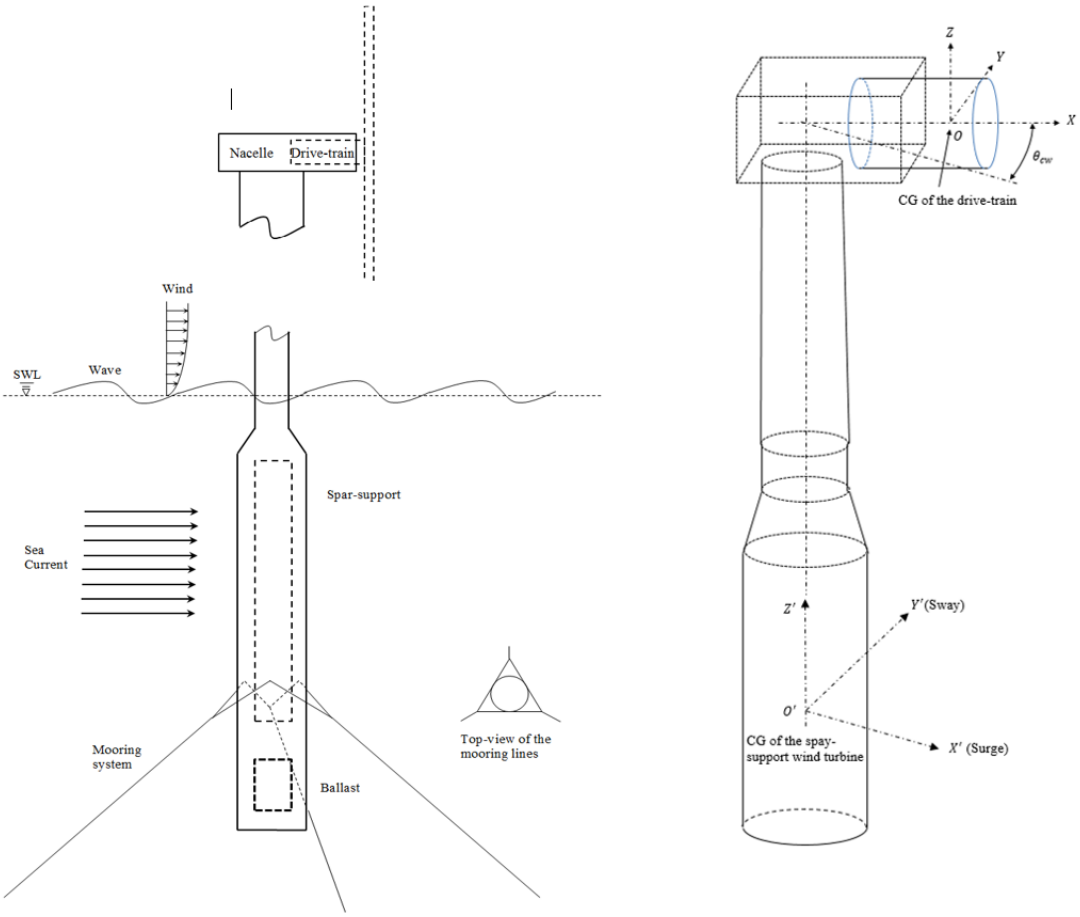

Figure 6-1 A simple sketch of the spar-support wind turbine and the global and local coordinate systems

This chapter aims to present a simplified approach to study the vibration behaviour due to the aerodynamic and hydrodynamic excitations on the wind turbine. As a result, a number of assumptions are made to focus on the primary points without redundancies:

1. The spar-support platform with tower structure is considered as a rigid long floating body under deep-sea condition.
2. External excitations considered acting on the model are generated from sea current, wave, wind, mooring and buoyancy.
3. Only displacements and the inclination angles of the platform with tower structure in surge and sway directions are discussed, while the displacement in heave direction is ignored.

4. The wave direction is the same as the wind direction, except for the case of misalignment to be considered.
5. The current direction is assumed to be in the surge direction. However it is also noticed that the wind and wave direction may not always be the same as the current direction, so the effect of the angle between the wind, wave and current directions θ_{wc} is introduced to reflect the difference in directions.
6. The dynamic effects associated with the mass, damping, and fluid acceleration on the mooring lines are neglected.
7. Only normal operational conditions are studied and the fault condition is not considered for the wind turbine system.

6.1.1. The dynamic model of the drive-train system

A nonlinear system of 4 DOF (y, z, θ_y, θ_z) in a moving-local (X, Y, Z)-coordinate system with origin at the centre of gravity (CG) of the drive-train system is used to describe the motion of the drive-train system. The equations of motion of the drive-train system can be obtained from Section 5.1 as

$$
\begin{aligned}
m\ddot{y} + c_{11}\dot{y} + c_{12}\dot{\theta}_z + k_{13}y + k_{14}\theta_z &= me\omega^2 cos(\omega t) + f_{my} + f_{wy}\, cos(\omega_w t) \\
m\ddot{z} + c_{11}\dot{z} - c_{12}\dot{\theta}_y + k_{13}z - k_{14}\theta_y &= me\omega^2\, sin(\omega t) + f_{mz} + f_{wz}\, cos(\omega_w t) \\
I\ddot{\theta}_z + I_p\omega\dot{\theta}_y + c_{21}\dot{y} + c_{22}\dot{\theta}_z + k_{23}y + k_{24}\theta_z &= (I_p - I)\tau\omega^2\, cos(\omega t + \beta) + l_3 f_{my} - l_4 f_{wy} \\
I\ddot{\theta}_y - I_p\omega\dot{\theta}_z + c_{21}\dot{z} - c_{22}\dot{\theta}_y + k_{23}z - k_{24}\theta_y &= \big(I_p - I\big)\tau\omega^2\, sin(\omega t + \beta) + l_3 f_{mz} - l_4 f_{wz}
\end{aligned}
$$

(6.1)

where

$$
\begin{aligned}
c_{11} &= c_1 + c_2 & c_{21} &= c_1 l_1 + c_2 l_2 \\
c_{12} &= c_1 l_1 + c_2 l_2 & c_{22} &= c_1 l_1^2 + c_2 l_2^2 \\
k_{13} &= k_1 + k_2 & k_{23} &= k_1 l_1 + k_2 l_2 \\
k_{14} &= k_1 l_1 + k_2 l_2 & k_{24} &= k_1 l_1^2 + k_2 l_2^2
\end{aligned}
$$

The vibration of the drive-train system will be incorporated into the dynamic model of the spar-type platform to study the dynamic interaction induced response in the wind turbines.

6.1.2. The dynamic model of the spar-type platform with tower structure

The spar-type platform with tower structure is assumed to be a rigid body for the sake of simplicity. A 4-DOF system (x', y', $\theta_x{}'$, $\theta_y{}'$) is used to describe the motion of the platform in the fixed-global (X', Y', Z')-coordinate system. The coordinates (x', y') define the translational motion of the spar-supported tower in X' and Y' directions, respectively. The coordinates ($\theta_x{}', \theta_y{}'$) indicate the rotational motion of the platform about X' and Y' directions. Many studies have assumed that the damping ratio of the system to be 2%. The damped and un-damped natural frequencies of the system would be equal for such a low critical damping ratio. By using the Newton's Second Law of Motion, the equation of motion for the platform with tower structure can be written as:

$$
\begin{aligned}
m'\ddot{x}' &= F_{current\_x'} + F_{wind\_x'} + F_{wave\_x'} + F_{mooring\_x'} + F_{interaction\_x'} \\
m'\ddot{y}' &= F_{current\_y'} + F_{wind\_y'} + F_{wave\_y'} + F_{mooring\_y'} + F_{interaction\_y'} \\
I'\ddot{\theta_{y'}} &= M_{current\_y'} + M_{wind\_y'} + M_{wave\_y'} + M_{mooring\_y'} + M_{bounacy\_y'} + M_{interaction\_y'} \\
I'\ddot{\theta_{x'}} &= M_{current\_x'} + M_{wind\_x'} + M_{wave\_x'} + M_{mooring\_x'} + M_{bounacy\_x'} + M_{interaction\_x'}
\end{aligned}
\tag{6.2}
$$

where m' and I' are the total mass and moment of inertia of the wind turbine including the nacelle (as a point mass). The interaction forces and moments are the equivalent response generated from the force response in the drive-train system, which can be expressed as

$$F_{interaction_{x'}} = f_x cos\theta_{cw} + \sum f_{iy}\, sin\theta_{cw}$$
$$F_{interaction_{y'}} = f_x sin\theta_{cw} + \sum f_{iy}\, cos\theta_{cw}$$
$$M_{interaction_{y'}} = (f_x cos\theta_{cw} + \sum f_{iy}\, sin\theta_{cw})h_{oo'} - \sum f_{iz}\,(l_{oo'} + l_i)sin\theta_{cw}$$
$$M_{interaction_{x'}} = -(f_x sin\theta_{cw} + \sum f_{iy}\, cos\theta_{cw})h_{oo'} + \sum f_{iz}\,(l_{oo'} + l_i)cos\theta_{cw}$$

$for\ i = 1,2,3$ (6.3)

where f_x represents the thrust force on the drive-train system, (f_{ix}, f_{iy}) denote the force response at the specific position (Bearing 1, Bearing 2 and the generator), $l_{oo'}$ and $h_{oo'}$ are the horizontal and vertical distances between the CG of the drive-train system and the CG of the platform respectively.

In substituting the equation of motion of the drive-train system in the local coordinate system into the global coordinate system, the displacement of the drive-train system has a relationship as

$$\begin{aligned} y &= y_{local} - y_{global} \qquad \theta_z = \theta_{z\_local} - \theta_{z\_global} \\ z &= z_{local} - z_{global} \qquad \theta_y = \theta_{y\_local} - \theta_{y\_global} \end{aligned} \tag{6.4}$$

where

$$y_{global} = y' + l_{oo'}\,\theta_{z'} \qquad \theta_{z\_global} = \theta_{z'}$$
$$z_{global} = z' + h_{oo'}(2 - cos\,\theta_{y'} - cos\theta_{x'}) \qquad \theta_{y\_global} = \theta_{y'}$$

When the drive-train system is modelled as a point mass, only 4 DOFs in the global coordinate system will be considered and Eq.(6.2) will be used to show the motion of the platform with tower structure. Only thrust force on the drive-train system will be transformed to the top of the tower, the interaction forces and moments in Eq.(6.2) will be equal to 0. In this case, no dynamic interaction between the drive-train system and tower structure will be considered. When the interaction between the drive-train system and the nacelle is induced, the dynamic force between the drive-train system and the nacelle will be considered as external forces for the tower structure. By substituting

Eq.(6.4) into Eq.(6.1) and combining Eq.(6.1) and (6.2), the equations of motion with 8 DOFs for the whole wind turbine can then be numerically solved in Matlab. Accordingly, the dynamic response of the wind turbine can be examined.

The main components and system parameters of a 5MW direct-drive wind turbine studied in this thesis, such as the platform, the tower and the drive-train system, are adapted from the designed NREL 5MW wind turbine with DDPMG[9, 19, 144, 161]. The spar-support platform is considered as a cylinder structure with a length of 120m. The main parameters of the structure are shown in Table 5-1 and 6-1. It is a non-uniform mass structure since the ballast is located within the structure to lower the CG in order to reduce the vibration of the system. The whole structure is then considered as a rigid body and the self-deflection is ignored. Mooring system is regarded as a spring system with variable stiffness related to its displacement.

Table 6-1 The main parameters of the spar-support wind turbine

Description	units	Value
Total weight (wind turbine)	kg	8,329,230
Pitch inertia about the CG (wind turbine)	$kg{\cdot}m^2$	2.2×10^{10}
Hub height	m	90
Spar-supported length above SWL	m	10
Spar-supported length below SWL	m	120
Top diameter of the spar-support above SWL	m	6.4
Top diameter of the spar-support below SWL	m	9.0

Location of mooring below SWL	m	70
Location of CG below SWL	m	78.61
Location of buoyancy below SWL	m	60
Drag coefficient	-	0.6
SWL: Sea Water Level		

6.2. External excitations

6.2.1. Aerodynamic excitation

Aerodynamic excitations, mainly in the form of wind excitations, acting on the wind turbine are discussed in two parts, the tower and the blades. For the wind excitation on the tower part, the long-term variability of wind force can be simply calculated by using a mean wind speed. A common wind shear model is used to represent the mean speed,

$$V_{(z)} = V_H(\frac{z}{H})^{\alpha} \qquad (6.5)$$

where $V_{(z)}$ is the mean wind speed at the altitude z, V_H is the reference wind velocity at the reference altitude H (normally $H = 10$ m), α is the wind shear exponent ($\alpha = 0.11$). The drag force of fluids passing through structure is given by:

$$F_w = \frac{1}{2}\rho_a {V_{r(z)}}^2 C_d A_{(z)} \qquad (6.6)$$

where ρ_a is the air density, $V_{r(z)}$ is the relative velocity of the wind and the structure, C_d is the drag coefficient of the structure and $A_{(z)} = d_e \times dz$ is the equivalent characteristic surface area. The spar's motion is normally assumed to be small and thus the relative velocity at elevation z is close to its wind velocity $V_{r(z)} \approx V_{(z)}$.

For the wind excitation on the blades, not only a thrust force but also a high torque in the generator would be generated. The thrust force can be transformed directly to the tower through the drive-train system, while radial forces can be produced due to rotational motion induced by the high torque. The radial force response of the drive-train system is normally generated at the bearings (bearing forces) and rotor-stator position (UMP). In order to control the rotating operation and the torque generated, a blade-pitch control system is widely used to limit the above-rated rotating speed. Since the electrical and control system will not be modelled and discussed in this thesis, the drive-train system is assumed to operate at the rated rotating speed corresponding to the wind speed. For the above-rated wind speed, the rotating speed will be limited at the rated speed by using the blade-pitch control system. The turbine cut-in and cut-out wind speeds are 4m/s and 25m/s, and the rated rotating speed is set at 12rpm. When the wind speed is beyond the cut-out speed, the drive-train system would stops rotating in order to survive under extreme weather conditions. The tower shadow can be ignored in some cases [30], thus the blade and tower interaction will not be discussed here. The blade model has been simplified and the blade parameters of the blade were implemented into the software HAWC2 [9, 19]. The rotating speed of the blades and the thrust force from the blades to the drive-train system corresponding to the wind speed are shown in Figure 6-2.

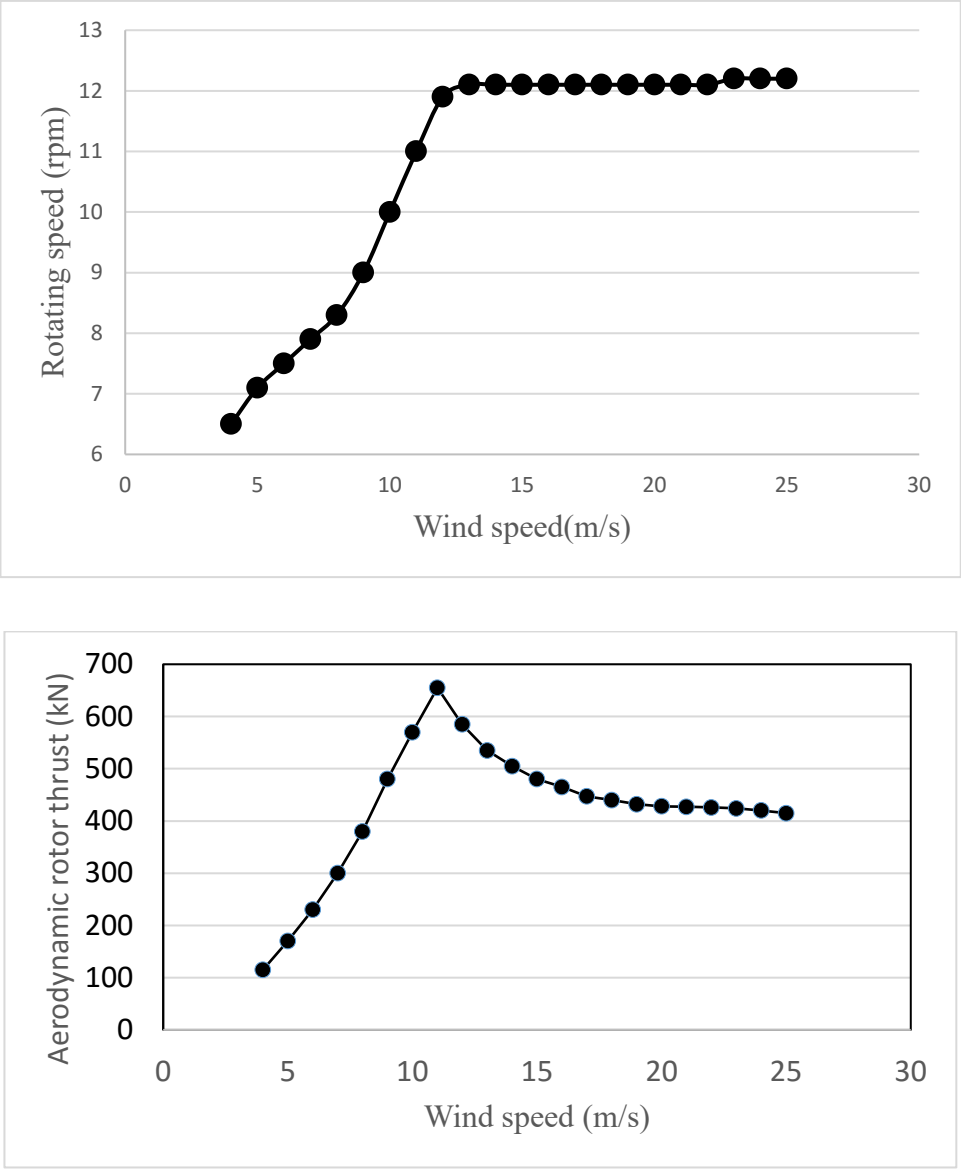

Figure 6-2 Thrust force from the blades to the drive-train system and the resultant rotating speed: (a) rotating speed; (b) thrust force [9, 19]

6.2.2. Hydrodynamic excitations

The hydrodynamic excitations of the offshore wind turbine mainly come from wave, current and buoyancy, which will be discussed in the following subsections.

6.2.2.1. Wave excitation

As assumed in this thesis, the waves are generated by wind and can be derived using the linear wave theory. The JONSWAP spectrum is used as introduced in Section 3.3.1. The long-term variability of wave loads can be defined by two wave spectral parameters: the significant wave height (H_s), and the peak period (T_p). Johannessen *et al.* [114] used a Weibull distribution to describe the significant wave height and a lognormal distribution to introduce its peak period, which was correlated with the given mean wind speed at 10 m height and the significant wave height. The expected value of the significant wave height and the expected value of the peak period can be calculated by using Eq.(3.4) and (3.5).

The wave model will be considered with different wind speeds to investigate the dynamic response of the wind turbine under three main wind conditions; weak, moderate and strong winds. The wind and wave conditions for all cases are given in Table 6-2.

Table 6-2 Parameters for wind and sea conditions

V_{mean} (m/s)	H_s(m)	T_p(s)	Condition
8	2.52	9.848	weak
11	3.01	10.037	
14	3.55	10.267	
16	3.94	10.437	moderate
17	4.14	10.908	
21	4.98	11.023	

25	5.88	11.321	
30	7.1	11.9	strong*
* Drive-train system has stoped rotating			

A JONSWAP spectrum is used to describe the wave and takes the form of

$$S_{\eta\eta}(\omega) = \frac{5}{16} H_s^2 \omega_p^4 \omega^{-5} \exp\left[-\frac{5}{4}\left(\frac{\omega_p}{\omega}\right)^4\right] \gamma^{\exp\left[-\frac{(\omega-\omega_p)^2}{2\sigma^2\omega_p^2}\right]} \qquad (6.7)$$

where η is the function of water surface elevation, γ is the peak enhancement factor ($\gamma = 3.3$ for deep-sea), $\omega_p = \frac{2\pi}{T_p}$ is the peak wave frequency, $\omega = \frac{2\pi}{T_m}$ is the circular wave frequency and T_m is the mean wave period. The spectrum defines a stationary Gaussian process with its standard deviation being equal to 1. The mean wave period T_m and the zero-up-crossing wave period T_z are related to its peak period T_p and its peak enhancement factor γ, as follows

$$\begin{matrix} T_p = 1.2859 T_z \\ T_m = 1.0734 T_z \end{matrix} \text{ for } \gamma = 3.3 \qquad (6.8)$$

and

$$\sigma = \begin{cases} 0.07 & \omega \leq \omega_p \\ 0.09 & \omega > \omega_p \end{cases} \qquad (6.9)$$

The total wave force acting on the spar-support can be calculated by the equation

$$f_{wave}(t) = \int_0^{d_w} p(z,t)\, dz \qquad (6.10)$$

where d_w is the water depth (from the SWL to sea bed), z is the vertical coordinate axis, $p(z,t)$ is the wave force acting on the structure which can be calculated by using the linearized Morison equation

$$p(z,t) = K_d\sqrt{\frac{8}{\pi}}\sigma_v v(z,t) + K_m a(z,t) \qquad (6.11)$$

with

$$K_d = \frac{1}{2}C_d\rho_w d_e \qquad (6.12)$$

$$K_m = \frac{1}{4}C_m\rho_w \pi d_e^2 \qquad (6.13)$$

where C_d is the drag coefficient, C_m is the inertia coefficient, d_e is the equivalent characteristic diameter of spar-support and ρ_w is the sea water density. According to the linear dispersion relationship [170], the wave property under deep-water condition follows

$$\frac{d_w}{\lambda} > \frac{1}{2} \qquad (6.14)$$

and the relation of the circular wave frequency and the wave number can be found as

$$\omega^2 \approx \text{gk} \qquad (6.15)$$

$$\lambda = \frac{2\pi}{k} \qquad (6.16)$$

where k is the wave number and λ is the wave length. The relationship of the horizontal velocity $v(z,t)$ and acceleration $\dot{v}(z,t)$ of the water particle in the deep-water environment and the wave elevation can be determined by using the linear wave theory,

$$v(z,t) = T_v(z)\eta(t) \quad (6.17)$$

$$\dot{v}(z,t) = T_a(z)\dot{\eta}(t) \quad (6.18)$$

where

$$T_v(z) = \omega e^{kz} \quad (6.19)$$

$$T_a(z) = \omega^2 e^{kz} \quad (6.20)$$

The standard deviation of the velocity at altitude z (from the SWL) can be obtained as

$$\sigma_v(z) = \left[\int_0^{\omega} |T_v(z)|^2 S_{\eta\eta}(\omega)\, d\omega\right]^{1/2} (6.21)$$

Substituting the relevant terms into Eq. (6.10) yields the total wave force acting on the structure,

$$f_w(t) = \left\{\int_0^{d_w} \left[K_d \sqrt{\frac{8}{\pi}} \sigma_v(z) T_v(z) + K_m T_a(z)\right] dz\right\} \eta(t) \quad (6.22)$$

A sample function of the random water surface elevation can be descripted by the trigonometric polynomial [171] as

$$\eta(t) = \sum_{k=1}^{n} \sqrt{S_{\eta\eta}(\omega) d\omega}\, (A_{1k} \cos(\omega_k t) + A_{2k} \sin(\omega_k t)) \quad (6.23)$$

where A_{1k}, A_{2k} for $k = 1,2, \dots, n$ are mutually independent standard normal variables and $\omega_{k+1} = \omega_k + \Delta\omega$, with $\Delta\omega$ being an infinitesimal frequency step. A truncation at the upper frequency ω_u can be made to neglect the small variance at higher frequency on the residual contribution, where $\int_{\omega_u}^{\infty} S_{\eta\eta}(\omega) d\omega \ll 1$. In this thesis, the upper frequency is set $\omega_u = 2\pi$, which gives $\int_{\omega_u}^{\infty} S_{\eta\eta}(\omega) d\omega \approx 0.00013$ and the resulting regularity factor $\int_1^{\omega_u} S_{\eta\eta}(\omega) d\omega \approx 0.3461$ for moderate condition. Other general parameters are the air density $\rho_a = 1.2\ kg/m^3$ and sea water density $\rho_w = 1029\ kg/m^3$. The PSDF for the three wind conditions is shown in Figure 6-3. The resulting time history of the surface

elevation of the sea and the loads on the platform under moderate condition is displayed in Figure 6-4. More detail can be found in Appendix 9.2.1. It is noted that the wave at low sea surface level would lead to a backward direction force acting on the structure (due to linear wave theory). The same irregular wave under certain sea conditions will be used to investigate both the relative effect of different excitations on wind turbine and the effect of the interaction between the drive-train system and the platform with tower structure.

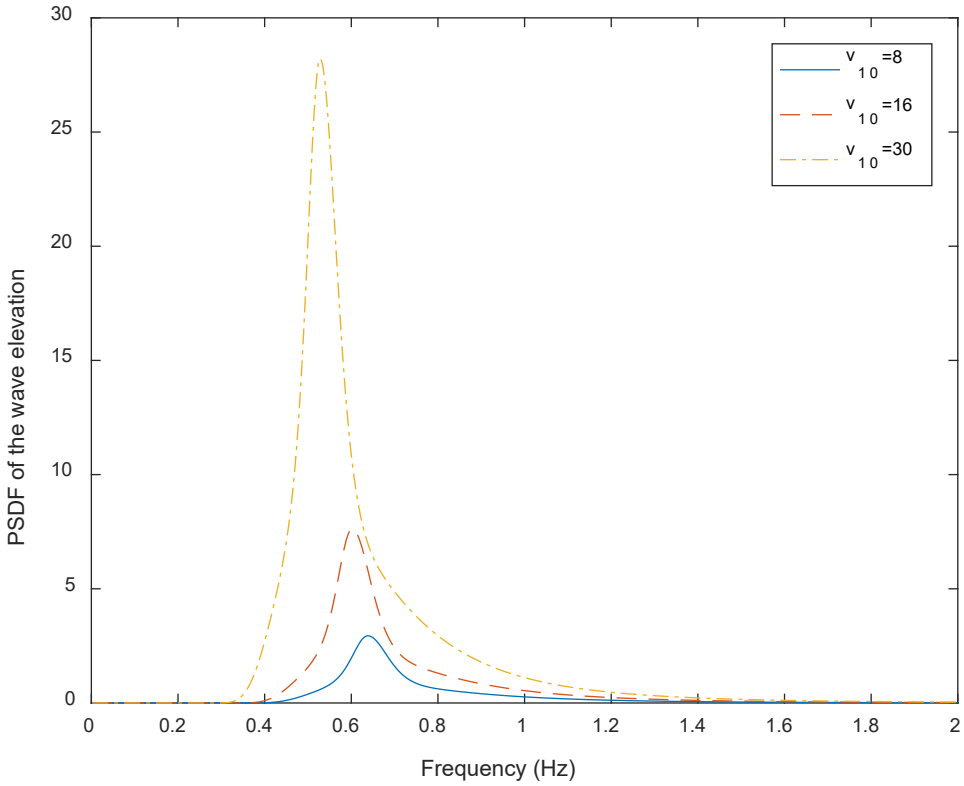

Figure 6-3 PSDF of the wave under different sea conditions

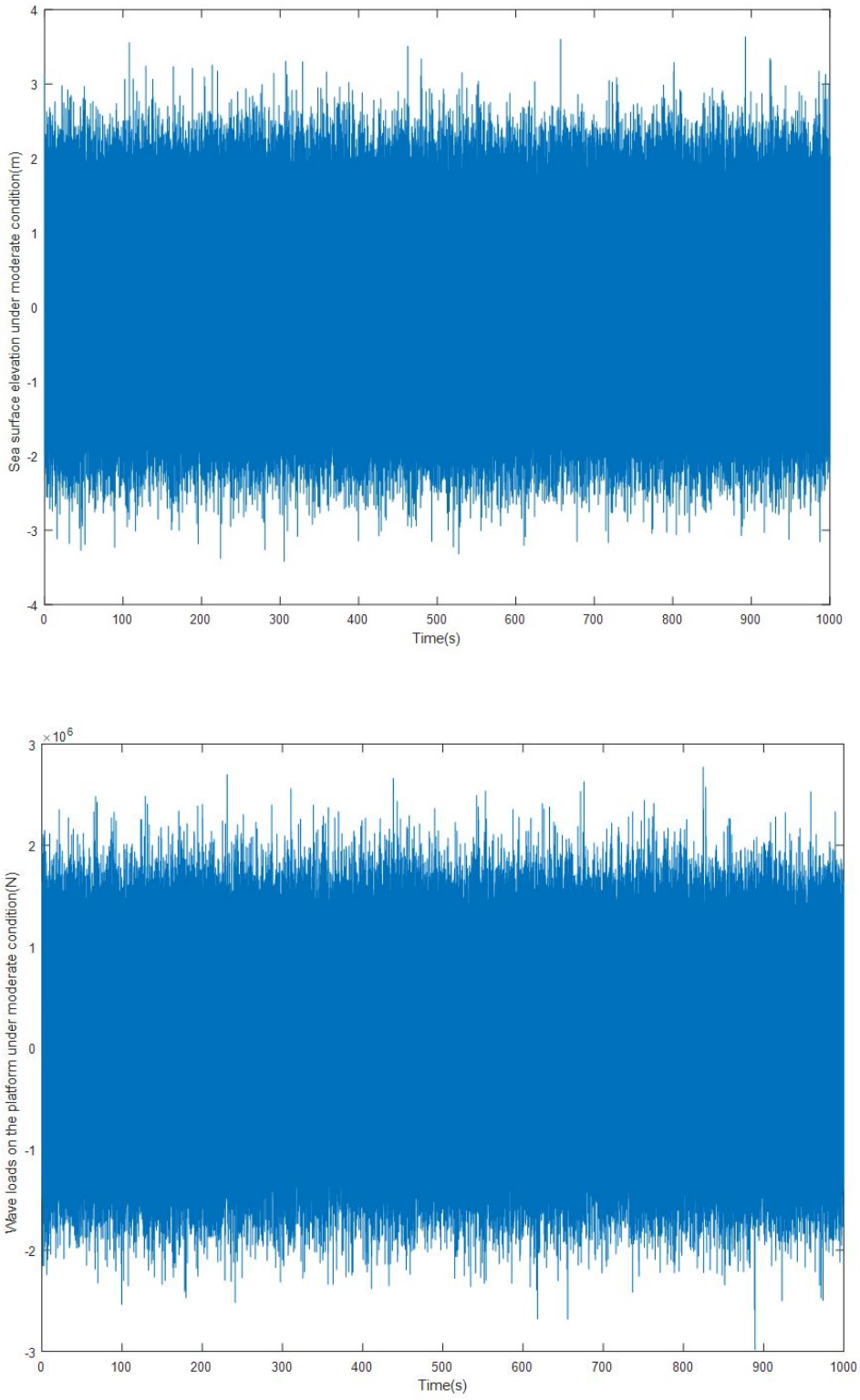

Figure 6-4 Time history of the random surface elevation of the sea and the loads on the platform under moderate condition

6.2.2.2. *Current excitation*

For a long structure sitting in an offshore environment, the current load can be an important source of hydrodynamic damping in some cases [76]. The sea current is a complex component varying with the sea depth, global location, time and other factors. To simplify the effect of the current loads on the model, an average current velocity of $V_c = 0.9m/s$ with a fixed direction is used in the present work. The force per unit length acting on the spar can be predicted by using the Morison equation as,

$$F_c(z) = \frac{1}{2}\rho_w C_d {V_{rc}}^2 d_e(z) + \frac{\pi}{4}\rho_w C_m \dot{V_{rc}} d_e(z)^2 \qquad (6.24)$$

where ρ_w is the sea water density, V_{rc} is the relative velocity of the current and the structure, C_d and C_m are the drag coefficient and inertia coefficient of the structure and d_e is the equivalent characteristic diameter of the cylinder structure. It is normally assumed that the spar's motion is small and thus the relative velocity at elevation z is close to its sea current velocity $V_{rc} \approx V_c$.

6.2.2.3. *Buoyant forces*

The buoyant force is the only force to support the whole wind turbine floating on the sea level, and is variable due to the change in longitudinal force and the sea surface. As made in the assumption, the displacement in the heave direction is ignored, the buoyant force would be balanced by the weight of the structure and the force in the heave direction. As mentioned, the center of buoyancy lower than the CG of the wind turbine due to the ballast, can help to achieve its stability. Thus the effect of the buoyant force on the moment of the spar-support for small angle inclination cannot be ignored and will be investigated. The buoyant force and resultant bending moment can be calculated as,

$$F_{buoyancy\_z'} = m'g + F_{interaction\_z'}$$
$$M_{buoyancy\_x'} = F_{buoyancy\_z'} \times l_{b-CG} \times \theta_{x'} \quad (6.25)$$
$$M_{buoyancy\_y'} = F_{buoyancy\_z'} \times l_{b-CG} \times \theta_{y'}$$

where l_{b-CG} is the distance between the center of buoyancy and the CG of the wind turbine.

6.2.3. Mooring system

The parameters of mooring system is adapted from Karimirad and Moan's design [19] and require no modification in this present study. Table 6-3 summarises the mooring parameters and Figure 6-5 gives a brief introduction of the mooring system. Three sets of mooring lines are attached on the circumference of the spar with two segments for each. The segments are used to provide yaw stiffness. Each adjacent line is 120 degree apart, the resultant stiffnesses of the surge motion and sway motion are different. The force-displacement relation of such a mooring system acting on the spar-support is simulated by using DEEPC [9], as shown in Figure 6-6.

Table 6-3 Mooring system properties [9]

Description	units	value
Sea depth	m	320
Depth to mooring line attached on the spar below SWL	m	70.0
Radius to mooring lines from platform centreline	m	853
Un-stretched mooring line length	m	902.2
Mooring line diameter	m	0.09

Clump mass	kg	17,253
Equivalent mooring line mass density	kg/m	42.5
Equivalent mooring line weight in water	N/m	381.8

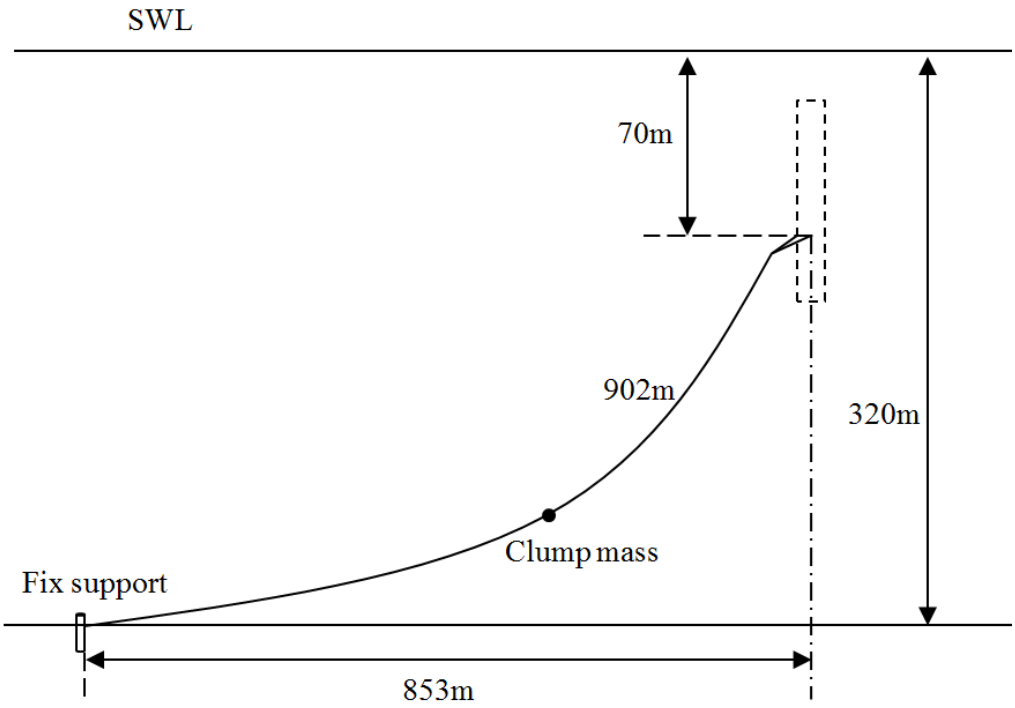

Figure 6-5 Mooring layout of the wind turbine [9]

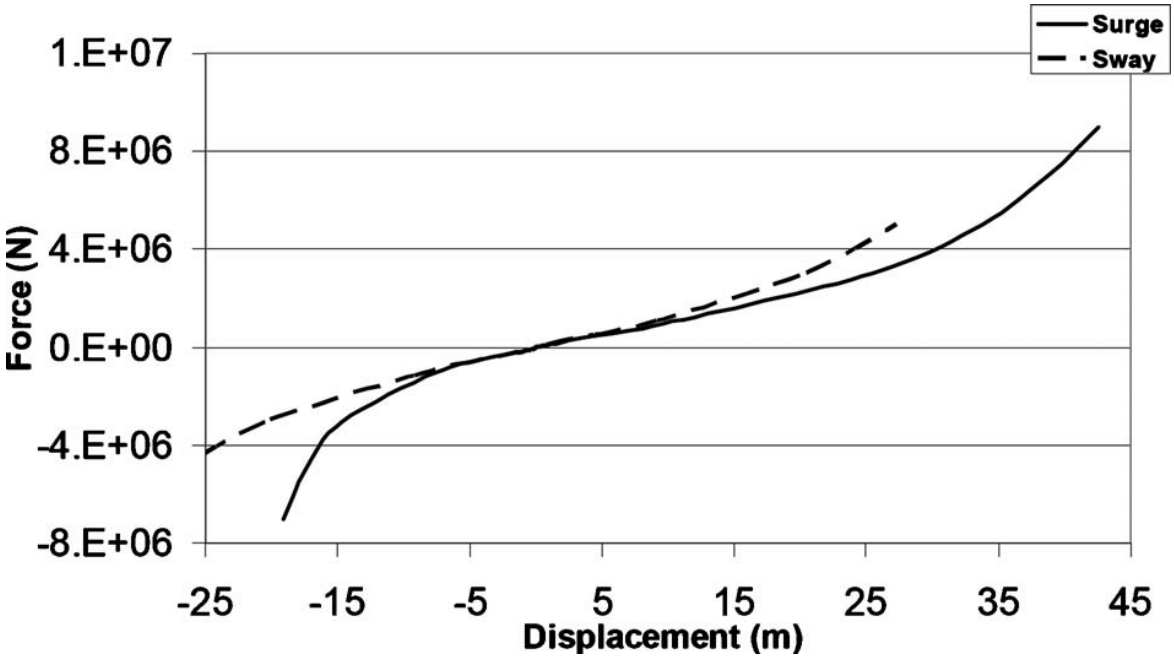

Figure 6-6 Force-displacement relationship of a mooring system [9]

6.3. Numerical simulations and discussions

6.3.1. Current-, wave- and wind- induced response

A comparison of the effects of different loads on the offshore wind turbine is made firstly. The nacelle and its components are considered as a point mass, the current, wave and wind are all assumed in the surge direction in this subsection. The nacelle's performance shows clearly the motion of the wind turbine, which includes both displacement and rotational response of the spar-support platform, and its standard deviation. The time history of the nacelle motion subjected to sea current only, current and wave coupled action, and a combination of the current, wave and wind actions, under three different sea conditions, defined in Table 3, are presented in Figure 6-7. Since the current excitation is independent of the sea condition, the nacelles' performance in all three sea conditions is found to be the same. The maximum displacement is 5.35m, the mean displacement is 2.67m and the standard deviation is 1.49m. A summary of the performance of the nacelle

in the surge direction under the three sea conditions with different considerations is shown in Table 5. It is found that the nacelle's mean displacement is increased no more than 1m when only the wave is involved but it can be increased up to 18.7m when both wave and wind are involved, meanwhile the change of its standard deviation is significant under wave-involved excitations, up to 16.32m, while the change is small when both wave and wind involved, only up to 2.5m. The maximum displacement is related to both the mean value and the standard deviation. The results show the nacelle's mean displacement response is primarily wind induced and its standard deviation is primarily wave induced.

The offshore floating wind turbine design standard mentioned by Jonkman [76] requires the consideration of the wind and wave misalignments up to 30 degree. The effect of the wind and wave excitation has been simulated and analysed individually in this study, the simulation results with misalignment consideration of $\pm 8^{\circ}$ and $\pm 30^{\circ}$ indicate the same conclusion as above. More detail can be found in Appendix 9.2.2.Thus the misalignment will not be further discussed in the following section.

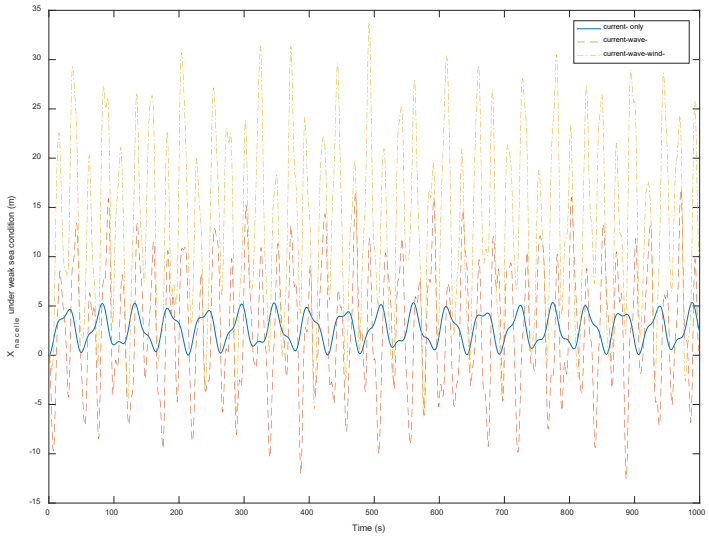

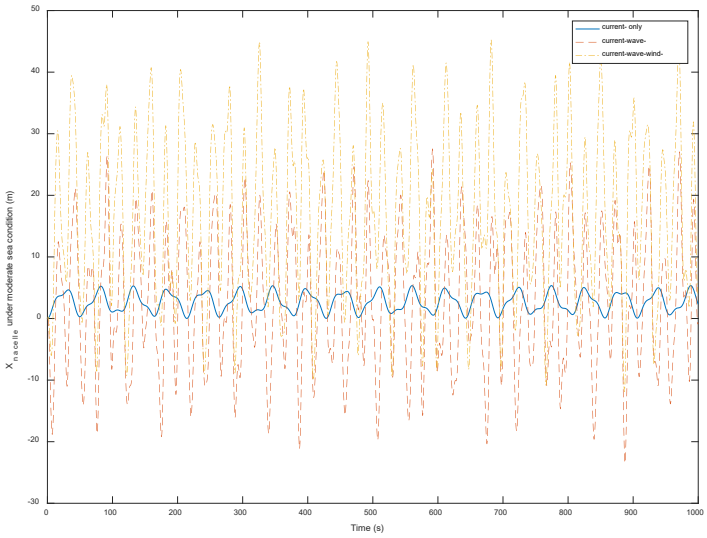

8

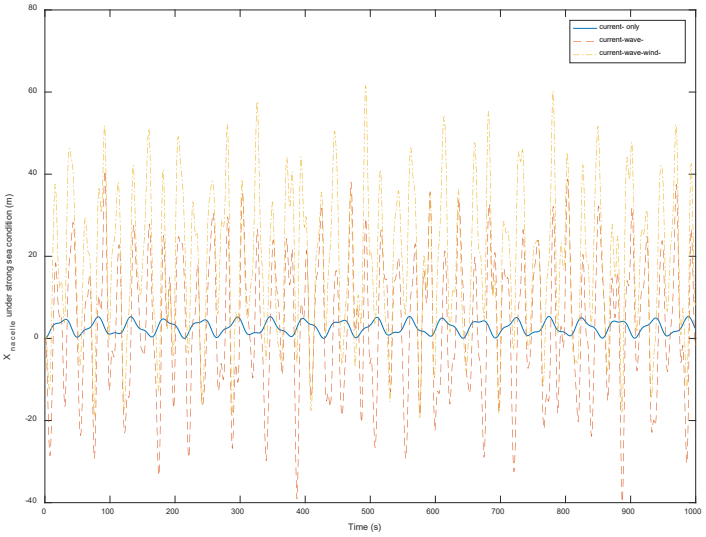

Figure 6-7 Time history of the nacelle's motion in the surge direction under (a) weak sea condition, (b) moderate sea condition, and (c) strong sea condition

Table 6-4 Nacelle performances in the surge direction

Excitations	Sea condition	Maximum displacement(m)	Mean displacement(m)	Standard deviation(m)
Current- only		5.35	2.67	1.49
Current-Wave-	Weak	16.83	2.66	6.22
	Moderate	27.4	2.89	10.94
	Strong	40.84	3.45	16.32
Current-Wave-wind-	Weak	33.69	13.25	8.93
	Moderate	45.19	16.7	13.2
	Strong	61.66	18.72	17.55

6.3.2. Effect of the dynamic interaction on the performance of the platform and the drive-train system

In order to investigate the effect of the dynamic interaction between the drive-train system and the platform with tower, the wind turbine model is simulated by considering the drive-train system as a point mass firstly and the drive-train itself has also been simulated in a fixed-stator condition to show their own performances without the interaction, and then the interaction from the rotating drive-train system is considered. In this subsection, the wind, wave and current are assumed in the same direction. For the drive-train system under a fixed-stator condition, the stator and the bearings are fixed and constrained in all

directions. The performance of the CG's motion and the rotor's motion can be found directly from Eq.(6.1), while under the interaction condition, such performances should also take the motion of the nacelle into account. The displacement responses of the CG of the drive-train system and the rotor in the local coordinate system are compared to examine their dynamic performances, as shown in Figure 6-8. Under the fixed-stator condition, the maximum displacement of the CG is 9.72×10^{-6}m at 8.3rpm and 2.03×10^{-5}m at 12rpm, maximum displacement of rotor is 1.84×10^{-5}m at 8.3rpm and 3.83×10^{-5}m at 12rpm. Under the interaction condition, the maximum displacement of the CG under the local coordinate system is 9.92×10^{-6}m at 8.3rpm and 2.06×10^{-5}m at 12rpm, the maximum eccentricity of rotor and stator is 1.82×10^{-5}m at 8.3rpm and 3.76×10^{-5}m at 12rpm. A percentage difference of the performance can be expressed to study the effect of the interaction on the dynamic response by using the formula:

$$\text{difference}\% = \frac{\mathrm{R_{int}} - \mathrm{R_{pm}}}{\mathrm{R_{pm}}} \times 100\% \qquad (6.26)$$

where R_i is the response of the model corresponding to its consideration, the subscript *int* represents the model with interaction and *pm* denotes the model without the interaction. The differences under two conditions are only about 2% in their performance. This means the effect of the interaction on the dynamics of the drive-train system itself is small and can be ignored in some cases.

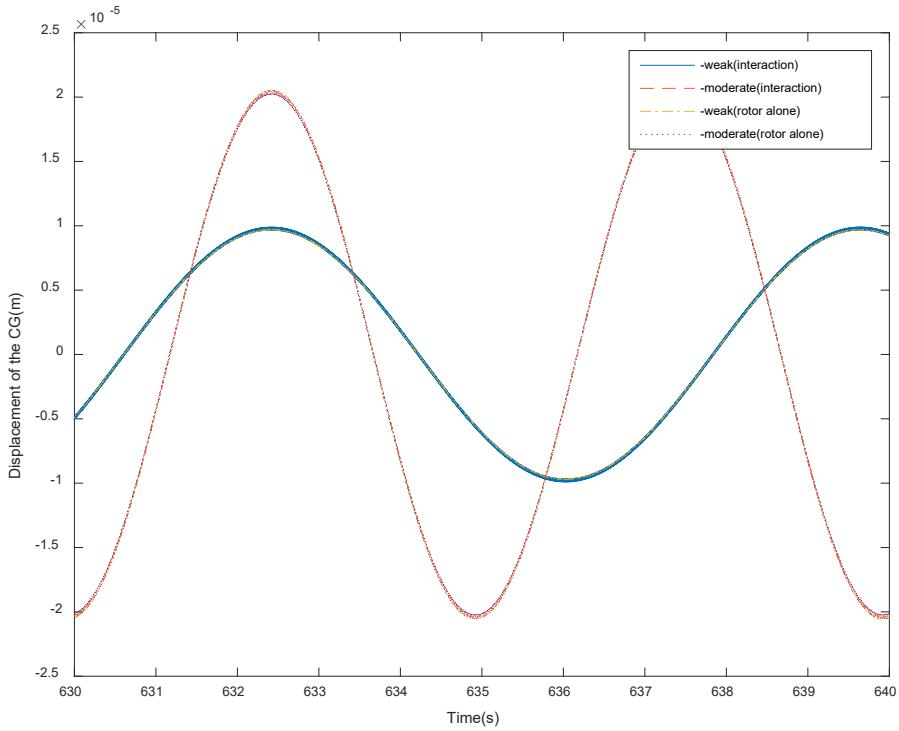

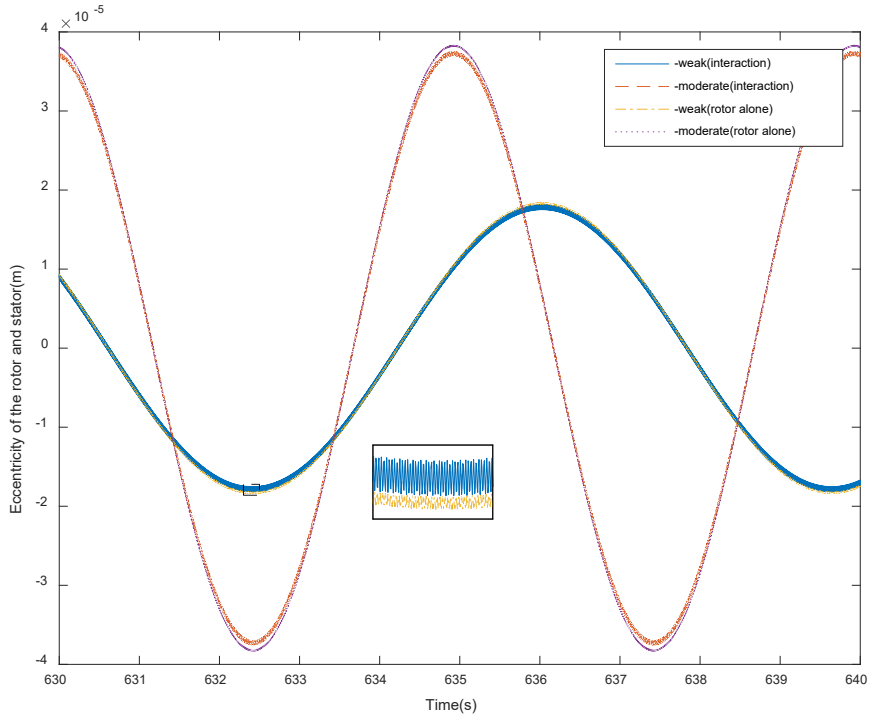

Figure 6-8 Displacement response of the CG of the drive-train system and the rotor under fixed-stator and interaction conditions

Figure 6-9 shows the motion of the nacelle in surge and sway directions under two considerations under different sea conditions. The effect of the dynamic interaction on the spar-support platform is noticeable, however it is not significant. In Figure 6-10, the differences in the frequency response for the nacelle's motion in the surge and sway directions are shown in the FFT spectrum figures. Additional peak frequency response can be found in both surge and way directions due to the dynamic interaction and such frequency responses are correlated to the rotating speed of the drive-train system. Figure 6-11 shows the performances of the nacelle's motion between the cut-in and cut-out wind speeds. The mean value of the nacelle's motion in the surge direction shows less than 1% difference. The maximum and standard deviation of the nacelle's motion in the surge direction is only up to 2.5% difference when considering the interaction. However, the maximum value and the standard deviation in the sway direction has increased significantly when the interaction is considered and the mean value of the motion in the sway direction remains within a small range. The reason for the large differences in the sway direction is that all excitations are assumed in the surge direction. The vibration in the sway direction is damped nearly to steady-state when the interaction is not induced. While the dynamic interaction would generate additional excitation in the sway direction (perpendicular to the wind direction) which means that the effect of the interaction on the platform's motion is induced in the sway direction. As a result, the effect of the dynamic interaction is evident but not significant when the wave, wind and current are all in the same direction. However, these results will be changed when the wave and wind directions are changed, which will be discussed in the following section.

A notable increase can be found at the nacelle's motion in the sway direction when the wind speed is increased from 8 to 16 m/s. This change is attributable to the rotating speed of the drive-train system that corresponds to the wind speed. It is also noted that the

increase of the nacelle's performance under strong sea condition due to the dynamic interaction, when the drive-train system stops rotating, still exists but the effect is reduced. This is because the eccentricity in the drive-train system is not only caused by self-rotating motion but also caused by its global translational motion.

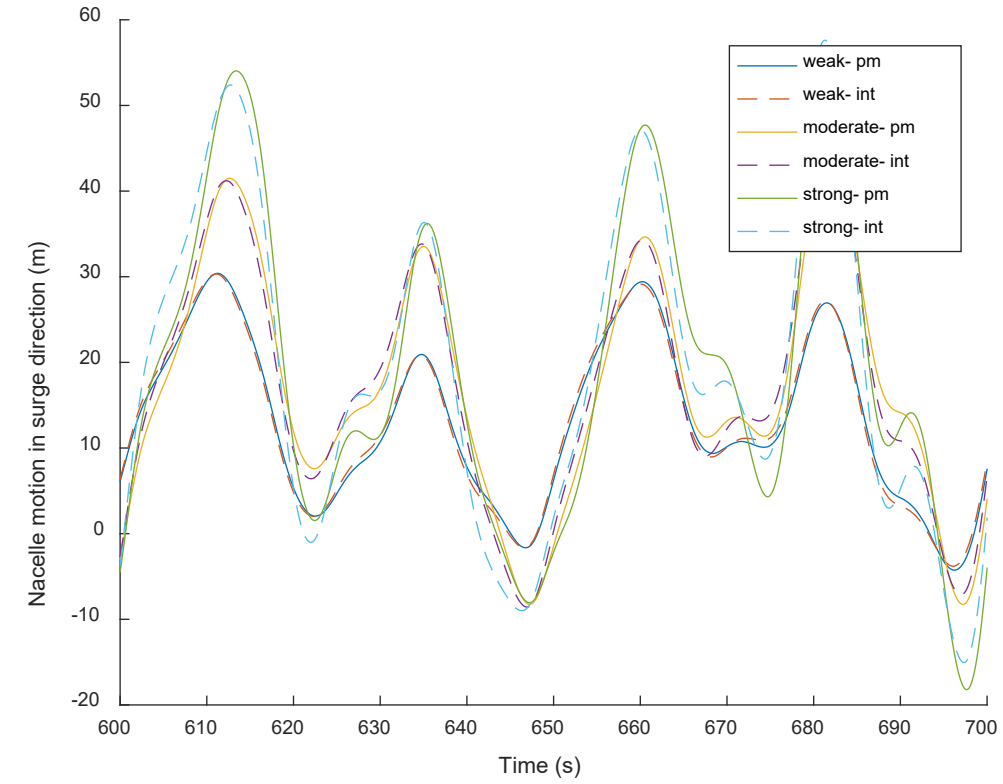

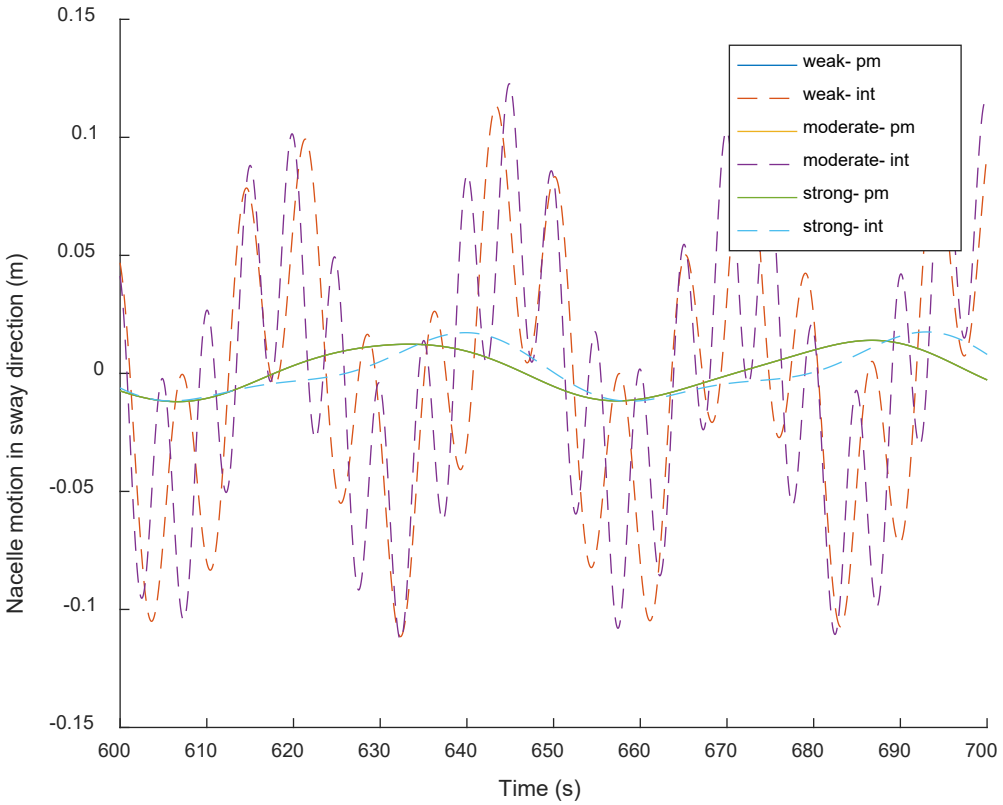

Figure 6-9 Time history of the platform motion in surge and sway directions

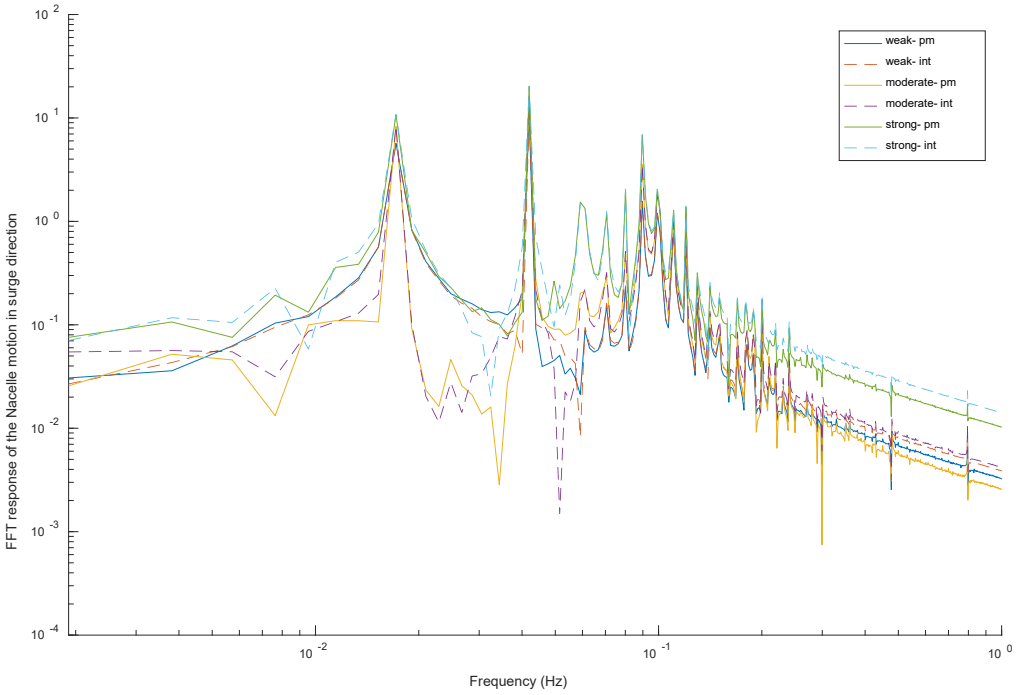

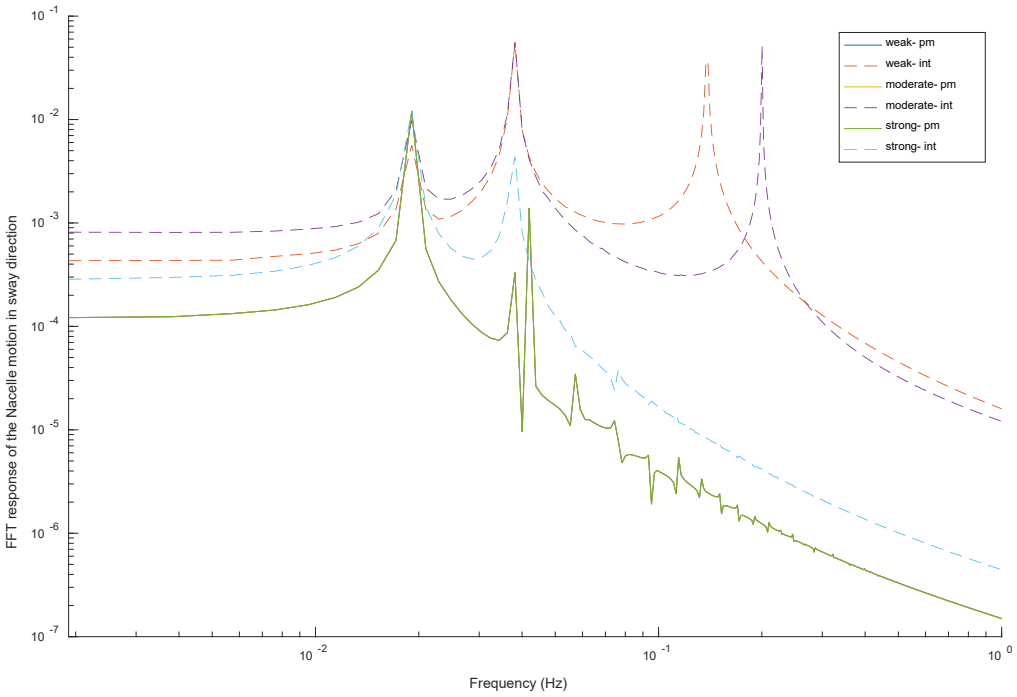

Figure 6-10 FFT of the nacelle's motion in the surge and sway directions

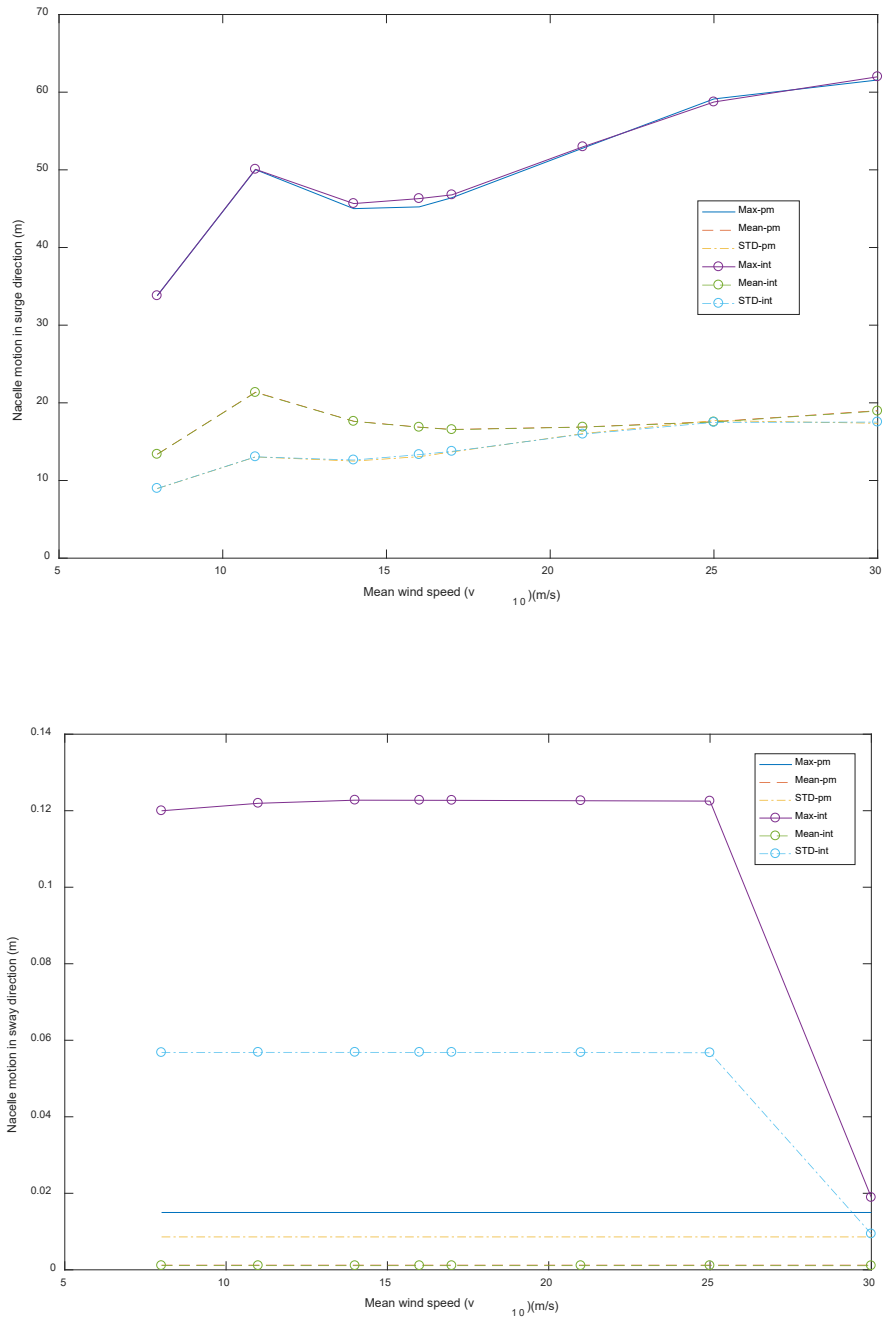

Figure 6-11 Performances of the platform motion in surge and sway directions

6.3.3. Effects of wind and current angle on the motion of the spar-support platform

In order to form a complete 3D description of the deep-sea environment, the directions of the wind and wave spreading referenced to the sea current direction should also be considered. Significant changes are expected to happen when the wind direction moves from the sea current direction to its opposite direction, while 180 degree could cover all possible cases and the performance in the other directions would show a mirrored trend about the surge axis. The performance of the nacelle's motion in surge and sway directions when the wind and current direction turns from 0 degree to 180 degree under different sea conditions are compared and shown in Figure 6-12. Firstly, it can be found from the results that the maximum displacement of the nacelle in the surge direction is reduced from 62 to 0m when the wind direction turns from the surge direction to its opposite direction meanwhile the mean displacement is reduced from 19 to -13m. The maximum displacement of the nacelle in the sway direction is in the range of 0 to 58.5m. The maximum orbital motion of the nacelle can be found in the range of 62 to -49m in the surge direction and -58.5 to 58.5m in the sway direction for all wind conditions from a fully simulation results. This is caused by the current excitation with a fixed direction and the different resultant stiffnesses of the mooring system corresponding to the wind turbine's displacement. The differences of the performance of the model are also notable when the interaction is considered or not. The percentage differences of the mean and standard deviation values of the nacelle's motion in two considerations are shown in Figure 6-13. For the nacelle's motion in the surge direction, a -20% peak percentage change can be found at 105 degree for the mean value, which means a significant decrease of the mean value happening at $\boldsymbol{\theta_{wc} = 105\ deg}$ when considering the interaction. A ±20% peak percentage change at 75 degree and 105 degree for the standard deviation

shows that the effect of the dynamic interaction would increase the vibration of the wind turbine in the surge direction when the wind direction is closer to sway direction. For the nacelle's motion in the sway direction, the percentage differences of the mean value and the standard deviation are within 10% for all three sea conditions. The percentage differences of the maximum values in both surge and sway directions are non-linear because the maximum value of the nacelle's motion is mainly depending on the irregular wave excitation. By comparing the effects of the dynamic interaction under different sea conditions in both wind directions, it can be found that the absolute percentage difference of the mean value under the higher wind speed sea condition is always higher than under low wind speed sea condition. On the contrary, the percentage difference of its standard deviation is lower, which means the effect of the interaction would be enhanced at the mean value but reduced at the standard deviation when sea condition is stronger (i.e., wind speed is higher).

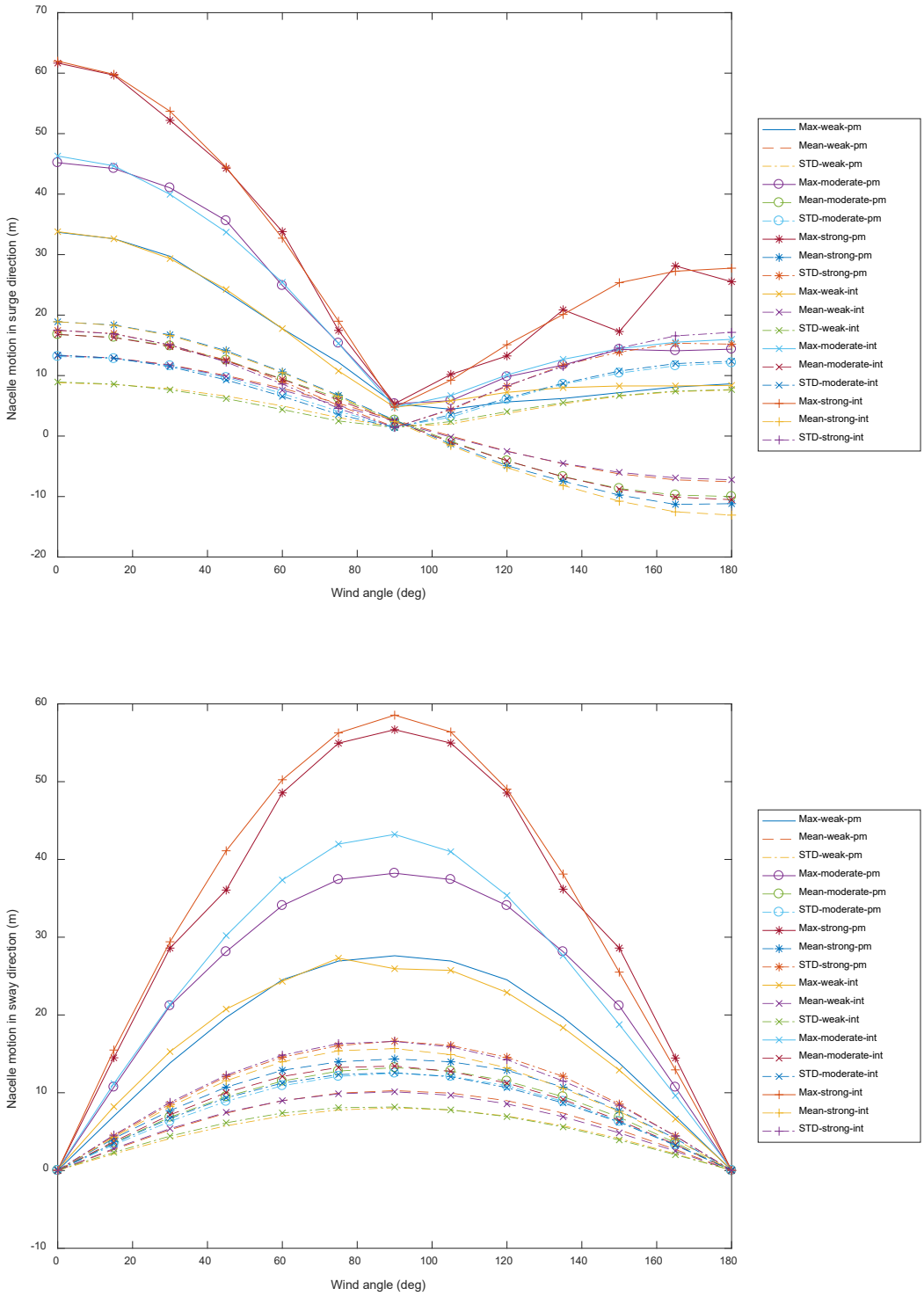

Figure 6-12 Performance of the nacelle's motion in surge and sway directions when changing the wind and current directions

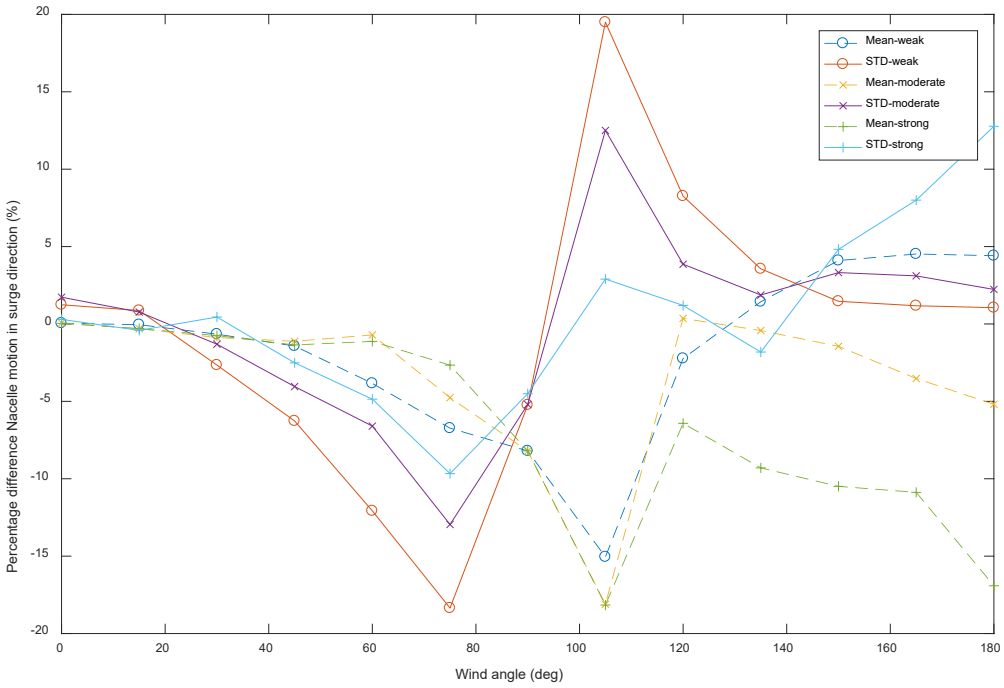

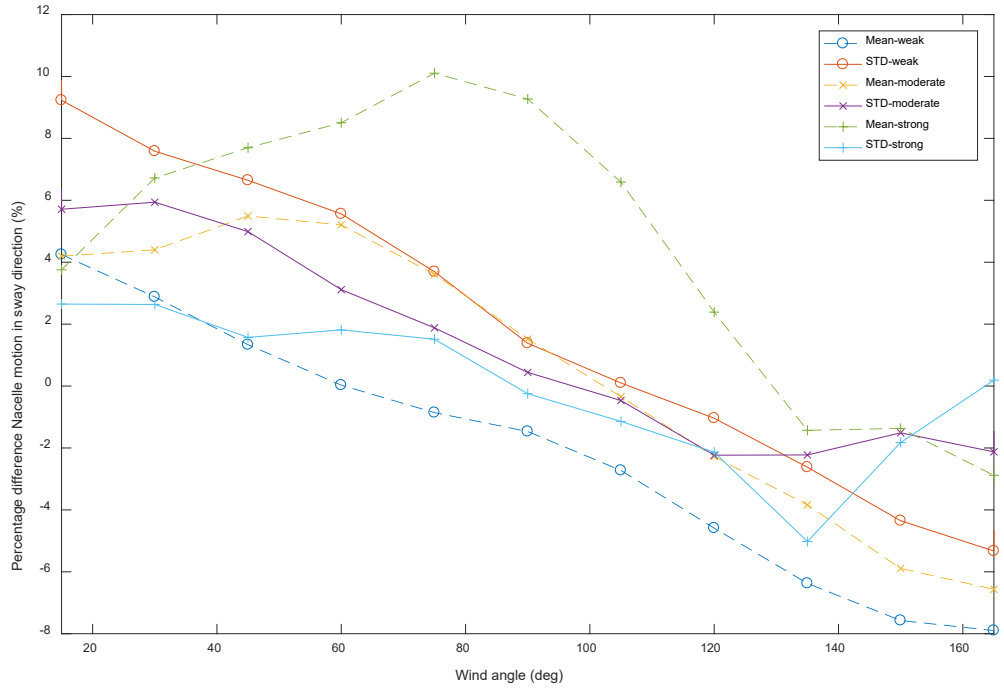

Figure 6-13 Percentage difference of the mean and standard deviation when changing the wind and current direction

6.4. Conclusion

This chapter studied the dynamic response of a spar-type floating direct-drive wind turbine caused by both hydrodynamic and aerodynamic excitations. The hydrodynamic and aerodynamics excitations are generated from wind, wave, current and buoyancy. The comparison of the effects of the current, wave and wind excitations shows that the nacelle's mean displacement response is primarily wind induced and its standard deviation is primarily wave induced.

The dynamic interaction between the drive-train system and the platform with tower structure has been discussed. It was found that the interaction in the drive-train system is not only caused by self-rotating motion of the drive-train system but also caused by the global translational motion. However, the comparison of performance indicated that the effect of interaction between the drive-train system and the nacelle on the dynamic response of the drive-train system itself can be ignored with a percentage difference being less than 3%, whereas the effect on the spar support with tower structure is notable but not significant and can induce the nacelle motion's response in both surge and sway directions when the wave and wind are in the surge direction.

The directions of the wind and wave spreading correlated to the sea current direction were also considered to form a complete 3D description of the deep-sea environment. The maximum orbital motion of the nacelle for different wind directions was found to be from -49 to 60m in the surge direction and -58.5 to 58.5m in the sway direction. By considering the interaction, the mean value and the standard deviation of the nacelle motion could lead to a 20% change in the surge direction and a 10% change in the sway direction. The effect of the interaction was found to be enhanced at the mean value but would be reduced at the standard deviation when the sea condition is stronger (wind speed is higher).

7. Tower vibration of the spar type wind turbines

In this Chapter, the free-vibration analysis for the tower structure of a spar-type floating offshore wind turbine is carried out by modelling it as a flexible beam structure between the floating platform and nacelle. The effects of the tower parameters, joint connections between the tower and other components, as well as the other related parameters on the natural frequencies are discussed. The theoretical analysis of the free vibration of both uniform tower structure and non-uniform tower structure is included.

7.1. Determination of the natural frequencies and mode shape for a uniform tower structure

An Euler-Bernoulli beam will be used to model the tower structure for the spar-type offshore wind turbine. Unlike the models considered in several published papers [119, 172, 173], the new tower model considered in this chapter uses a free-free beam with two large mass components attached at its ends which are employed to represent the nacelle and floating platform, as shown in Figure 7-1. Torsion spring constraints imposed at both ends of the beam (tower) are used to describe the joint connections between the tower and floating platform or nacelle. The stiffnesses of two springs are different due to different connecting methods between different structures. A uniform tower structure will be considered in this section.

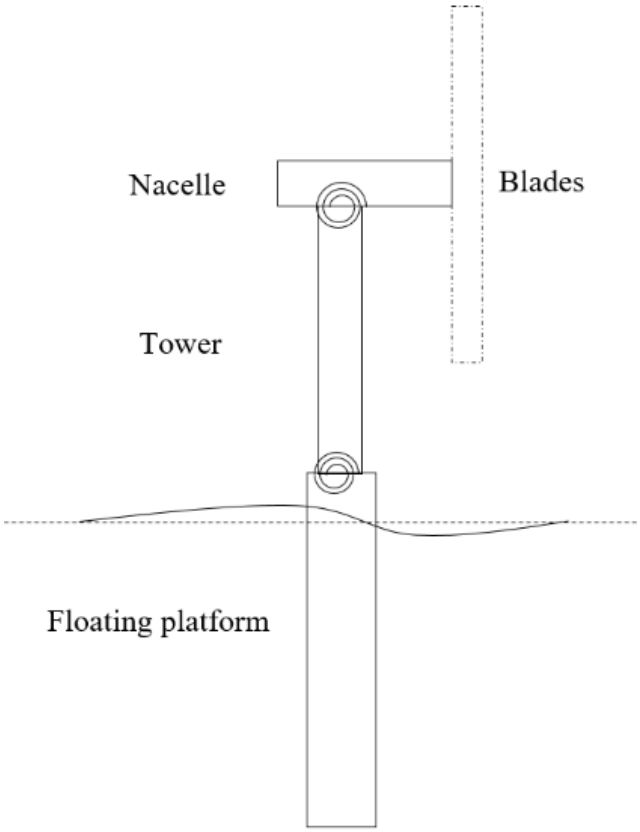

Figure 7-1 Schematic of a free-free model of the offshore wind turbine

The equation of motion of the tower structure can be derived according to Geradin and Rixen [174] and Adhikari [119] as

$$EI_{(z)}\frac{\partial^4 w_{(z,t)}}{\partial z^4} + N_{(z)}\frac{\partial^2 w_{(z,t)}}{\partial z^2} - m_{(z)}r_{(z)}{}^2\frac{\partial^2}{\partial z^2}\left(\frac{\partial^2 w_{(z,t)}}{\partial t^2}\right) + m_{(z)}\frac{\partial^2 w_{(z,t)}}{\partial t^2} = f_{(z,t)} \quad (7.1)$$

where z is the altitude along the tower, $EI_{(z)}$ is the bending stiffness of the tower, $N_{(z)}$ is the normal force in the vertical direction, $m_{(z)}$ is the mass density per unit length of the tower, $r_{(z)}$ is the radius of gyration and $f_{(z,t)}$ represents the resultant force of various loadings applied on the tower, which can be simply expressed as a harmonic excitation with a constant amplitude f_0 and an angular frequency ω_e, $f_{(z,t)} = f_0 e^{i\omega_e t}$.

By using the separation of variables method, the general solution to the free-vibration of equation (7.1) for the nth vibrational mode can be written as

$$w_{(z)} = A_1 \sin(\lambda z) + A_2 \cos(\lambda z) + B_1 \sinh(\lambda z) + B_2 \cosh(\lambda z) \qquad (7.2)$$

where $\lambda^2 = \omega_n \sqrt{\frac{m}{EI}}$, and ω_n is the nth natural frequency. The boundary conditions at the two ends of the tower structure are used to determine the unknown constants. More detail can be found in Appendix 9.3.1.

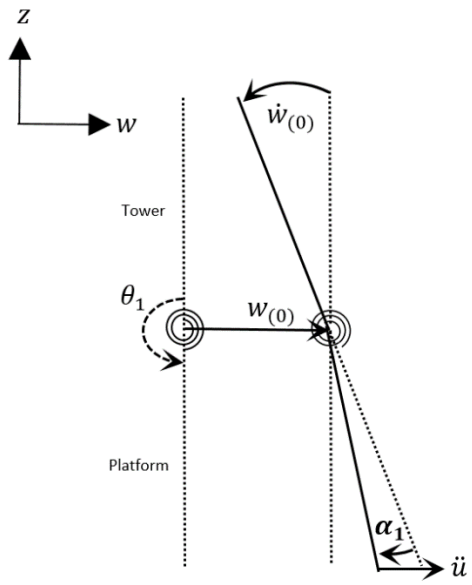

Figure 7-2 Geometry of boundary condition at z=0

Figure 7-2 shows the geometry of boundary condition at z=0, where $w_{(0)}$ is the displacement in the horizontal direction and $\dot{w}_{(0)}$ is the slope of the tower bottom end. θ_1 is the fixed angle between the longitudinal axes of the platform and undeformed tower. The moment equilibrium at this location with the torsion spring, k_1, can lead to a rotating angle α_1, as $\alpha_1 = \frac{EIw''_{(0)}}{k_1}$. The acceleration of the platform in the horizontal direction can be written as $\ddot{u} = -\omega^2 w_{(0)}$, which is obtained by differentiating the general equation twice and also as given in [175]. The equation of equilibrium for the bending moment at z=0 can be expressed as

$$EIw''_{(0)} = -I_{01}\omega^2\left(w'_{(0)} - \alpha_1\right) - g_1\, M_1\omega^2 w_{(0)}\cos(\theta_1) \qquad (7.3)$$

where I_{01} is the moment of inertia of the platform about the connection point (i.e., the bottom end of the tower) and M_1 is the mass of the platform. $I_{01}\omega^2\left(w'_{(0)} - \alpha_1\right)$ denotes the moment due to the rotational inertia of the mass, and $g_1\, M_1\omega^2 w_{(0)}\cos(\theta_1)$ represents the moment due to the acceleration. The shear force equilibrium at z=0 can be expressed as

$$EIw'''_{(0)} = M_1\omega^2 w_{(0)} + g_1\, M_1\omega^2(\dot{w}_{(0)} - \alpha_1)\, cos(\theta_1) \qquad (7.4)$$

Similarly at the top end of the tower with z=L, the tower is connected to the nacelle with another torsion spring, k_2, the equations of equilibrium for bending moment and shear force can be written as

$$EIw''_{(L)} = I_{02}\omega^2\left(w'_{(L)} + \alpha_2\right) + g_2\, M_2\omega^2 w_{(L)}\, cos(\theta_2) \qquad (7.5)$$

$$EIw'''_{(L)} = -M_2\omega^2 w_{(L)} - g_2\, M_2\omega^2(\dot{w}_{(L)} + \alpha_2)\, cos(\theta_2) \qquad (7.6)$$

where I_{02} is the moment of inertia of the nacelle about the connection point (i.e., the top end of the tower) and M_2 is the mass of the nacelle. θ_2 is the fixed angle between the longitudinal axes of the nacelle and undeformed tower. α_2 is the rotating angle of the nacelle due to the moment equilibrium at this location with the torsion spring, k_2, and it is given by $\alpha_2 = \frac{EIw''_{(L)}}{k_2}$.

Substituting the general solution given by Eq.(7.2) into the four equations of boundary condition, Eqs.(7.3)-(7.6), yields

$$\begin{bmatrix} R_{11} & R_{12} & R_{13} & R_{14} \\ R_{21} & R_{22} & R_{23} & R_{24} \\ R_{31} & R_{32} & R_{33} & R_{34} \\ R_{41} & R_{42} & R_{43} & R_{44} \end{bmatrix} \begin{bmatrix} A_1 \\ A_2 \\ B_1 \\ B_2 \end{bmatrix} = 0 \qquad (7.7)$$

where the elements of the matrix R are listed in Appendix 9.3.2 for brevity.

Since the constant vector $[A_1\ A_2\ B_1\ B_2]^T$ is generally non-zero, the matrix R should have a zero solution as

$$\det[R_{ij}] = 0 \qquad (7.8)$$

The transcendental equation can be solved using symbolic calculation method in MATLAB to obtain numerical results. Numerical simulations will be conducted to obtain the natural frequencies and the corresponding mode shapes.

The main components and their system parameters studied in this section, such as the platform, tower and nacelle, are adopted from the NREL designed 5MW direct-drive wind turbine [9, 19, 144, 161]. The nacelle and platform are considered as large mass components connecting at two ends of the tower structure. The related parameters are shown in Table 7-1 and 7-2. The main parameters of the turbine structure are given in Table 5-1, respectively. Other relevant constants are calculated using the formulas given in Appendix 9.3.3.

Table 7-1 Parameters of the tower structure [9, 19, 144, 161]

Description	Symbol	Units	Value
Elastic modulus	E	Pa	2.1×10^{11}
Area moment of inertia	I	m^4	To be calculated
Material density	ρ	kg/ m^3	7800
Tower length	L	m	77.6

Tower average diameter	D	m	5
Tower top diameter	D_{top}	m	3.2
Tower bottom diameter	D_{bottom}	m	6.5
Average shell thickness	t	m	0.03
Top shell thickness	t_{top}	m	0.027
Bottom shell thickness	t_{bottom}	m	0.043

Table 7-2 Parameters of the platform and nacelle [9, 88, 144, 161, 167-169]

Description	Symbol	Units	Value
Total mass of the platform	M_1	kg	7,593,000
Moment of inertia of the platform about its centre gravity (CG)	I_1	$kg \cdot m^2$	4.489×10^9
Distance between the CG of the platform to the bottom end of the tower structure	g_1	m	102.6
the fixed angle between the longitudinal axes of the platform and the undeformed tower	θ_1	degree	180
Total mass of the nacelle	M_2	kg	240,000
Moment of inertia of the nacelle about its CG	I_2	$kg \cdot m^2$	2.1×10^6

Distance between the CG of the nacelle to the top end of the tower structure	g_2	m	To be calculated
Horizontal distance between the CG of the nacelle and the top end of the tower structure	$l_{oo'}$	m	0.65
Vertical distance between the CG of the nacelle and the top end of the tower structure	$h_{oo'}$	m	1.5
the fixed angle between the rotating axis in the nacelle and the undeformed tower	θ_2'	degree	90

The stiffnesses of the torsion springs k_1 and k_2 are different due to the different joint methods between the tower and two mass components. Normally the bottom end of the tower is fixed with the platform, and the equivalent stiffness k_1 could be infinity as of a fixed support. The top end of the tower is connected with the nacelle through the yaw system with bearings, the stiffness k_2 could be significantly large but smaller than k_1. Therefore, the parameters of the joint types, or say the stiffnesses of the torsion springs, will be considered variable to understand how they will affect the overall vibration of the tower structure, which will be discussed later in this section. For the initial analysis, both the torsion springs are assumed to have the same stiffness of $10^{15} Nm/rad$. The natural frequency ω_n can be numerically solved from Eq.(7.8), then the elements of matrix $\boldsymbol{R}$ can be found. By letting A_1 =1 in the constant matrix $[A_1\ A_2\ B_1\ B_2]^T$ and using Eq.(7.7), the unknown constants, A_2, B_1 and B_2 can be numerically determined. Then by substituting all the known parameters, ω_n, A_1, A_2, B_1, B_2, into Eq.(7.2), the nth mode shape $w_{n(z)}$ can be obtained.

The first three natural frequencies under the given parameters are found to be 2.308, 23.087 and 69.101 rad/s, respectively. The third natural frequency is far beyond the frequency range of interest for offshore wind turbines [176]. Thus only the first two natural frequencies will be considered in the discussion of mode shapes. The mode shapes corresponding to ω_1 and ω_2 are shown in Figure 7-3. The first natural frequency of the tower structure and both mode shapes show a good agreement with the FEA simulation results as discussed by Si *et al.* [122] and Yilmaz [177]. For the first mode shape, it also shows a close agreement with Karimirad and Moan's [87] tower elastic mode as shown in their figure 9, which has a frequency at 2.37 rad/s. Table 8 presents the comparison of the first natural frequency obtained using different models. For the second mode shape, a dash-dot line connecting the top and bottom ends of the tower indicates a rigid-body rotation of the tower. The two large mass components demonstrate opposite direction rotation to achieve the force and moment equilibrium. Nodal point *N*, the intersection of the dashed line and the second mode shape line, is close to the bottom end of the tower because the mass of the platform is far larger than that of the nacelle. When the mass difference of the two components changes, the location of the nodal point will move along the tower axis.

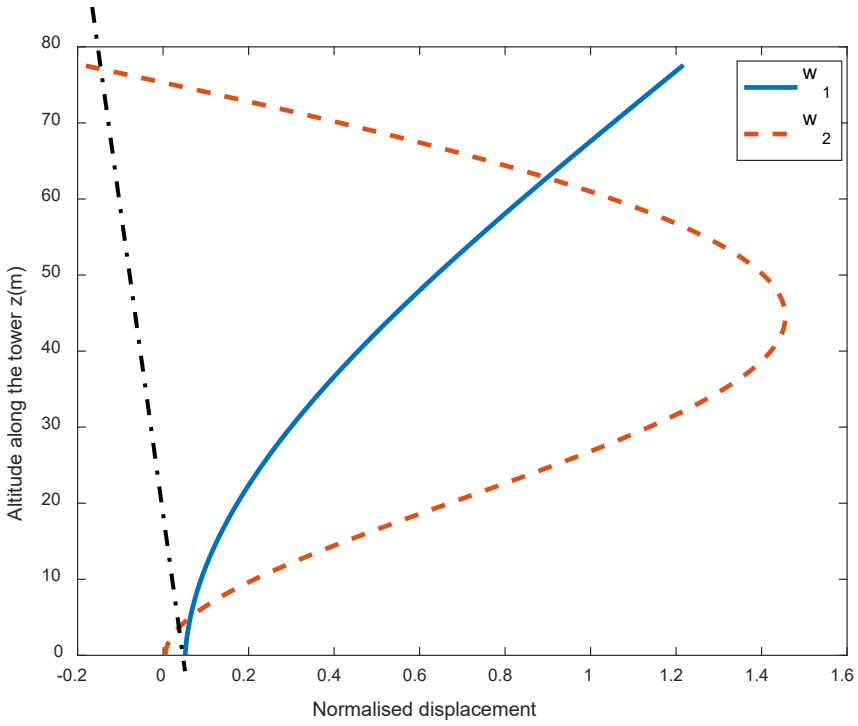

Figure 7-3 First and second mode shapes of the tower structure

Table 7-3 Comparison of the first natural frequency from different models

	NREL 5 MW offshore wind turbine				
Model Type	Tower-monopile[177]	Platform-tower[122]	Spar-tower-blade[87]		Spar-tower-nacelle
Modelling Method	FAST-SC	FAST-SC	HAWC2	ABAQUS	MATLAB
Natural Frequency (rad/s)	1.25 -2.14	2.953	2.89	$2.78_{(shell)}$ $2.89_{(beam)}$ $2.37_{(tower\ part)}$	2.308rad/s

7.1.1. Effects of the tower parameters

The uniform thickness shells are widely used in the theoretical analysis of offshore wind turbine tower to simplify a non-uniform tower for brevity. It should be noted that the non-structure mass (such as cables for power transmission and stairs for access to the nacelle) can contribute to the mass of the tower structure. The parameters of diameter D, thickness t, and mass density ρ will be used as the variables to understand their effects on the natural frequencies of the system.

Given the fact that the non-structure mass does not affect the mode shape of the tower directly but can increase the mass density per unit length [75], the mass density ρ will be assumed higher than the structure materials to account for the non-structure mass. Figure 7-4 shows the variation of the first natural frequency of the tower structure with respect to different mass density ρ. The natural frequency of the whole system decreases linearly with the increase of mass density ρ. The decreasing rate is only about 1% when ρ is increased from $7800kg/m^3$ to $8700kg/m^3$ by an 11.5% (or say by adding $422\ kg/m$ of the mass per unit height).

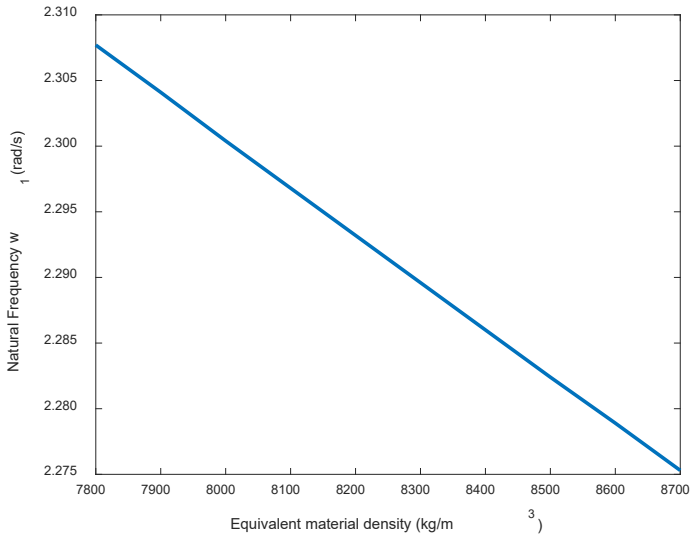

Figure 7-4 Variation of the first natural frequency of the tower structure with respect to the mass density

Different from the mass density, the variation of the tower diameter and shell thickness can not only change its mass density per unit length, but also its moment of inertia of the circular cross section. The first natural frequency of the tower structure under different diameter *D* and thickness *t* is shown in Figure 7-5 and 7-6, respectively.

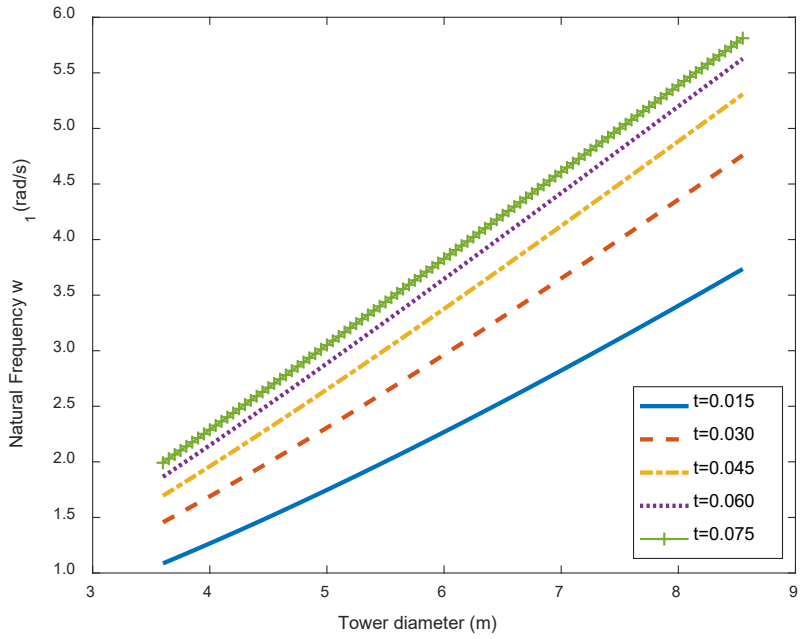

Figure 7-5 Variation of the first natural frequency of the tower structure with the tower diameter D under different shell thickness

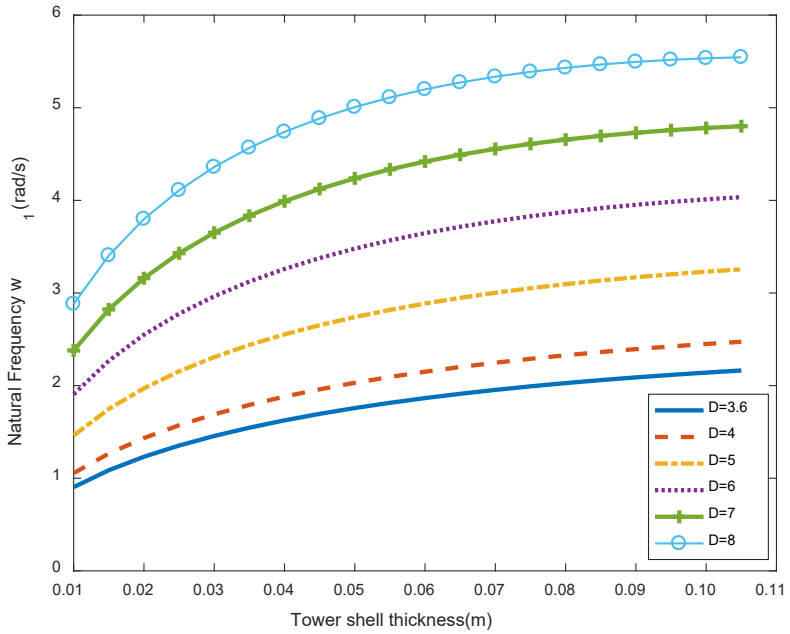

Figure 7-6 Variation of the first natural frequency of the tower structure with the tower shell thickness under different diameters

Firstly, it is easy to notice that an increase of either *D* or *t* would lead to a non-linear increase of the first natural frequency of the whole system. From Figure 7-5, the natural frequency is increased with an increase of the tower diameter under different thickness. A larger shell thickness gives a higher natural frequency under the same tower diameter. The increase rate of natural frequency is reduced quickly when the thickness *t* is increased, as shown in Figure 7-6. The percentage increase of the natural frequency due to the increase of the thickness from 0.01m to 0.1m are 140% (from 0.90Hz to 2.16Hz) when *D=3.6m*, and 92.4% (from 2.88Hz to 5.54Hz) when *D=8m*. The percentage increase of the natural frequency due to the increase of the tower diameter *D* from 3.60m to 8.55m are 244% (from 1.087Hz to 3.74Hz) when t=0.015*m*, and 192% (from 1.99Hz to 5.81Hz) when *t=0.075m*. This means that within the reasonable and possible variation range of the shell thickness and tower diameter, the effect of the variation of the thickness

and diameter on the natural frequency of the whole system at a small diameter or thickness is larger than at large diameter or thickness. As mentioned in [119, 178-181], the possible frequency range of the excitations from a fully-developed sea condition is from 0.04Hz to 0.1 Hz (i.e., from 0.25 to 0.62rad/s), and from a non-fully-developed sea condition is from 0.5Hz to 0.7Hz (from 3.1 to 4.3rad/s) based on the JONSWAP wave model. For a 3MW Opti-OWECS turbine, the rotor frequency is 0.37Hz (or 2.3rad/s) and the blade passing frequency is 0.75Hz (or 4.6rad/s), while for the 5MW NREL direct-drive wind turbine, the rotor frequency of the drive-train system is 0.267Hz (or 1.68rad/s). The design of the turbine structure should ensure the resultant natural frequency to be outside the range of the environmental excitation frequencies and the frequencies of the other structural components to avoid resonant vibrations, large bending moment and shear force for a long-term safe operation. A 3D plot of the variation of the first natural frequency of the whole system with respect to both the tower diameter and shell thickness is shown in Figure 7-7. From this figure, the tower parameters (the shell thickness and the tower diameter) can be chosen to avoid the resonance for a safe operation.

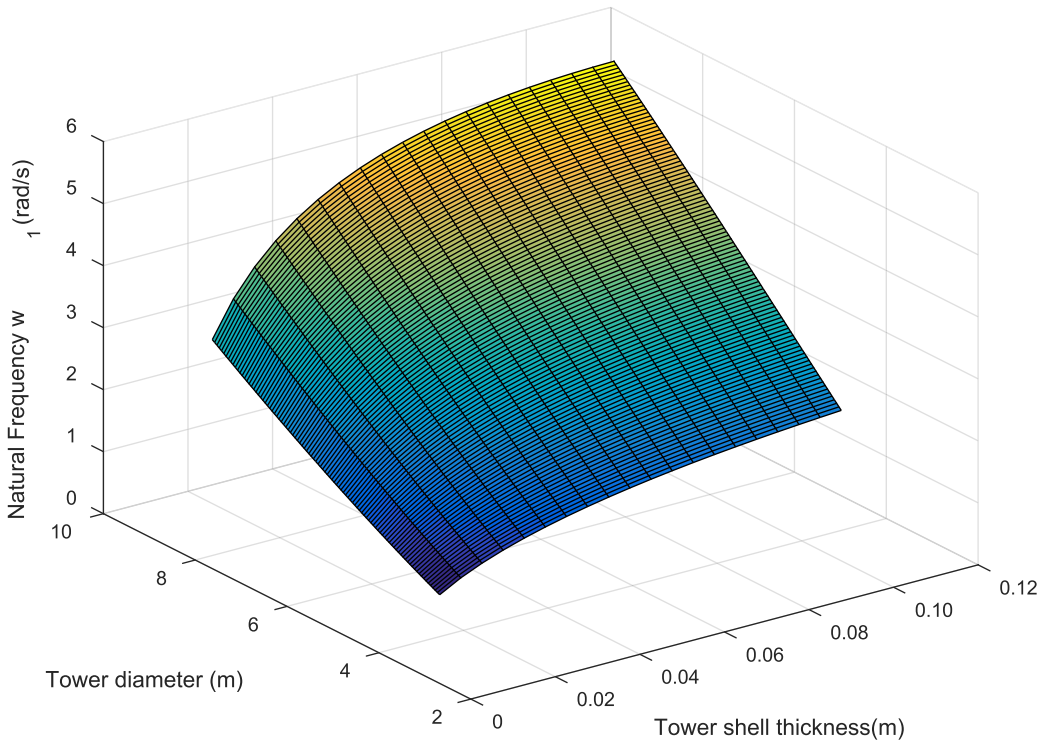

Figure 7-7 Variation of the first natural frequency of the tower structure with the tower diameter and thickness in 3D plot

7.1.2. Effects of the joint stiffness of the tower with end components

The tower structure is connected by the nacelle at its top end and the spar-type platform at its bottom end through different joint methods. The joints of the tower structure with these two end components are modelled as torsional springs, and the spring stiffness is considered in the range from 10^{-5} to $10^{15}\ Nm/rad$. It should be mentioned that the stiffness k will never be equal to zero due to the moment equilibrium equation of the torsional spring. Here $k_i = 10^{-5}\ Nm/rad$ means that the connection type is a pure revolute joint, and $k_i = 10^{15}\ Nm/rad$ indicates that the connection type is a fixed joint. For the bearing type joint at the top end of tower, k_2 should be smaller than $10^{15}\ Nm/rad$. The high value of the torsional stiffness can stabilize the system. The

consideration of low values of spring stiffness assumes that there may exist cracks at the connecting location. The overall variation of the first natural frequency of the tower structure with respect to both k_1 and k_2 is shown in Figure 7-8. The zero natural frequency results shown in Figures 7-8 to 7-12 suggest that the whole system be buckled [119]. The stiffness at these ranges will not be considered as this situation is not under a safe operational condition. It is interesting to observe from Figures 7-8 to 7-12 that the performances of the torsional springs at different locations are different. From the meaningful (non-zero) values of the natural frequencies shown in Figure 7-9, it can be found that the natural frequency of the whole system has no significant changes when the stiffness of the torsional spring is higher than a certain value (about$10^{11}\ Nm/rad$). This indicates that the joint has already been essentially considered as a fixed joint. Meanwhile, the natural frequency of the system is highly sensitive when either k_1 or k_2 is in the range from 10^5 to $10^{10}\ Nm/rad$. This means a slightly lower value of the torsional stiffness than the stiffness of the fixed state, normally corresponding to a weak connecting type or cracks at the joints, would destabilize the whole system.

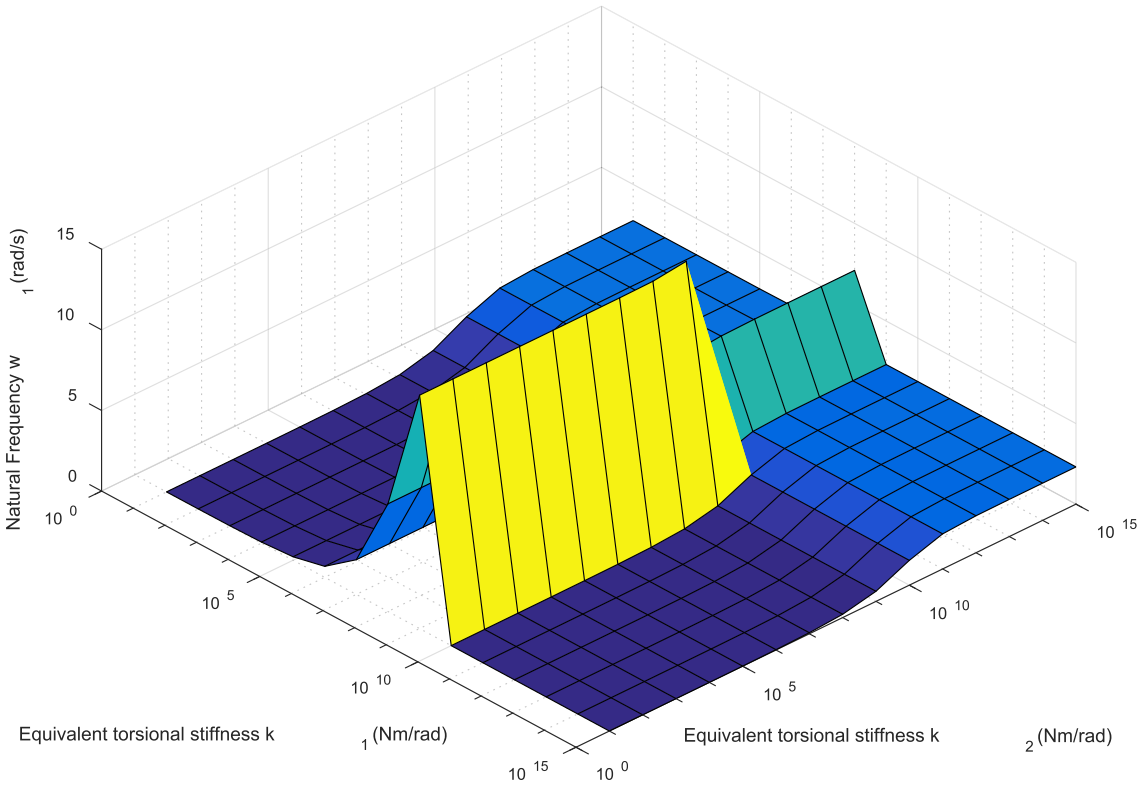

Figure 7-8 Variation of the first natural frequency of the tower structure with respect to both torsion spring stiffnesses in 3D plot

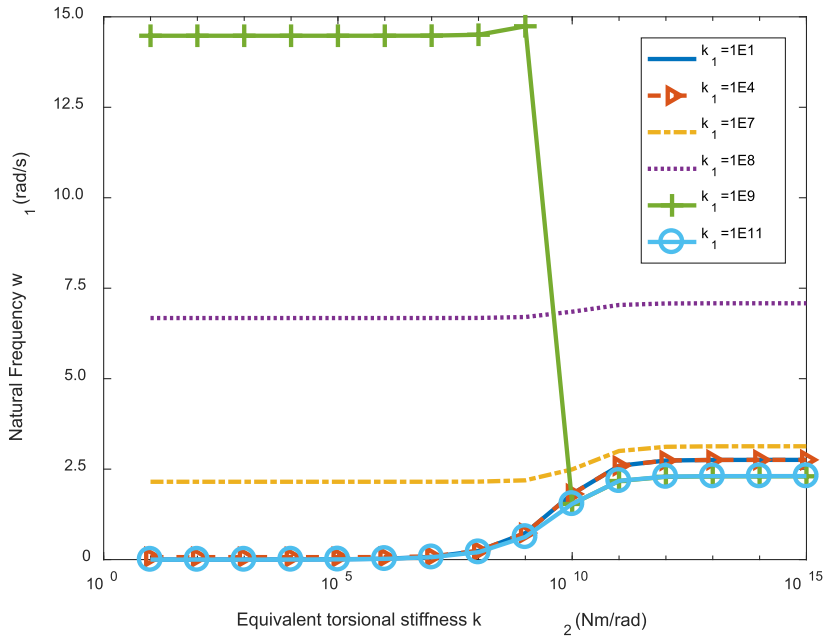

Figure 7-9 Variation of the first natural frequency of the tower structure with respect to torsional stiffness k_1

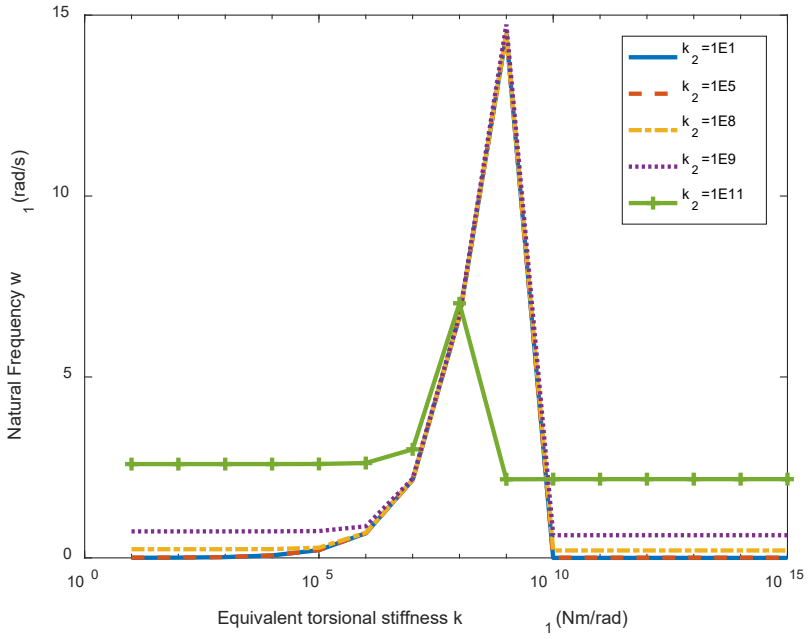

Figure 7-10 Variation of the first natural frequency of the tower structure with respect to torsional stiffness k_2

7.1.3. Effects of the end components

The moments of inertia of the end components about their own centre of gravity (CG) were assumed to be constants in the previous subsections. However, the moments of inertia about the ends of the tower can be different, depending on the distances from their CG to the respective tower ends. Figure 7-11 shows the effect of the location change of the CG of the platform along its vertical axis g_1 and the CG of the nacelle along its drive-train rotor axis in the horizontal direction $l_{oo'}$ on the first natural frequency. It can be seen that the change of $l_{oo'}$ does not significantly affect the variation of the natural frequency (less than 0.01% from Figure 7-12), which means the location of the CG of the nacelle along its rotational axis is not very important in the analysis of the natural frequency of the turbine structure. On the contrary, a closer location of the CG of the platform to the tower end would vibrate the whole system more due to its large mass. Although the natural frequency could be increased along with the distance g_1, the sensitivity is reduced

due to the increase of its moment of inertia related to the tower end. The variation of the natural frequency of the turbine structure with respect to the location of the CG of the platform can be found in Figure 7-11, has shown a non-linear relationship. The location of the CG of the platform has a slight effect on the natural frequency after $g_1 = 100m$.

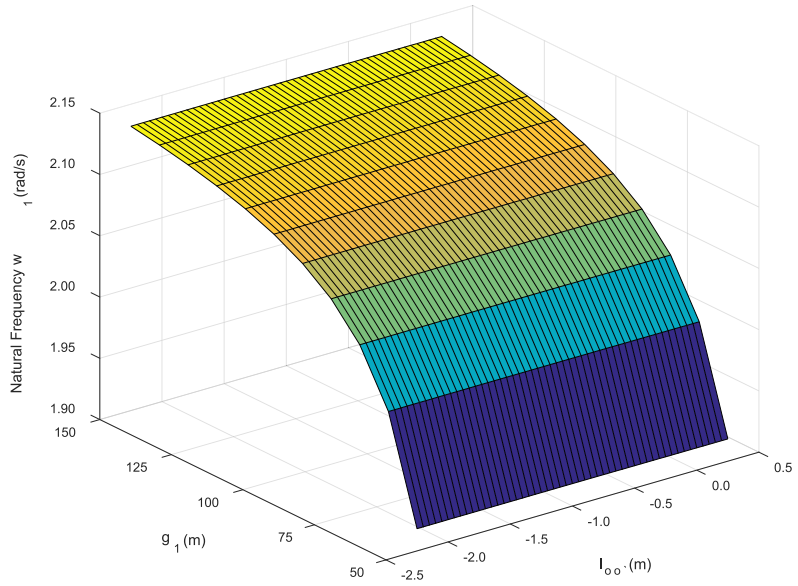

Figure 7-11 Variation of the first natural frequency of the whole system with respect to the distances between the tower ends and the CG of the end components

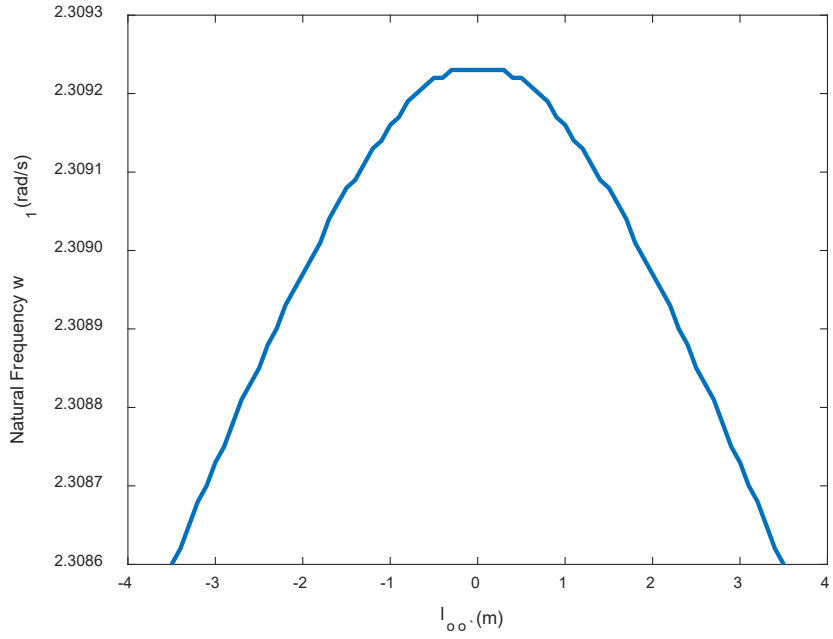

Figure 7-12 Variation of the first natural frequency of the tower structure with respect to the horizontal distance between the CG of the nacelle and the top end of the tower structure $l_{oo'}$.

7.2. Determination of the natural frequencies of a non-uniform tower structure

In this section, the non-uniform tower model will be used instead of the uniform tower structure. The tower structure with variable paremeters is illustrated in Figure 7-13. The total length of the tower are represented by L. The outter diameter and thickness at height l are shown as $D_{(l)}$ and $t_{(l)}$. For the uniform tower sturcture, constant vaules of the diameter and thickness are used. For the non-uniform case, the diameter and thickness at different height of the tower will be variable. Assume that the tower structure is divided into n element, the length of each element can be calculated as $\Delta h = L/n$. The difference of the element's parameter at its two ends should be small when n is large. Evidently, the cross section area and the moment of inertia of the elements are functions of their heights along the tower axis.

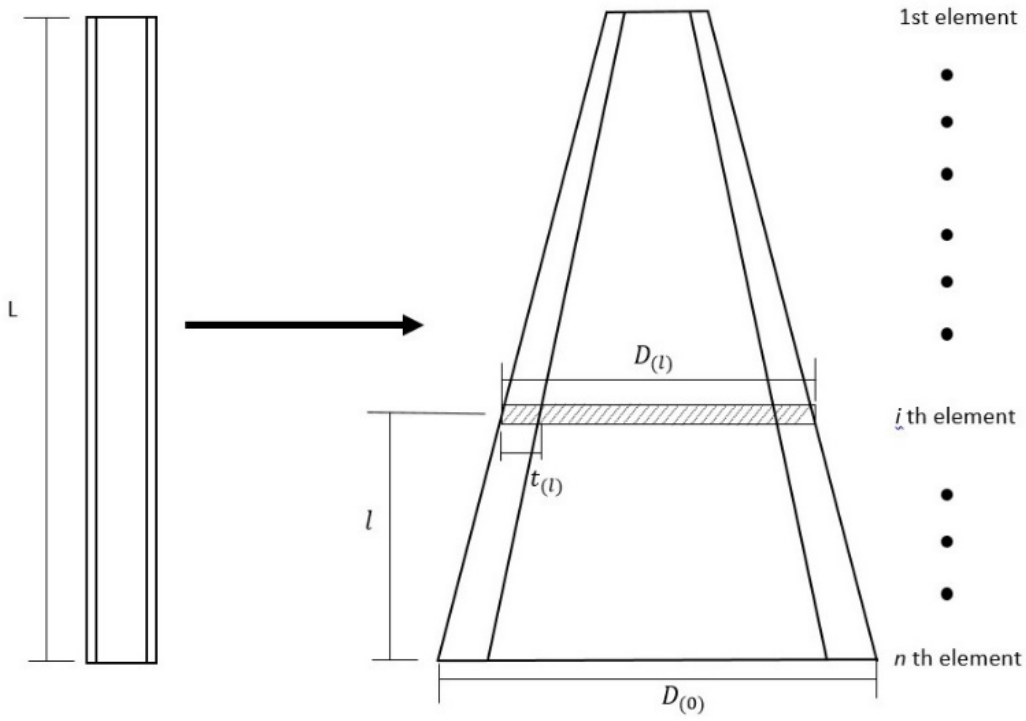

Figure 7-13 Non-uniform tower structures

Three types of elements are considered for the tower structure, namely top element ($1st$ element), body element (ith element for $i = 2, \cdots, n-1$) and bottom element (nth element). The top element and bottom element are contected with end masses, while the body elements are quite general beam elements, as shown in Figure 7-14.

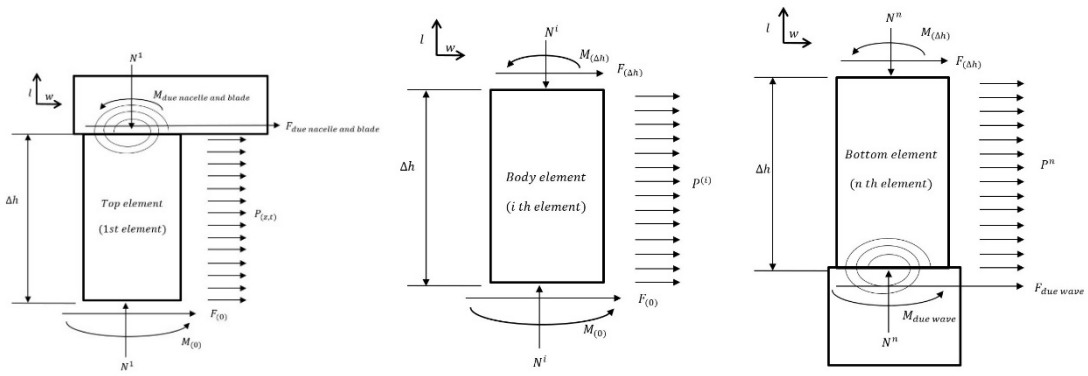

Figure 7-14 Element types for the tower structure

According to the equation of motion of the tower elements, Eq.(7.1), and the similar boundary conditions at the tower top and bottom, the bending moment and shear force equilibrium at the top of the $1st$ element and the bottom of the nth element can be the same as Eq.(7.3) to (7.6), as shown following

$$EIw_{(\Delta h)}^{(1)\,''} = I_{02}\omega^2\left(w_{(\Delta h)}^{(1)\,'} + \alpha_2\right) + g_2\, M_2\omega^2 w_{(\Delta h)}^{(1)}\, cos(\theta_2) \quad (7.9)$$

$$EIw_{(\Delta h)}^{(1)\,'''} + Nw_{(\Delta h)}^{(1)\,'} = -M_2\omega^2 w_{(\Delta h)}^{(1)} - g_2\, M_2\omega^2(w_{(\Delta h)}^{(1)} + \alpha_2)\, cos(\theta_2) \quad (7.10)$$

$$EIw_{(0)}^{(n)\,''} = -I_{01}\omega^2\left(w_{(0)}^{(n)\,'} - \alpha_1\right) - g_1\, M_1\omega^2 w_{(0)}^{(n)}\cos(\theta_1) \quad (7.11)$$

$$EIw_{(0)}^{(n)\,'''} + Nw_{(0)}^{(n)\,'} = M_1\omega^2 w_{(0)}^{(n)} + g_1\, M_1\omega^2 w_{(0)}^{(n)} - \alpha_1)\, cos(\theta_1) \quad (7.12)$$

The body elements, the bottom end of the top element and the top end of the bottom element are under quite general beam element conditions. For the *i* th element, the shear forces, bending moments and normal forces from other elements are represented as $\boldsymbol{F^{(i)}} = \left[F_{(\Delta h)}^{(i)}\; M_{(\Delta h)}^{(i)}\; F_{(0)}^{(i)}\; M_{(0)}^{(i)}\right]^T$ and $N^{(i)}$, respectively as shown in Figure 7-14. The wind drag force on the tower element will lead to two forces applied on the top and bottom of the element, represented as $\boldsymbol{P^{(i)}} = \left[\frac{P^{(i)}}{2}\;\frac{P^{(i)}\Delta h}{4}\;\frac{P^{(i)}}{2}\;\frac{-P^{(i)}\Delta h}{4}\right]^T$. The boundary conditions can be expressed as

$$\begin{aligned} EIw_{(\Delta h)}^{(i)\,''} &= M_{(\Delta h)}^{(i)} + \frac{P^{(i)}\Delta h}{4} \\ EIw_{(\Delta h)}^{(i)\,'''} + Nw_{(\Delta h)}^{(i)\,'} &= F_{(\Delta h)}^{(i)} + \frac{P^{(i)}}{2} \end{aligned} \quad \text{for } i = 2, \cdots, n \quad (7.13)$$

$$\begin{aligned} EIw_{(0)}^{(i)\,''} &= M_{(0)}^{(i)} - \frac{P^{(i)}\Delta h}{4} \\ EIw_{(0)}^{(i)\,'''} + Nw_{(0)}^{(i)\,'} &= F_{(0)}^{(i)} + \frac{P^{(i)}}{2} \end{aligned} \quad \text{for } i = 1, \cdots, n-1 \quad (7.14)$$

Substituting the free parameters (arbitrary constants) in the general solution in Eq.(7.2) for each element, $A_1^{(i)}$, $A_2^{(i)}$, $B_1^{(i)}$ and $B_2^{(i)}$, into a matrix form $\mathbf{C}^{(i)}$, and substituting the general solution Eq.(7.2) into the four boundary condition equation of each elements, Eq.(7.9)-(7.14) gives a rise to

$$\begin{bmatrix} R_{11}^{(i)} & R_{12}^{(i)} & R_{13}^{(i)} & R_{14}^{(i)} \\ R_{21}^{(i)} & R_{22}^{(i)} & R_{23}^{(i)} & R_{24}^{(i)} \\ R_{31}^{(i)} & R_{32}^{(i)} & R_{33}^{i)} & R_{34}^{(i)} \\ R_{41}^{(i)} & R_{42}^{(i)} & R_{43}^{(i)} & R_{44}^{(i)} \end{bmatrix} \begin{bmatrix} A_1^{(i)} \\ A_2^{(i)} \\ B_1^{(i)} \\ B_2^{(i)} \end{bmatrix} = \begin{bmatrix} F_{(\Delta h)}^{(i)} + \frac{P^{(i)}}{2} \\ M_{(\Delta h)}^{(i)} + \frac{P^{(i)}\Delta h}{4} \\ F_{(0)}^{(i)} + \frac{P^{(i)}}{2} \\ M_{(0)}^{(i)} - \frac{P^{(i)}\Delta h}{4} \end{bmatrix} \; or \; \mathbf{R}^{(i)}\mathbf{C}^{(i)} = \mathbf{F}^{(i)} + \mathbf{P}^{(i)} \quad (7.15)$$

where the elements of the matrix $\boldsymbol{R}^{(i)}$ are listed in Appendix 9.3.4 for brevity.

The expressions for the rotation angular ($\theta^{(i)}$), of the *i*th element can be written as

$$\theta_{(l)}^{(i)} = \frac{\partial w^{(i)}}{\partial l} \quad (7.16)$$

The vibration of the element, $\boldsymbol{W}^{(i)} = \begin{bmatrix} w_{(\Delta h)}^{(i)} & \theta_{(\Delta h)}^{(i)} & w_{(0)}^{(i)} & \theta_{(0)}^{(i)} \end{bmatrix}^T$ can be form the following matrix equations

$$\begin{bmatrix} w_{(\Delta h)}^{(i)} \\ \theta_{(\Delta h)}^{(i)} \\ w_{(0)}^{(i)} \\ \theta_{(0)}^{(i)} \end{bmatrix} = \begin{bmatrix} \lambda_1^{(i)} S & \lambda_1^{(i)} CH & \lambda_2^{(i)} C & \lambda_2^{(i)} SH \\ \lambda_1^{(i)} C & -\lambda_1^{(i)} S & \lambda_2^{(i)} CH & \lambda_2^{(i)} SH \\ 0 & 1 & 0 & 1 \\ \lambda_1^{(i)} & 0 & \lambda_2^{(i)} & 0 \end{bmatrix} \begin{bmatrix} A_1^{(i)} \\ A_2^{(i)} \\ B_1^{(i)} \\ B_2^{(i)} \end{bmatrix} \; or \; \boldsymbol{W}^{(i)} = \boldsymbol{T}^{(i)}\boldsymbol{C}^{(i)} \quad (7.17)$$

The free parameters matrix, $\mathbf{C}^{(i)}$ can be eliminated from Eq.(7.15) and (7.17) as follows

$$\begin{bmatrix} F_{(\Delta h)}^{(i)} + \frac{P^{(i)}}{2} \\ M_{(\Delta h)}^{(i)} + \frac{P^{(i)}\Delta h}{4} \\ F_{(0)}^{(i)} + \frac{P^{(i)}}{2} \\ M_{(0)}^{(i)} - \frac{P^{(i)}\Delta h}{4} \end{bmatrix} = \begin{bmatrix} E_{11}^{(i)} & E_{12}^{(i)} & E_{13}^{(i)} & E_{14}^{(i)} \\ E_{21}^{(i)} & E_{22}^{(i)} & E_{23}^{(i)} & E_{24}^{(i)} \\ E_{31}^{(i)} & E_{32}^{(i)} & E_{33}^{(i)} & E_{34}^{(i)} \\ E_{41}^{(i)} & E_{42}^{(i)} & E_{43}^{(i)} & E_{44}^{(i)} \end{bmatrix} \begin{bmatrix} w^{(i)}{}_{(\Delta h)} \\ \theta^{(i)}{}_{(\Delta h)} \\ w^{(i)}{}_{(0)} \\ \theta^{(i)}{}_{(0)} \end{bmatrix} \; or \; \mathbf{F^{(i)}} + \mathbf{P^{(i)}} = \boldsymbol{E^{(i)} W^{(i)}} \; (7.18)$$

where

$$\begin{bmatrix} E_{11}^{(i)} & E_{12}^{(i)} & E_{13}^{(i)} & E_{14}^{(i)} \\ E_{21}^{(i)} & E_{22}^{(i)} & E_{23}^{(i)} & E_{24}^{(i)} \\ E_{31}^{(i)} & E_{32}^{(i)} & E_{33}^{(i)} & E_{34}^{(i)} \\ E_{41}^{(i)} & E_{42}^{(i)} & E_{43}^{(i)} & E_{44}^{(i)} \end{bmatrix}$$

$$= \begin{bmatrix} R_{11}^{(i)} & R_{12}^{(i)} & R_{13}^{(i)} & R_{14}^{(i)} \\ R_{21}^{(i)} & R_{22}^{(i)} & R_{23}^{(i)} & R_{24}^{(i)} \\ R_{31}^{(i)} & R_{32}^{(i)} & R_{33}^{i)} & R_{34}^{(i)} \\ R_{41}^{(i)} & R_{42}^{(i)} & R_{43}^{(i)} & R_{44}^{(i)} \end{bmatrix} \begin{bmatrix} \lambda_1^{(i)} S & \lambda_1^{(i)} CH & \lambda_2^{(i)} C & \lambda_2^{(i)} SH \\ \lambda_1^{(i)} C & -\lambda_1^{(i)} S & \lambda_2^{(i)} CH & \lambda_2^{(i)} SH \\ 0 & 1 & 0 & 1 \\ \lambda_1^{(i)} & 0 & \lambda_2^{(i)} & 0 \end{bmatrix}^{-1}$$

$$or \; \boldsymbol{E^{(i)}} = \boldsymbol{R^{(i)} T^{(i)^{-1}}} \quad (7.19)$$

From Figure 7-15, it is known that the displacements of the bottom of the $\boldsymbol{ith}$ element ($v_{(0)}^{(i)}$& $\theta_{(0)}^{(i)}$) should be the same as the displacements of the top of the $\boldsymbol{i+1th}$ element ($v_{(\Delta h)}^{(i+1)}$& $\theta_{(\Delta h)}^{(i+1)}$), while the shear forces, bending moments and normal forces at the bottom of the $i+1th$ element and the top of the ith element are the action and reaction forces, which also means $F_{(0)}^{(i)}+F_{(\Delta h)}^{(i+1)}=0$, $M_{(0)}^{(i)}+M_{(\Delta h)}^{(i+1)}=0$ and $N^{(i+1)}=N^{(i)}+m^{(i)}$, where $m^{(i)}$ is the self-weight of the ith element.

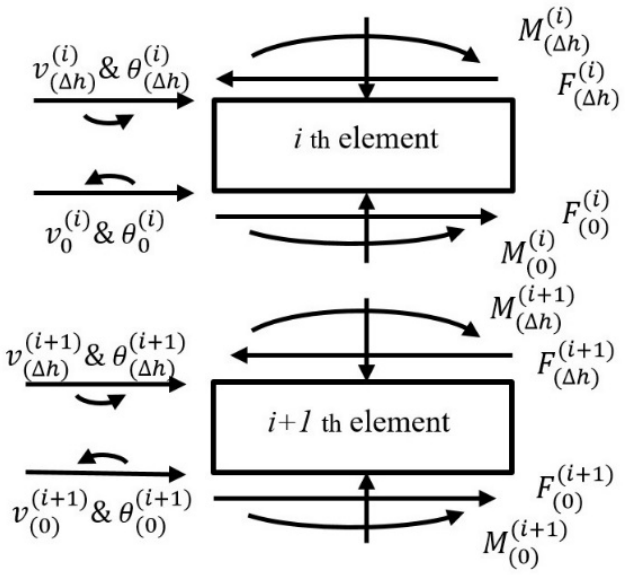

Figure 7-15 Interaction of elements

Thus the equation of the motion of the tower structure in the matrix form can be represented as,

$$\begin{bmatrix} F_{(\Delta h)}^{(1)} + \frac{P^{(1)}}{2} \\ M_{(\Delta h)}^{(1)} + \frac{P^{(1)}\Delta h}{4} \\ F_{(0)}^{(1)} + \frac{P^{(1)}}{2} + F_{(\Delta h)}^{(2)} + \frac{P^{(2)}}{2} \\ M_{(0)}^{(1)} - \frac{P^{(1)}\Delta h}{4} + M_{(\Delta h)}^{(2)} - \frac{P^{(2)}\Delta h}{4} \\ \vdots \\ F_{(0)}^{(n)} + \frac{P^{(n)}}{2} \\ M_{(0)}^{(n)} - \frac{P^{(n)}\Delta h}{4} \end{bmatrix} =$$

$$\begin{bmatrix} E_{11}^{(1)} & E_{12}^{(1)} & E_{13}^{(1)} & E_{14}^{(1)} & & & & & \\ E_{21}^{(1)} & E_{22}^{(1)} & E_{23}^{(1)} & E_{24}^{(1)} & \cdots & & 0 & & \\ E_{31}^{(1)} & E_{32}^{(1)} & E_{33}^{(1)}+E_{11}^{(2)} & E_{34}^{(1)}+E_{12}^{(2)} & & & & & \\ E_{41}^{(1)} & E_{42}^{(1)} & E_{43}^{(1)}+E_{21}^{(2)} & E_{44}^{(1)}+E_{22}^{(2)} & & & & & \\ & & \vdots & & \ddots & & \vdots & & \\ & & & & & E_{33}^{(n-1)}+E_{11}^{(n)} & E_{34}^{(n-1)}+E_{12}^{(n)} & E_{13}^{(n)} & E_{14}^{(n)} \\ & & 0 & & \cdots & E_{43}^{(n-1)}+E_{21}^{(n)} & E_{44}^{(n-1)}+E_{22}^{(n)} & E_{23}^{(n)} & E_{24}^{(n)} \\ & & & & & E_{31}^{(n)} & E_{32}^{(n)} & E_{33}^{(n)} & E_{34}^{(n)} \\ & & & & & E_{41}^{(n)} & E_{42}^{(n)} & E_{43}^{(n)} & E_{44}^{(n)} \end{bmatrix}.$$

$$\begin{bmatrix} w_{(\Delta h)}^{(1)} \\ \theta_{(\Delta h)}^{(1)} \\ w_{(0)}^{(1)}\ (w_{(\Delta h)}^{(2)}) \\ \theta_{(0)}^{(1)}(\theta_{(\Delta h)}^{(2)}) \\ \vdots \\ w_{(0)}^{(n)} \\ \theta_{(0)}^{(n)} \end{bmatrix} \quad or\ \mathbf{F}^{\boldsymbol{tower}} + \mathbf{P}^{\boldsymbol{tower}} = \boldsymbol{E}^{\boldsymbol{tower}}\boldsymbol{W}^{\boldsymbol{tower}} \qquad (7.20)$$

By considering a free-vibration condition, where $\mathbf{P}^{\boldsymbol{tower}}$=0, $\mathbf{N}^{\boldsymbol{tower}}$=0, the vibration of the whole tower $\boldsymbol{W}^{\boldsymbol{tower}}$ is generally non-zero, the $\boldsymbol{E}^{\boldsymbol{tower}}$ matrix should have a zero solution as

$$\det\left[E_{ij}^{tower}\right] = 0 \qquad (7.21)$$

The transcendental equation is solved using symbolic calculation method in MATLAB to obtain numerical results.

7.2.1. Numerical simulation results

By considering a mulit-element tower model but using an average tower diameter and shell thickness, the first three natural frequencies are different according to their element number, *n*, as shown in Table 7-4 and Figure 7-16. By comparing to the natural

frequencies obtained from the uniform tower structure in Section 7.1, it can be observed that the natural frequency shows a better agreement when the number of element is increased.

However, if take the *n* value into the mode shape under wind excitation (only) condition, as shown in Figure 7-17, the first mode shape of n=20 element shows a large difference with n=40 and higher (the higher value of *n* makes the mode shape convergence). Then at least a value of over 40 elements are further required for the higher accuracy. Thus the following section will use n=40 in order to achieve a reasonable high accuracy and less simulation time.

Table 7-4 Natural frequency under different n

		Element number n						
		2	3	5	10	20	40	80
nth order natural frequency	1	0.4800	0.855	1.36	1.949	2.239	2.332	2.357
	2	15.8090	16.230	17.318	19.917	22.316	23.391	23.716
	3	63.7550	63.933	64.437	65.972	68.023	69.262	69.692

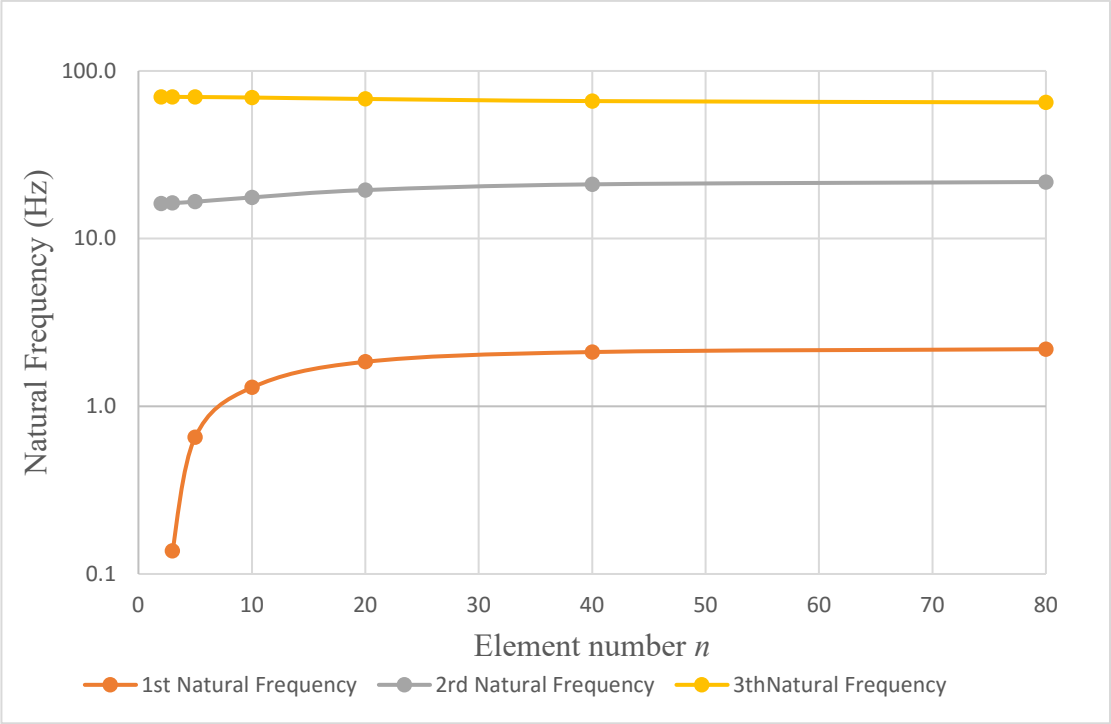

Figure 7-16 Natural frequency under different element number, n

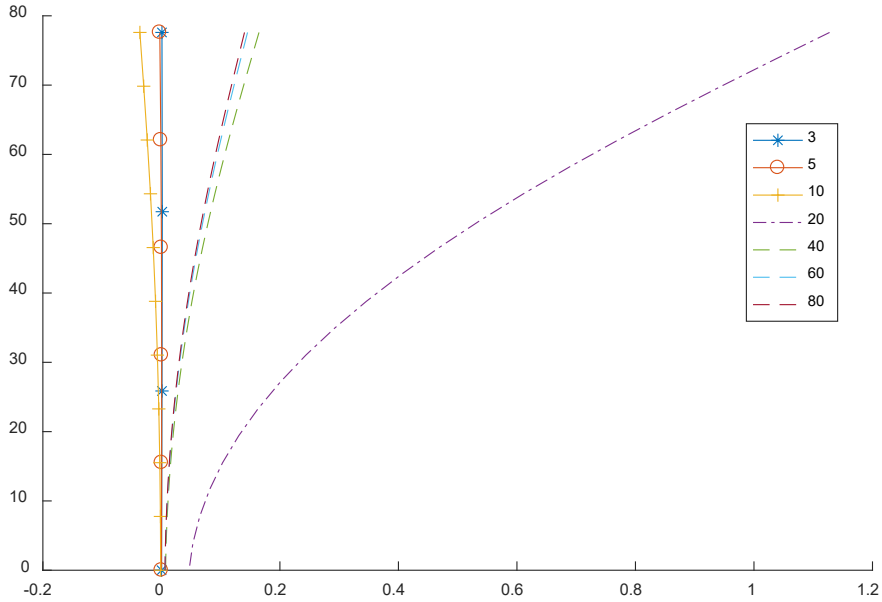

Figure 7-17 First mode shape under wind condition only with different n

By using the average tower diameter and shell thickness in the mulit-element tower model, with n=40 element, the first natural frequency is variable with its diameter and

thickness as shown in Figure 7-18. However, different from the other free-vibration beam analysis, the self-weight of the tower structure is also considered. The self-weight of each element could cause an additional normal force applied on the element below. From Eq.(7.2), it can be found that the normal force applied on the element could affect its motion. Thus in the improved tower model, the element self-weight will be added to the normal force on the element below.

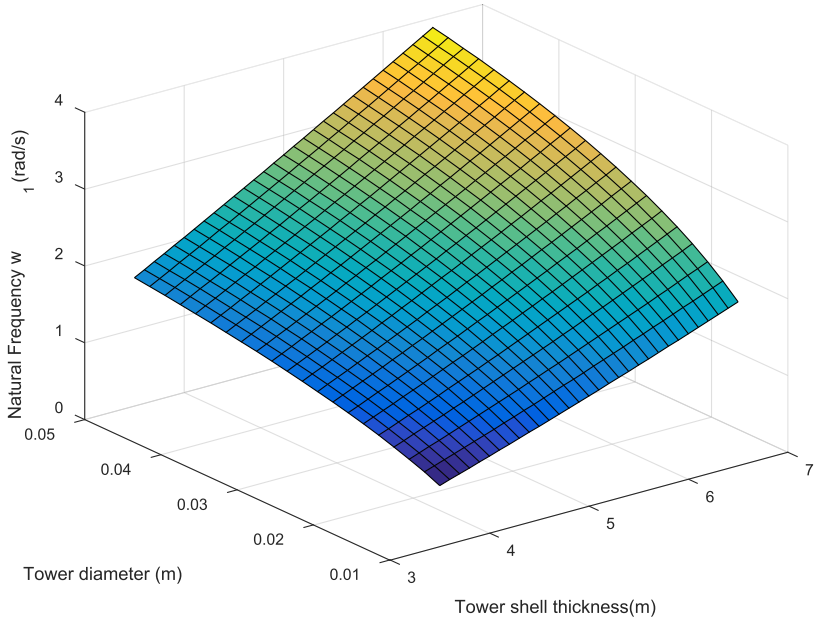

Figure 7-18 Natural frequency VS thickness and diameter (self-weight)

To consider the non-uniform tower case, a constant shell thickness of 0.3m is first applied. Assume that the diameter at the bottom of the tower is fixed at 6.5m and the diameter of the tower along its axis is linearly reduced. The natural frequency of the whole wind turbine with non-uniform tower structure according to its top diameter is shown in Figure 7-19 (a). The natural frequency of the tower model is found at 3.3 rad/s when the top diameter D_top=6.5m and at 2.82 rad/s when D_top=3.5m. The difference of over 21% can be found when the top diameter reduced from 6.5 to 3.5m.

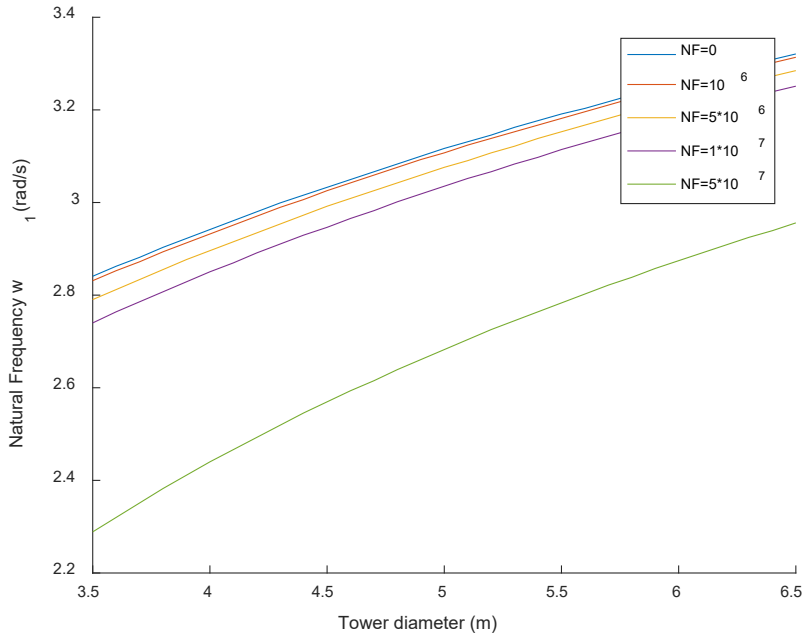

Figure 7-19 Natural frequency VS diameter (a) normal force=0, (b) with normal forces

Similar, in regard to the change of its shell thickness, a constant diameter of 6.5m is applied. The shell thickness at the bottom of the tower is fix at 0.03m and is linearly reducing along the tower axis. The natural frequency of the wind turbine is shown in Figure 7-20 (a). The first mode natural frequency is found as 2.6 rad/s when t_top=0.01m, and 2.9 rad/s when t_top=0.05m. A difference of over 11.5% can be found when the top shell thickness is increased from 0.01 to 0.05m.

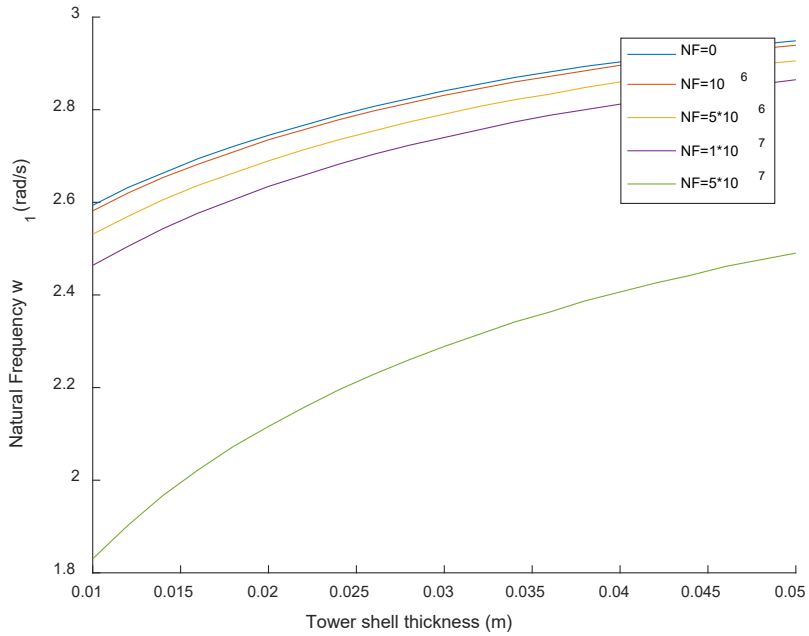

Figure 7-20 Natural frequency VS thickness (a) normal force=0 (b) with normal forces

Additional force in the normal direction can be applied on the wind turbine due to the wind or water (current or bouncy). Figure 7-19(b) and 7-20(b) show the natural frequency difference of the non-uniform tower parameter under an additional normal force. The reduction of its natural frequency due to the increase of the normal force is nonlinear. When normal forces increase from 0 to $10^7 N$, the average reduction of its natural frequency is only about 3%, but when the normal force is increased from $10^7 N$ to $5 \times 10^7 N$, the reduction ratio has increased to 30%. This means that small value of the normal force will not affect its natural frequency but oversized force will dampen the vibration of the whole system.

A combined consideration of wind turbine with a non-uniform tower structure, the natural frequency of the system is shown in Figure 7-21. By comparing with the natural frequency for a uniform tower structure with D=6.5m and t=0.03m, which is 3.32 rad/s, the non-uniform tower structure can save much amount of mass but affect its natural frequency less. According to Figure 7-22, by narrowing either diameter or shell thickness at the top

section of the tower structure, the natural frequency of the whole model could lead to the maximum reduction of about 20%, but the total mass can be saved up to 60%.

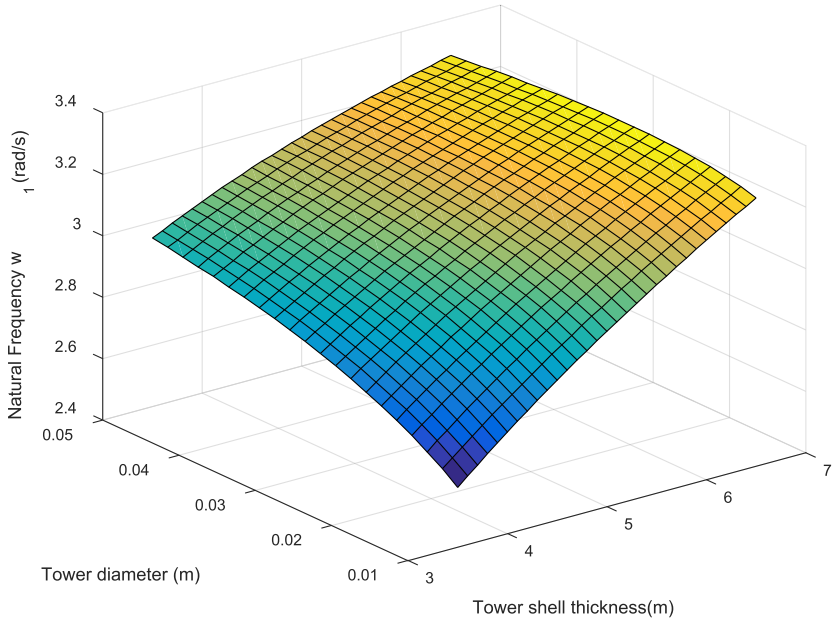

Figure 7-21 3D natural frequency of the non-uniform tower with different diameter and thickness

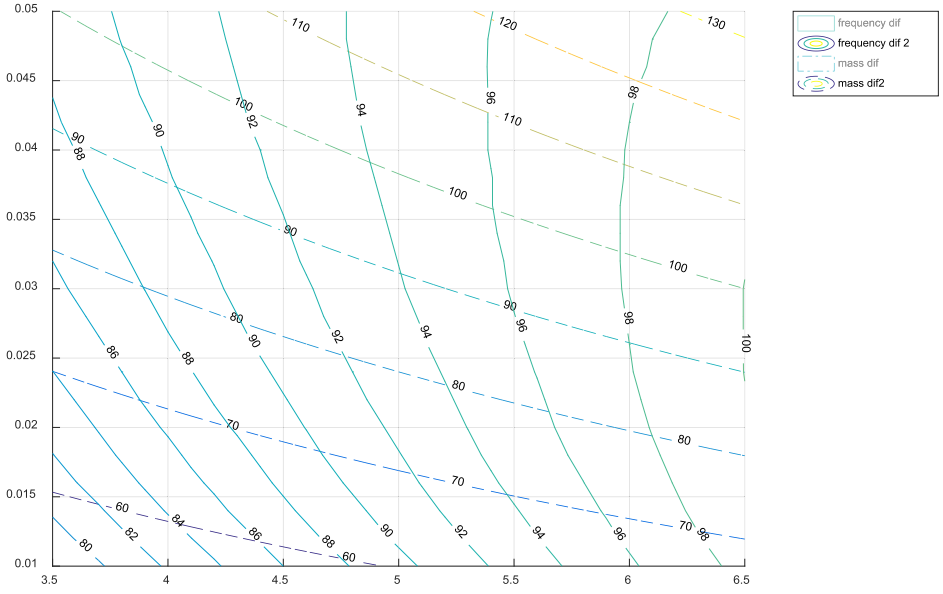

Figure 7-22 Natural frequency and mass differences between the uniform tower and non-uniform tower

7.3. Conclusion

The free-vibration of the tower structure of a spar-type floating offshore wind turbine has been investigated using a free-free end beam model with end components. The natural frequencies of the whole system were derived from the characteristic equation based on the Euler-Bernoulli beam theory.

A uniform tower structure was considered firstly. The numerical simulation results of the natural frequencies and the mode shapes of the tower structure have shown good agreement with the FEA simulation results from the previously published papers. Several parameters, including the tower diameter, shell thickness, mass density (due to the presence of non-structure mass), the torsional stiffness at the connecting locations and the positions of the CG of the end components relative to the ends of the tower, have been considered in studying their effects on the natural frequency of the tower structure. An increase of the mass density due to the non-structure components was found to make a linear reduction of the natural frequency, while an increase of both tower diameter and shell thickness could increase the natural frequency. The effect of the variation of the diameter or thickness at a small thickness or diameter (small size of the tower) is larger than at a large thickness or diameter (large size of the tower). High sensitivity of the natural frequency was found in the reduction of either k_1 or k_2 from 10^{10} to $10^5\ Nm/rad$, indicating that the tower structure could be unstable when the joint is weak or a crack exists. The horizontal distance of the CG of the nacelle to the tower axis (yaw axis) was found to have negligible effect on the natural frequency of the whole system. A lower location of the CG of the platform corresponding to the bottom end of the tower would stabilize the whole system.

Then the tower part has been developed by using a non-uniform structure. A mulit-elements model was used to improve its numerical results. The total mass of the tower section were found can be greatly reduced by using the non-uniform parameters but have less effect on the natural frequency of the whole system. Additional forces in the normal direction were also found to have a slight effect when it is small, while large forces can reduce the natural frequency quickly.

It is expected that the simple analytical method presented in this chapter would be easily applicable to the calculation of the natural frequencies of the different floating type wind turbines to ensure the turbine tower within the desired safe frequency range.

8. Conclusions and future research

An overview of the offshore direct-drive wind turbines has been presented firstly. Different concepts of the direct-drive generators were discussed and compared in terms of their advantages and disadvantages. The subsystems involved in the nacelle were also given. The tower and supporting structure were reviewed based on their classifications. A reference list used for further study on the vibration behaviour of the offshore wind turbine systems was provided, with particular considerations on studying the dynamic performance of the wind turbines. Both environmental and internal excitations have been included. The effects of aerodynamic and hydrodynamic excitations being applied on the wind turbines and the interaction of the tower/nacelle (rotating) system and the tower/blade system have been discussed. However, as the simulation of a complete system can be very difficult, a certain subsystem level is recommended to perform the validation. Therefore, although many existing studies have been done on the generator optimization and subsystem design, there still are some unaddressed issues when combining the interaction between each system, due to the lack of knowledge of how they interact. It is believed that more field data can change this situation in the future.

In this thesis, three new models have been presented. For the analysis of the direct-drive drive-train system, a double bearing generator model was developed as a 4DOF nonlinear system. The vibration response of the drive-train system was found to be related to its rotor position and mass ratio. The bearing forces, wind excitation were applied. The comparison results of the consideration of the UMP force indicate an up to 30% notable difference in the allowable tolerance of air-gap under a workable operation. Thus, the UMP force needed to be considered. According to the simulation results, the effect of the

rotor position adjustment could give significant change on its displacement magnitude but less change on the response frequency, while the effect of the rotor mass adjustment is not as significant as the effect of the rotor position adjustment.

After that, the dynamic response of a spar-type floating direct-drive wind turbine caused by both hydrodynamic and aerodynamic excitations was studied. The comparison of the effects of the current, wave and wind excitations shows that the nacelle's mean displacement response is primarily wind induced and its standard deviation is primarily wave induced. It was found that the interaction in the drive-train system is not only caused by self-rotating motion of the drive-train system but also caused by the global translational motion. However, the comparison of performance indicated that the effect of interaction between the drive-train system and the nacelle on the dynamic response of the drive-train system itself can be ignored with little percentage difference, whereas the effect on the spar support with tower structure is notable but not significant. The directions of the wind and wave spreading correlated to the sea current direction were also considered to form a complete 3D description of the deep-sea environment. By considering the interaction, the mean value and the standard deviation of the nacelle motion could lead to a 20% change in the surge direction and a 10% change in the sway direction. The effect of the interaction was found to be enhanced at the mean value but would be reduced at the standard deviation when the sea condition is stronger (wind speed is higher).

Lastly, the free-vibration of the tower structure of a spar-type floating offshore wind turbine has been investigated using a free-free end beam model with end components. The natural frequencies of the whole system were derived from the characteristic equation based on the Euler-Bernoulli beam theory. A uniform tower structure was considered

firstly. The numerical results of the natural frequencies and the mode shapes of the tower structure have shown good agreement with the FEA simulation results from the previously published papers. Several parameters, including the tower diameter, shell thickness, mass density (due to the presence of non-structure mass), the torsional stiffness at the connecting locations and the positions of the CG of the end components relative to the ends of the tower, were considered. An increase of the mass density due to the non-structure components was found to make a linear reduction of the natural frequency, while an increase of both tower diameter and shell thickness could increase the natural frequency. The effect of the variation of the diameter or thickness at a small thickness or diameter (small size of the tower) is larger than at a large thickness or diameter (large size of the tower). High sensitivity of the natural frequency was found when the joint was weak or a crack existed. Then the tower part was developed by using a non-uniform structure. A mulit-elements model was used to improve its numerical results. It was found that the total mass of the tower section can be greatly reduced by using the non-uniform parameters but have less effect on the natural frequency of the whole system. Additional forces in the normal direction were also found to have a slight effect when they were small, while large forces can reduce the natural frequency quickly.

Based on the review of new models developed, several observations can be summarized as follows;

- The offshore direct-drive wind turbines demonstrate a significant improvement on the power production and system reliability when comparing to the indirect-drive turbines, as there exists an abundant wind source with less environmental issues for offshore wind turbines. There is great potential on further optimizations on the weight, cost and design of offshore wind turbines.

- The combination of different excitations is necessary when studying the dynamic response of the complete wind turbine system. The consideration of the interaction between main subsystems can increase the accuracy of the simulation results, but only a certain subsystem level is recommended due to the cost and technology issues.
- The research on dynamic analysis of offshore wind turbines is still in its infancy. Offshore wind turbines have many different types of supporting structures and are subjected to complicated loading conditions. The supporting structures of the wind turbines with a fixed-base have been developed from land to transitional-water, more complex design has been used to meet the environment requirements. Floating platforms for deep-water wind turbines have been developed for their advantages of more power output and less limitation than the land-based turbines. A deep understanding of the dynamics of offshore wind turbines will help the designers and operators to optimize wind turbines in a more efficient and reliability way, thereby increasing the power output and reducing the maintenance cost.

In addition, further studies upon this thesis can be conducted. The blade and pitch system can be detail modelled in either the drive-train system or platform system when studying the effect of the wind on the wind turbine. This consideration can have a direct effect on the performance of the force and moment on the drive-train system and can also help with the study of the tower shadow. Furthermore, the flexible tower system can be used instead of the rigid tower structure in the platform model. More complex structures and special considerations can be applied at the joint sections between the tower and other components. Yaw bearing system and additional systems, such as wave damper, can be

considered to help with the performance of the entire wind turbine in the deep-sea environment.

9. Appendices

9.1. Additional figures for Chapter 5

9.1.1. The vibration performance of the CG and the rotor at different l and rpm

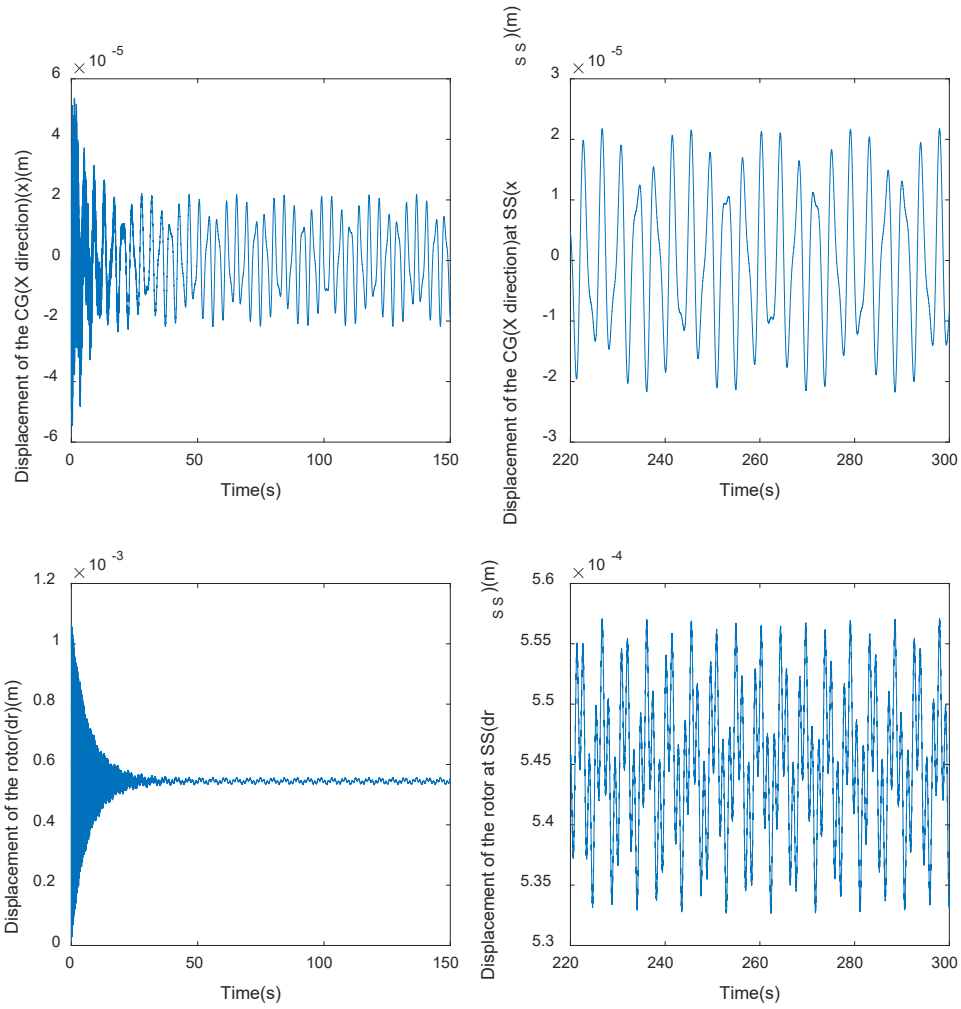

Time-history of the displacement of the CG and the rotor when $l = 0.0m$ at 16 rpm. The left and right subfigures show the transient and steady-state response, respectively.

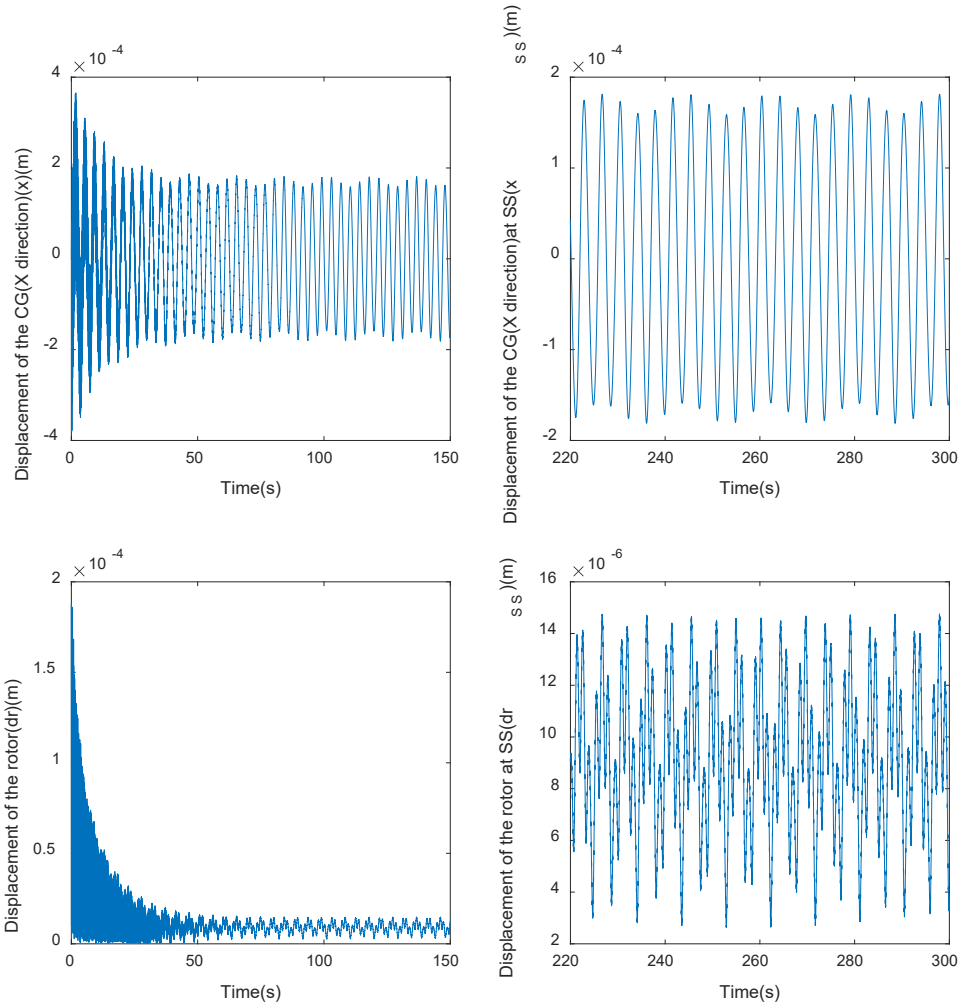

Time-history of the displacement of the CG and the rotor when $l = 1.7m$ at 16 rpm. The left and right subfigures show the transient and steady-state response, respectively.

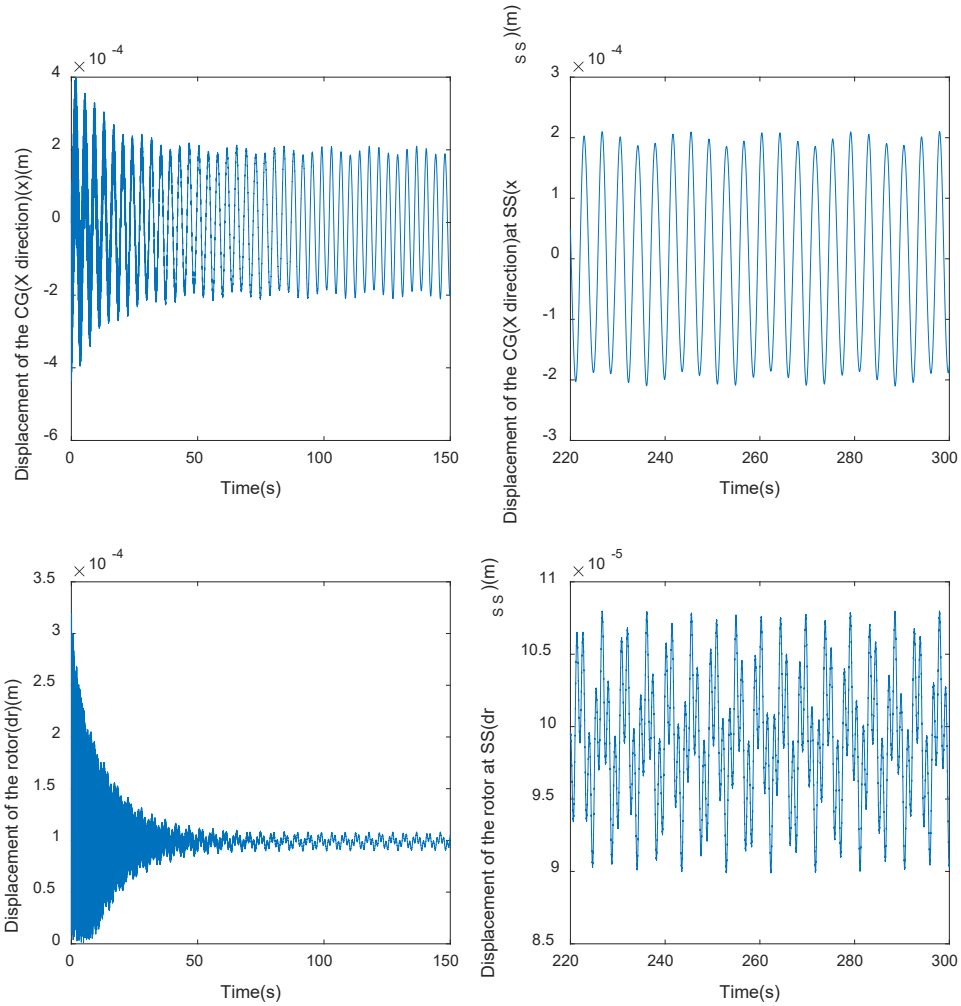

Time-history of the displacement of the CG and the rotor when $l = 2.0m$ at 16 rpm. The left and right subfigures show the transient and steady-state response, respectively.

9.1.2. The vibration performance of the CG and the rotor at different mass ratio

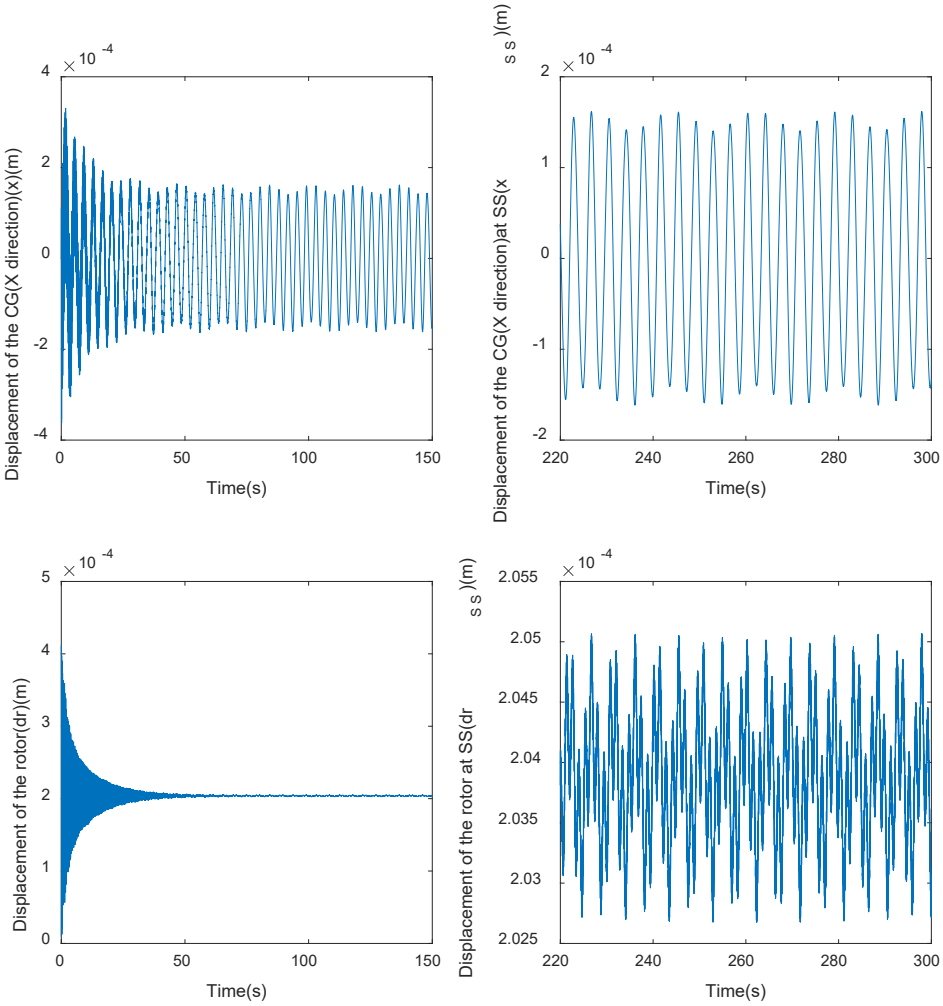

Time-history of the displacement of the CG and the rotor when mass ratio=0.25 at 16 rpm. The left and right subfigures show the transient and steady-state response, respectively.

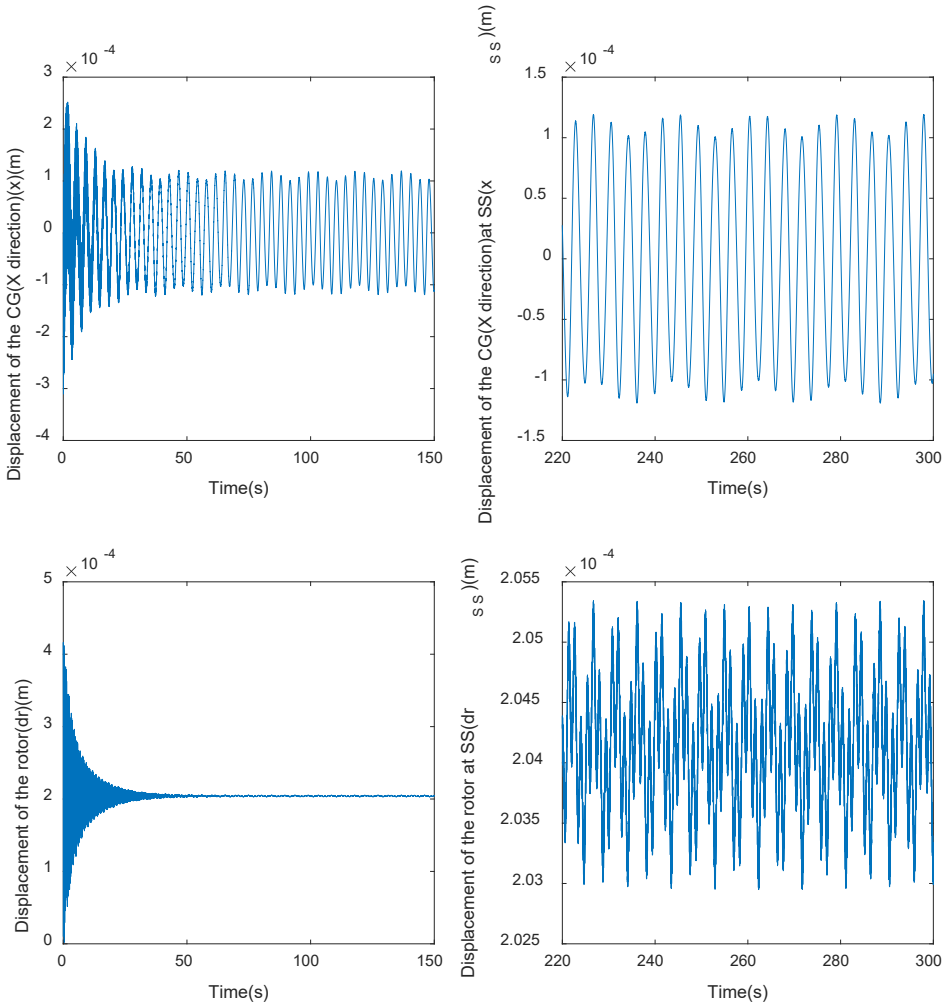

Time-history of the displacement of the CG and the rotor when mass ratio=0.40 at 16 rpm. The left and right subfigures show the transient and steady-state response, respectively.

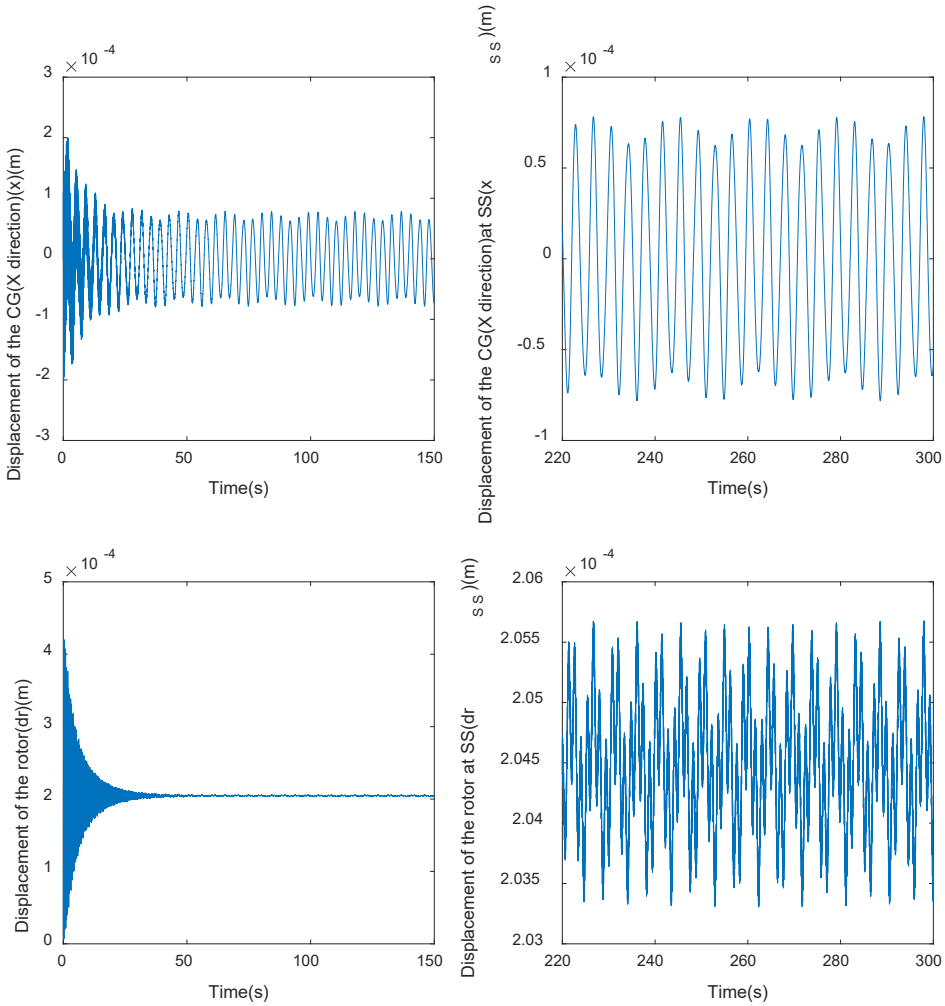

Time-history of the displacement of the CG and the rotor when mass ratio=0.60 at 16 rpm. The left and right subfigures show the transient and steady-state response, respectively.

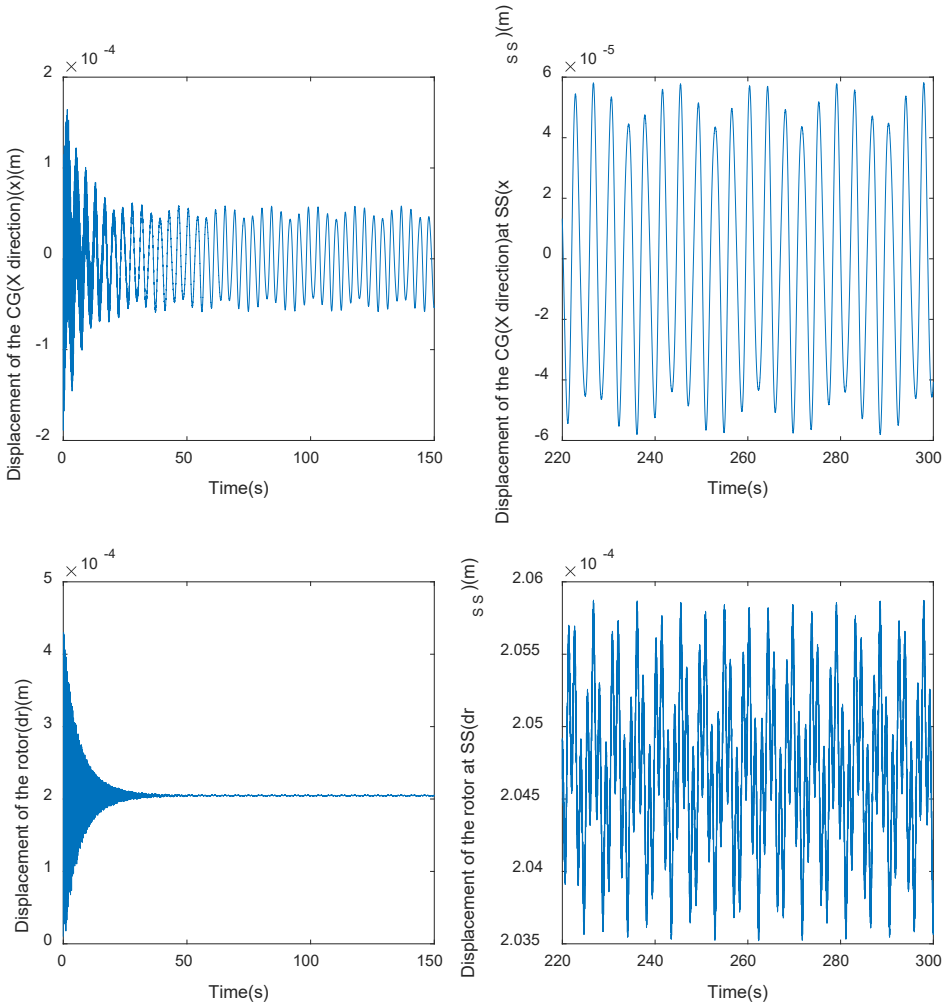

Time-history of the displacement of the CG and the rotor when mass ratio=0.73 at 16 rpm. The left and right subfigures show the transient and steady-state response, respectively.

9.1.3. The vibration performance of the bearings at different mass ratio

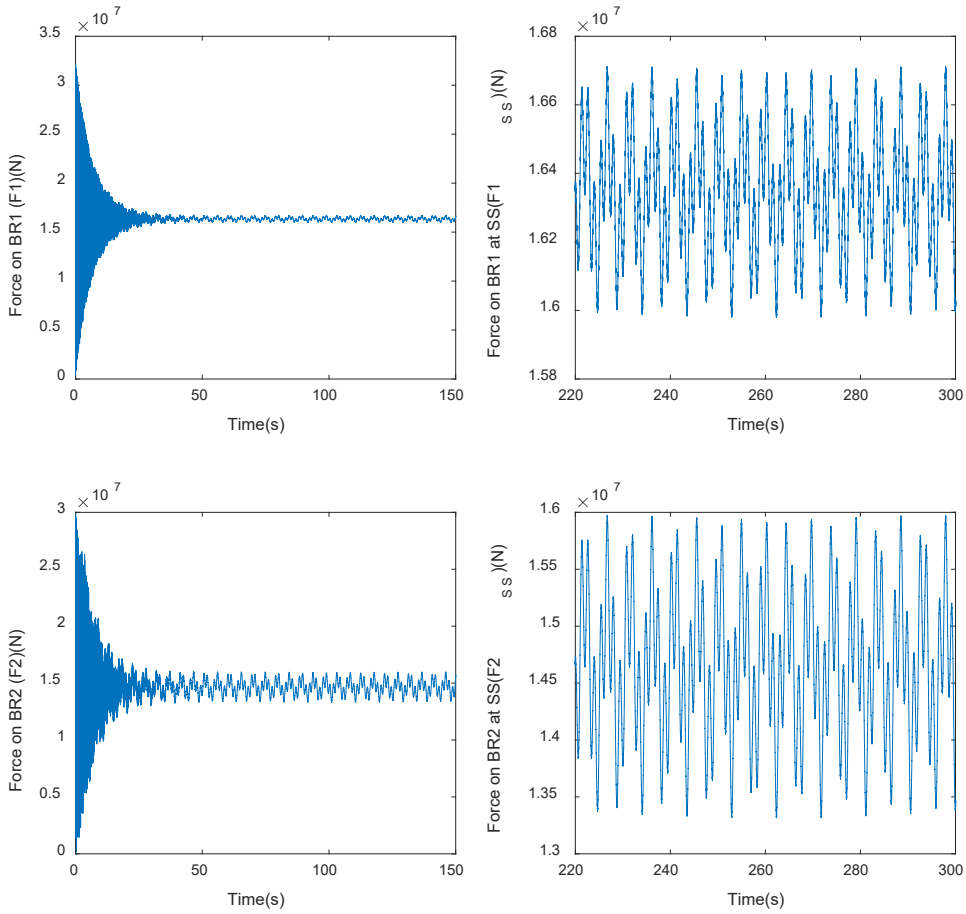

Bearing force response when $l = 0.0$m at 16 rpm , (a) force on Bearing 1, (b) force on Bearing 2. The left and right subfigures show the transient and steady-state response, respectively.

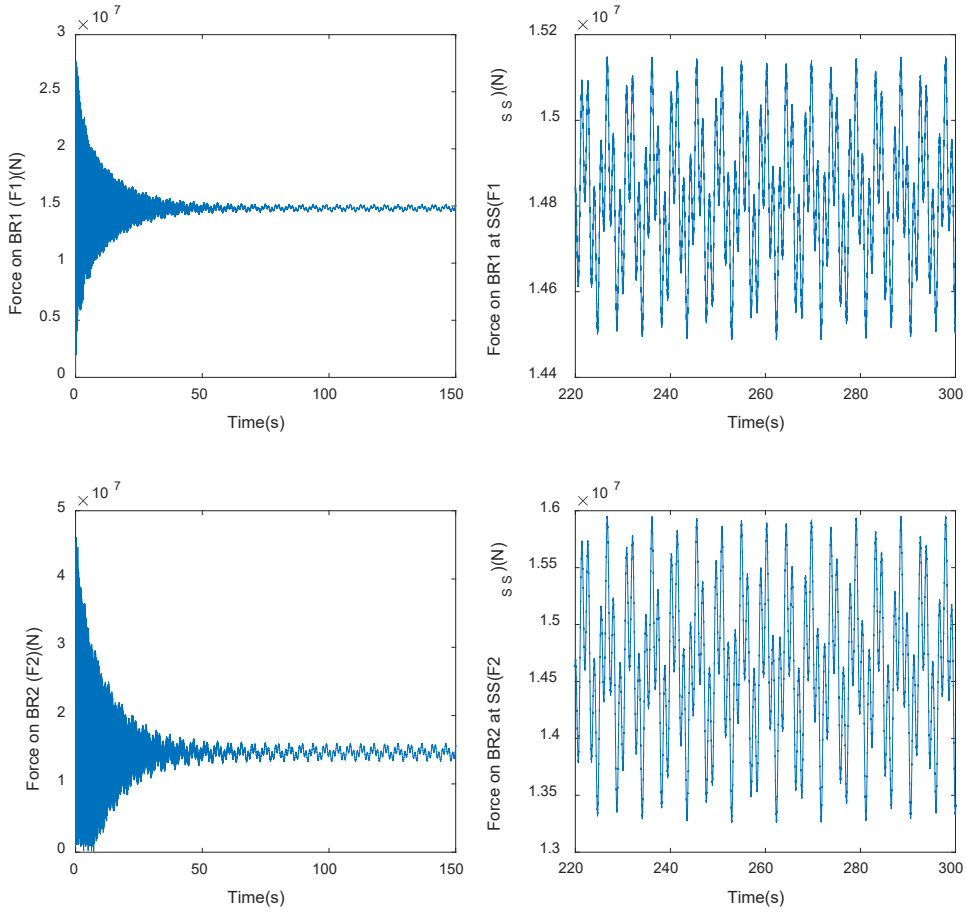

Bearing force response when $l = 1.7$m at 16 rpm , (a) force on Bearing 1, (b) force on Bearing 2. The left and right subfigures show the transient and steady-state response, respectively.

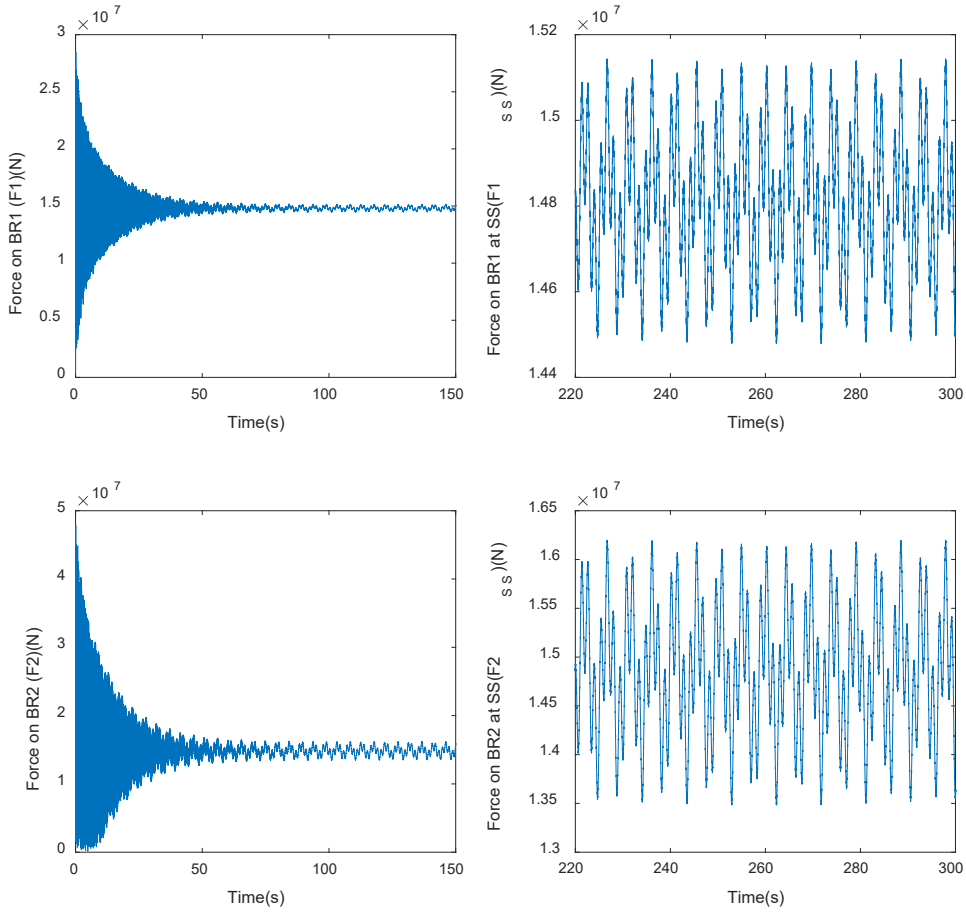

Bearing force response when $l = 2.0$m at 16 rpm , (a) force on Bearing 1, (b) force on Bearing 2. The left and right subfigures show the transient and steady-state response, respectively.

9.2. Additional figures for Chapter 6

9.2.1. The time history of the random surface elevation of the sea and the loads on the platform

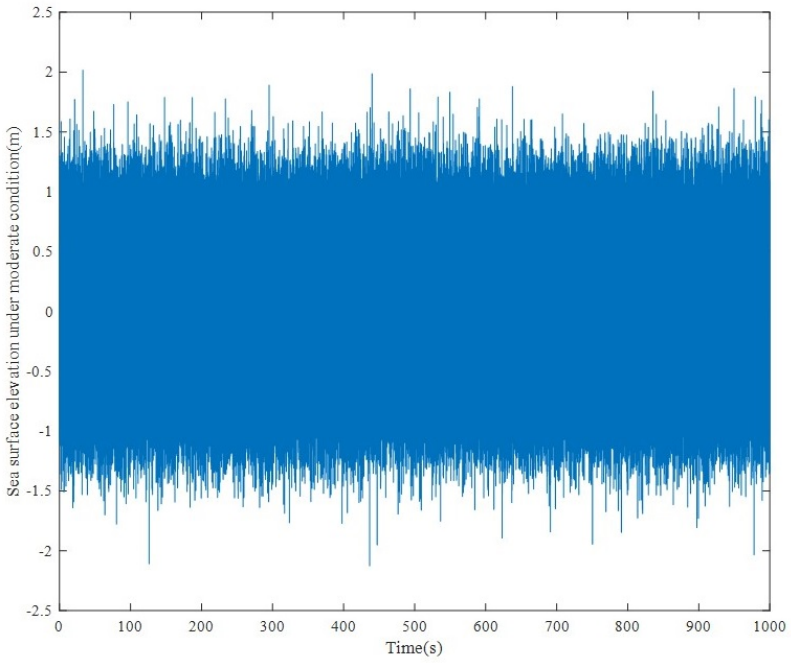

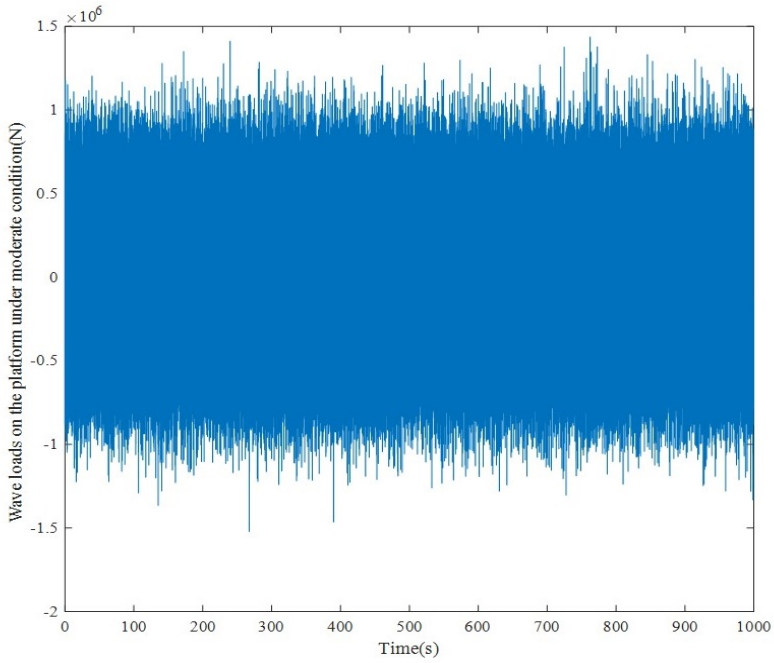

The time history of the random surface elevation of the sea and the loads on the platform under weak condition

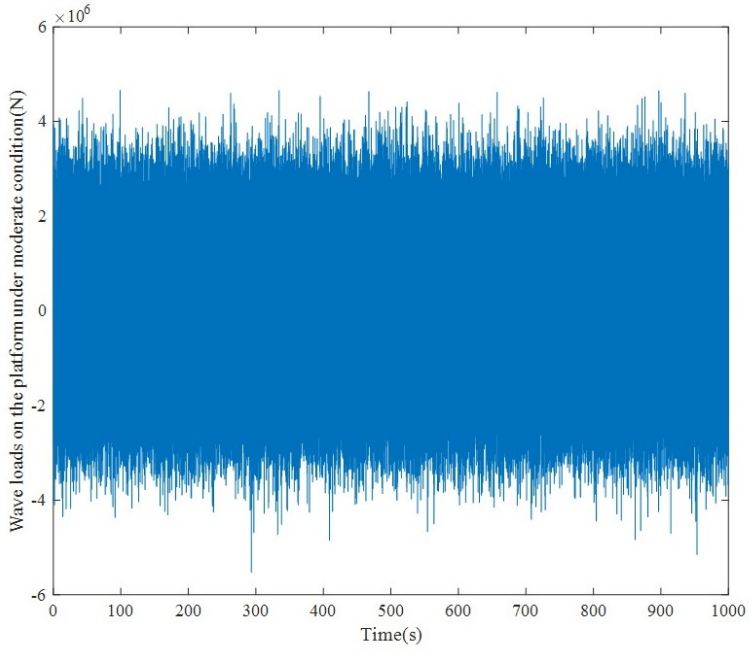

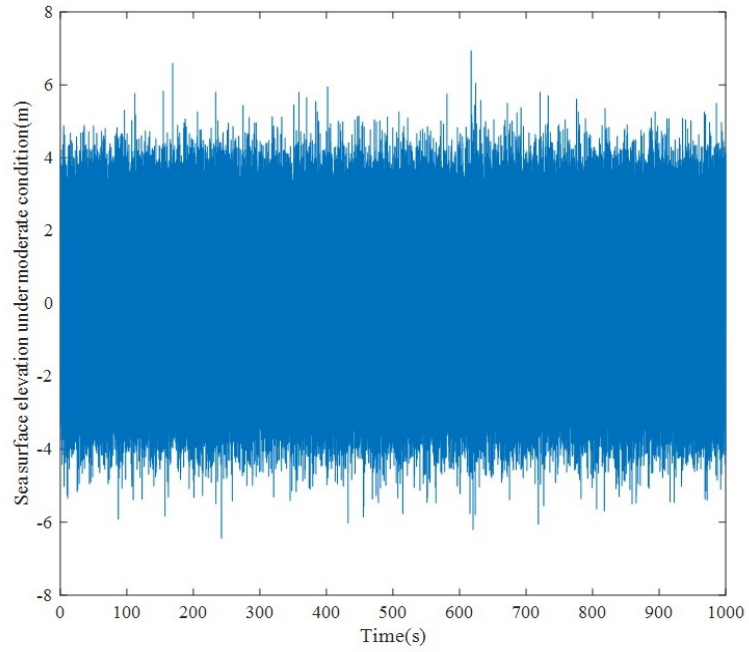

The time history of the random surface elevation of the sea and the loads on the platform under strong condition

9.2.2. The time-history of the nacelle's motion in the surge direction considered the wind-wave misalignment

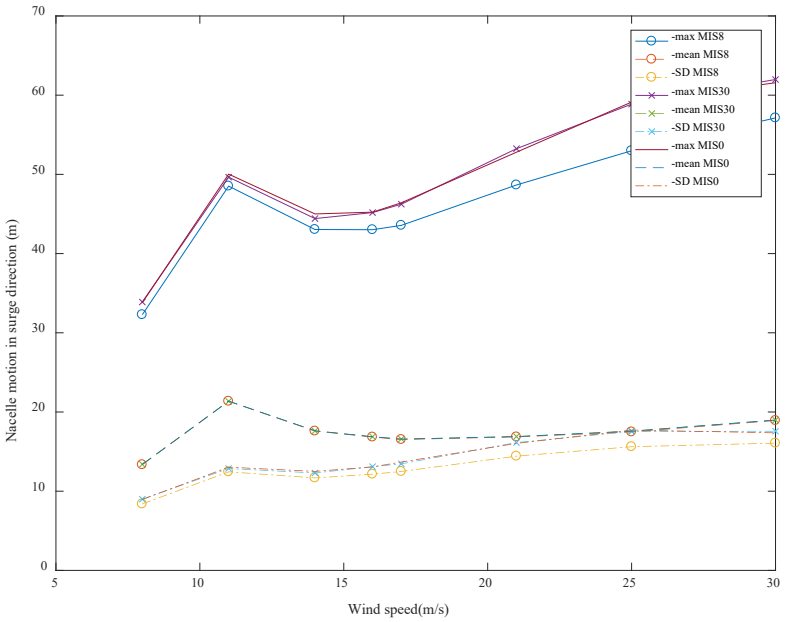

The nacelle's performances in the surge direction under with a wind and wave misalignment at 8deg

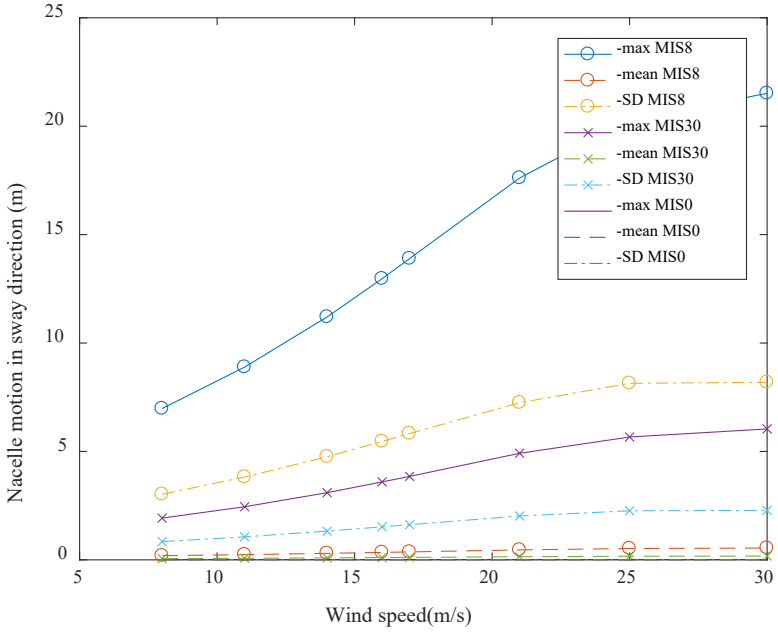

The nacelle's performances in the surge direction under with a wind and wave misalignment at 30deg

9.3. Additional eqations for Chapter 7

9.3.1. General solution of the 4th order differential equation

The equation of motion of the tower structure for wind turbine shown in Section 7.1 is

$$EI_{(z)}\frac{\partial^4 w_{(z,t)}}{\partial z^4} + N_{(z)}\frac{\partial^2 w_{(z,t)}}{\partial z^2} - m_{(z)}r_{(z)}{}^2\frac{\partial^2}{\partial z^2}\left(\frac{\partial^2 w_{(z,t)}}{\partial t^2}\right) + m_{(z)}\frac{\partial^2 w_{(z,t)}}{\partial t^2} = f_{(z,t)} \quad (9.1)$$

Assume harmonic oscillation with angular frequency ω so that

$$v_{(z,t)} = v_{(\xi,t)} = V_{(\xi)}e^{i\omega t} \quad (9.2)$$

where $V_{(\xi)}$ is the amplitude of the vibration and $\xi = {}^{z}/_{L}$

Substituting Eq.(9.2) into Eq.(9.1) gives,

$$\frac{\partial^4 V}{\partial \xi^4} + \alpha\frac{\partial^2 V}{\partial \xi^2} - \beta V_{(\xi)} = \gamma \quad (9.3)$$

where

$$\frac{NL^2}{EI} = \alpha$$
$$\frac{\omega^2 \rho A L^4}{EI} = \beta$$
$$\frac{PL^4}{EIe^{i\omega t}} = \gamma$$

The general solution of the above equation would have two parts, complementary function (CF) and the particular integral (PI). So $V_{(\xi)} = V_{CF} + V_{PI}$.

First, solve the corresponding homogeneous equation

$$r^4 + \alpha r^2 - \beta r = 0 \quad (9.4)$$

Thus the complementary solutions are

$$V_{CF} = C_1 e^{r_1 \xi} + C_2 e^{r_2 \xi} + C_3 e^{r_3 \xi} + C_4 e^{r_4 \xi} \quad (9.5)$$

where C_1, C_2, C_3 &C_4 are free parameters (arbitrary constants)

r_1, r_2, r_3 & r_4 are the four roots of the Eq. (9.4), $\pm\sqrt{\frac{-\alpha \pm \sqrt{\alpha^2+4\beta}}{2}}$

Assume that $r_1 = -r_3 = \sqrt{\frac{-\alpha+\sqrt{\alpha^2+4\beta}}{2}}$, $r_2 = -r_4 = \sqrt{\frac{-\alpha-\sqrt{\alpha^2+4\beta}}{2}}$and $r_1 \neq r_2$

For the PI, try $V_{PI} = C$,

$$V_{PI} = C = -\frac{\gamma}{\beta} \quad (9.6)$$

Thus the general solution of the vibration equation is

$$V_{(\xi)} = C_1 e^{r_1 \xi} + C_2 e^{r_2 \xi} + C_3 e^{r_3 \xi} + C_4 e^{r_4 \xi} - \frac{\gamma}{\beta} \quad (9.7)$$

9.3.2. The elements of the tower vibration matrix R

The elements of the matrix ***R*** are given by:

$$R_{11} = R_{13} = I_{01}\omega^2\lambda$$

$$R_{12} = -EI\lambda^2\left(1 - \frac{I_{01}\omega^2}{k_1}\right) + g_1M_1\omega^2\,cos(\theta_1)$$

$$R_{14} = EI\lambda^2\left(1 - \frac{I_{01}\omega^2}{k_1}\right) + g_1M_1\omega^2\,cos(\theta_1)$$

$$R_{21} = -EI\lambda^3 + mr^2\omega^2\lambda - g_1M_1\omega^2\lambda\,cos(\theta_1)$$

$$R_{22} = -M_1\omega^2 - g_1M_1\omega^2\,cos(\theta_1)\frac{EI\lambda^2}{k_1}$$

$$R_{23} = EI\lambda^3 + mr^2\omega^2\lambda - g_1M_1\omega^2\lambda\,cos(\theta_1)$$

$$R_{24} = -M_1\omega^2 + g_1M_1\omega^2\,cos(\theta_1)\frac{EI\lambda^2}{k_1}$$

$$R_{31} = -EI\lambda^2S - I_{02}\omega^2\lambda C + I_{02}\omega^2\frac{EI\lambda^2}{k_2}S - g_2M_2\omega^2\,cos(\theta_2)S$$

$$R_{32} = -EI\lambda^2C + I_{02}\omega^2\lambda S + I_{02}\omega^2\frac{EI\lambda^2}{k_2}C - g_2M_2\omega^2\,cos(\theta_2)C$$

$$R_{33} = EI\lambda^2SH - I_{02}\omega^2\lambda CH - I_{02}\omega^2\frac{EI\lambda^2}{k_2}SH - g_2M_2\omega^2\,cos(\theta_2)SH$$

$$R_{34} = EI\lambda^2CH - I_{02}\omega^2\lambda SH - I_{02}\omega^2\frac{EI\lambda^2}{k_2}CH - g_2M_2\omega^2\,cos(\theta_2)CH$$

$$R_{41} = -EI\lambda^3C + mr^2\omega^2\lambda C + M_2\omega^2S + g_2M_2\omega^2\,cos(\theta_2)(\lambda C - \frac{EI\lambda^2}{k_2}S)$$

$$R_{42} = EI\lambda^3S - mr^2\omega^2\lambda S + M_2\omega^2C - g_2M_2\omega^2\,cos(\theta_2)(\lambda S + \frac{EI\lambda^2}{k_2}C)$$

$$R_{43} = EI\lambda^3CH + mr^2\omega^2\lambda CH + M_2\omega^2SH + g_2M_2\omega^2\,cos(\theta_2)(\lambda CH + \frac{EI\lambda^2}{k_2}SH)$$

$$R_{44} = EI\lambda^3SH + mr^2\omega^2\lambda SH + M_2\omega^2CH + g_2M_2\omega^2\,cos(\theta_2)(\lambda SH + \frac{EI\lambda^2}{k_2}CH)$$

where $S = \sin(\lambda L)$, $C = cos(\lambda L)$, $SH = sinh(\lambda L)$, and $CH = cosh(\lambda L)$,

9.3.3. The calculation of the tower parameters

For the sake of brevity, the tower structure is considered as a uniform shell structure with constant thickness. The moment of inertia of the circular cross-section can be calculated by

$$I = \frac{\pi}{64}D^4 - \frac{\pi}{64}(D - 2t)^4$$

The mass density per unit length of the tower is given by $m = \rho A$, where $A = \frac{\pi}{4}D^2 - \frac{\pi}{4}(D - 2t)^2$.

The moment of inertia for the two mass components about the ends of the tower can be calculated by

$$I_{0i}^2 = I_i^2 + M_i^2 g_i^2 , \quad i = 1,2$$

where I_i is the moment of inertia of the component about its centre of gravity (CG), as listed in Table 7. The fixed angle and the distance between the CG of the nacelle and the top end of the tower structure can be calculated as

$$\theta_2 = \tan^{-1}\left(\frac{l_{oo'}}{h_{oo'}}\right)$$

$$g_2 = \sqrt{{l_{oo'}}^2 + {h_{oo'}}^2}$$

9.3.4. The elements of the non-uniform tower vibration matrix $R^{(i)}$

The elements of the matrix $\boldsymbol{R}^{(i)}$ are given by:

$$R_{11}^{(1)} = I_{01}\omega^2\lambda_1^{(1)}$$

$$R_{12}^{(1)} = -EI{\lambda_1^{(1)}}^2\left(1-\frac{I_{01}\omega^2}{k_1}\right)+g_1M_1\omega^2\,cos(\theta_1)$$

$$R_{13}^{(1)} = I_{01}\omega^2\lambda_2^{(1)}$$

$$R_{14}^{(1)} = EI{\lambda_2^{(1)}}^2\left(1-\frac{I_{01}\omega^2}{k_1}\right)+g_1M_1\omega^2\,cos(\theta_1)$$

$$R_{21}^{(1)} = -EI{\lambda_1^{(1)}}^3+mr^2\omega^2\lambda_1^{(1)}-g_1M_1\omega^2\lambda_1^{(1)}\,cos(\theta_1)$$

$$R_{22}^{(1)} = -M_1\omega^2-g_1M_1\omega^2\,cos(\theta_1)\frac{EI{\lambda_1^{(1)}}^2}{k_1}$$

$$R_{23}^{(1)} = EI{\lambda_2^{(1)}}^3+mr^2\omega^2\lambda_2^{(1)}-g_1M_1\omega^2\lambda_2^{(1)}\,cos(\theta_1)$$

$$R_{24}^{(1)} = -M_1\omega^2+g_1M_1\omega^2\,cos(\theta_1)\frac{EI{\lambda_2^{(1)}}^2}{k_1}$$

and

$$R_{31}^{(n)} = -EI{\lambda_1^{(n)}}^2\mathrm{S}^{(n)}-I_{02}\omega^2\lambda_1^{(n)}C^{(n)}+I_{02}\omega^2\frac{EI{\lambda_1^{(n)}}^2}{k_2}\mathrm{S}^{(n)}-g_2M_2\omega^2\,cos(\theta_2)\mathrm{S}^{(n)}$$

$$R_{32}^{(n)} = -EI{\lambda_1^{(n)}}^2C^{(n)}+I_{02}\omega^2\lambda_1^{(n)}\mathrm{S}^{(n)}+I_{02}\omega^2\frac{EI{\lambda_1^{(n)}}^2}{k_2}C^{(n)}-g_2M_2\omega^2\,cos(\theta_2)C^{(n)}$$

$$R_{33}^{(n)} = EI{\lambda_2^{(n)}}^2SH^{(n)}-I_{02}\omega^2\lambda_2^{(n)}CH^{(n)}-I_{02}\omega^2\frac{EI{\lambda_2^{(n)}}^2}{k_2}SH^{(n)}-g_2M_2\omega^2\,cos(\theta_2)SH^{(n)}$$

$$R_{34}^{(n)} = EI{\lambda_2^{(n)}}^2CH^{(n)}-I_{02}\omega^2\lambda_2^{(n)}SH^{(n)}-I_{02}\omega^2\frac{EI{\lambda_2^{(n)}}^2}{k_2}CH^{(n)}-g_2M_2\omega^2\,cos(\theta_2)CH^{(n)}$$

$$R_{41}^{(n)} = -EI{\lambda_1^{(n)}}^3C^{(n)}+mr^2\omega^2\lambda_1^{(n)}C^{(n)}+M_2\omega^2\mathrm{S}^{(n)}+g_2M_2\omega^2\,cos(\theta_2)(\lambda_1^{(n)}C^{(n)}-\frac{EI{\lambda_1^{(n)}}^2}{k_2}\mathrm{S}^{(n)})$$

$$R_{42}^{(n)} = EI{\lambda_1^{(n)}}^3\mathrm{S}^{(n)}-mr^2\omega^2\lambda_1^{(n)}\mathrm{S}^{(n)}+M_2\omega^2C^{(n)}-g_2M_2\omega^2\,cos(\theta_2)(\lambda_1^{(n)}\mathrm{S}^{(n)}+\frac{EI{\lambda_1^{(n)}}^2}{k_2}C^{(n)})$$

$$R_{43}^{(n)} = EI{\lambda_2^{(n)}}^3CH^{(n)}+mr^2\omega^2\lambda_2^{(n)}CH^{(n)}+M_2\omega^2SH^{(n)}+g_2M_2\omega^2\,cos(\theta_2)(\lambda_2^{(n)}CH^{(n)}+\frac{EI{\lambda_2^{(n)}}^2}{k_2}SH^{(n)})$$

$$R_{44}^{(n)} = EI{\lambda_2^{(n)}}^3SH^{(n)}+mr^2\omega^2\lambda_2^{(n)}SH^{(n)}+M_2\omega^2CH^{(n)}+g_2M_2\omega^2\,cos(\theta_2)\left(\lambda_2^{(n)}SH^{(n)}+\frac{EI{\lambda_2^{(n)}}^2}{k_2}CH^{(n)}\right)$$

and

$$\left.\begin{aligned} R_{11}^{(i)} &= EI{\lambda_1^{(i)}}^3 C^{(i)} - N\lambda_1^{(i)} C^{(i)} - mr^2\omega^2\lambda_1^{(i)} C^{(i)} \\ R_{12}^{(i)} &= -EI{\lambda_1^{(i)}}^3 \mathrm{S}^{(i)} + N\lambda_1^{(i)} \mathrm{S}^{(i)} + mr^2\omega^2\lambda_1^{(i)} \mathrm{S}^{(i)} \\ R_{13}^{(i)} &= -EI{\lambda_2^{(i)}}^3 CH^{(i)} - N\lambda_2^{(i)} CH^{(i)} - mr^2\omega^2\lambda_2^{(i)} CH^{(i)} \\ R_{14}^{(i)} &= -EI{\lambda_2^{(i)}}^3 SH^{(i)} - N\lambda_2^{(i)} SH^{(i)} - mr^2\omega^2\lambda_2^{(i)} SH^{(i)} \\ R_{21}^{(i)} &= EI{\lambda_1^{(i)}}^2 \mathrm{S}^{(i)} \\ R_{22}^{(i)} &= EI{\lambda_1^{(i)}}^2 C^{(i)} \\ R_{23}^{(i)} &= -EI{\lambda_2^{(i)}}^2 SH^{(i)} \\ R_{24}^{(i)} &= -EI{\lambda_2^{(i)}}^2 CH^{(i)} \end{aligned}\right\} for\ i = 2, \cdots, n$$

and

$$\left.\begin{aligned} R_{31}^{(i)} &= -EI{\lambda_1^{(i)}}^3 + N\lambda_1^{(i)} + mr^2\omega^2\lambda_1^{(i)} \\ R_{32}^{(i)} &= R_{34}^{(i)} = R_{41}^{(i)} = R_{43}^{(i)} = 0 \\ R_{33}^{(i)} &= EI{\lambda_2^{(i)}}^3 + N\lambda_2^{(i)} + mr^2\omega^2\lambda_2^{(i)} \\ R_{42}^{(i)} &= -EI{\lambda_1^{(i)}}^2 \\ R_{44}^{(i)} &= EI{\lambda_2^{(i)}}^2 \end{aligned}\right\} for\ i = 1, \cdots, n-1$$

where $\mathrm{S}^{(i)} = \sin(\lambda_1^{(i)}\Delta h)$, $C^{(i)} = cos\left(\lambda_1^{(i)}\Delta h\right)$, $SH^{(i)} = sinh\left(\lambda_2^{(i)}\Delta h\right)$

and $CH^{(i)} = cosh(\lambda_2^{(i)}\Delta h)$.

References

[1] Yang W, Tavner PJ, Crabtree CJ, Wilkinson M. Cost-effective condition monitoring for wind turbines. IEEE Transactions on Industrial Electronics. 2010;57:263-71.

[2] Senjyu T, Ochi Y, Kikunaga Y, Tokudome M, Yona A, Muhando EB et al. Sensor-less maximum power point tracking control for wind generation system with squirrel cage induction generator. Renewable Energy. 2009;34:994-9.

[3] Polinder H, Van der Pijl FF, De Vilder G-J, Tavner PJ. Comparison of direct-drive and geared generator concepts for wind turbines. IEEE Transactions on Energy Conversion. 2006;21:725-33.

[4] Polinder H, de Haan SW, Dubois MR, Slootweg JG. Basic operation principles and electrical conversion systems of wind turbines. EPE JOURNAL. 2005;15:43.

[5] Slootweg H, De Vries E. Inside wind turbines-Fixed vs. variable speed. Renewable Energy World. 2003;6:30-41.

[6] Spooner E, Chalmers B. 'TORUS': a slotless, toroidal-stator, permanent-magnet generator. IEE Proceedings B (Electric Power Applications): IET; 1992. p. 497-506.

[7] Chalmers B, Spooner E. An axial-flux permanent-magnet generator for a gearless wind energy system. Energy Conversion, IEEE Transactions on. 1999;14:251-7.

[8] Yang W. Condition monitoring the drive train of a direct drive permanent magnet wind yurbine using generator electrical signals. Journal of Solar Energy Engineering-The Transactions of ASME. 2014;136:021008.

[9] Sethuraman L, Xing Y, Gao Z, Venugopal V, Mueller M, Moan T. A 5MW direct-drive generator for floating spar-buoy wind turbine: Development and analysis of a fully coupled Mechanical model. Proceedings of the Institution of Mechanical Engineers, Part A: Journal of Power and Energy. 2014;228:718-41.

[10] Muljadi E, Butterfield CP, Wan Y-h. Axial-flux modular permanent-magnet generator with a toroidal winding for wind-turbine applications. IEEE Transactions on Industry Applications. 1999;35:831-6.

[11] Milborrow D. Wind energy: a technology that is still evolving. Proceedings of the institution of mechanical engineers, part a: Journal of power and energy. 2011;225:539-47.

[12] Walford CA. Wind turbine reliability: understanding and minimizing wind turbine operation and maintenance costs. Sandia National Laboratories, SAND2006-1100; March 2006.

[13] Wilkinson M, Spianto F, Knowles M. Towards the zero maintenance wind turbine. Universities Power Engineering Conference, 2006 UPEC'06 Proceedings of the 41st International, Newcastle-upon-Tyne, UK: IEEE; 6-8 Sept. 2006. p. 74-8.

[14] McMillan D, Ault GW. Quantification of condition monitoring benefit for offshore wind turbines. Wind Engineering. 2007;31:267-85.

[15] Dai K, Bergot A, Liang C, Xiang W-N, Huang Z. Environmental issues associated with wind energy–A review. Renewable Energy. 2015;75:911-21.

[16] Dezvareh R, Bargi K, Mousavi SA. Control of wind/wave-induced vibrations of jacket-type offshore wind turbines through tuned liquid column gas dampers. Structure and Infrastructure Engineering. 2016;12:312-26.

[17] Muliawan MJ, Karimirad M, Moan T. Dynamic response and power performance of a combined spar-type floating wind turbine and coaxial floating wave energy converter. Renewable Energy. 2013;50:47-57.

[18] Ramachandran GKV, Bredmose H, Sørensen JN, Jensen JJ. Fully coupled three-dimensional dynamic response of a tension-leg platform floating wind turbine in waves and wind. Journal of Offshore Mechanics and Arctic Engineering. 2014;136:020901.

[19] Karimirad M, Moan T. Wave-and wind-induced dynamic response of a spar-type offshore wind turbine. Journal of Waterway, Port, Coastal, and Ocean Engineering. 2011;138:9-20.

[20] Basu B, Zhang Z, Nielsen SR. Damping of edgewise vibration in wind turbine blades by means of circular liquid dampers. Wind Energy. 2016;19:213-26.

[21] Qiao W, Lu D. A survey on wind turbine condition monitoring and fault diagnosis—Part I: Components and subsystems. IEEE Transactions on Industrial Electronics. 2015;62:6536-45.

[22] Bazeos N, Hatzigeorgiou G, Hondros I, Karamaneas H, Karabalis D, Beskos D. Static, seismic and stability analyses of a prototype wind turbine steel tower. Engineering Structures. 2002;24:1015-25.

[23] Lavassas I, Nikolaidis G, Zervas P, Efthimiou E, Doudoumis I, Baniotopoulos C. Analysis and design of the prototype of a steel 1-MW wind turbine tower. Engineering Structures. 2003;25:1097-106.

[24] Naguleswaran S. Lateral vibration of a centrifugally tensioned uniform Euler-Bernoulli beam. Journal of Sound and Vibration. 1994;176:613-24.

[25] Banerjee J. Free vibration of centrifugally stiffened uniform and tapered beams using the dynamic stiffness method. Journal of Sound and Vibration. 2000;233:857-75.

[26] Lee C, Al-Salem M, Woehrle T. Natural frequency measurements for rotating spanwise uniform cantilever beams. Journal of Sound and Vibration. 2001;240:957-61.

[27] Baumgart A. A mathematical model for wind turbine blades. Journal of sound and Vibration. 2002;251:1-12.

[28] Chung J, Yoo HH. Dynamic analysis of a rotating cantilever beam by using the finite element method. Journal of Sound and Vibration. 2002;249:147-64.

[29] Harrison R, Hau E, Snel H. Large wind turbines: design and economics. Chichester, UK: John Wiley & Sons; 2000.

[30] Murtagh P, Basu B, Broderick B. Along-wind response of a wind turbine tower with blade coupling subjected to rotationally sampled wind loading. Engineering Structures. 2005;27:1209-19.

[31] Dubois M, Polinder H, Ferreira J. Comparison of generator topologies for direct-drive wind turbines. Proceedings of IEEE Nordic Workshop on Power and Industrial Electronics (Norpie 2000), Aalborg, Denmark2000. p. 22-6.

[32] Quinonez-Varela G, Cruden A. Modelling and validation of a squirrel cage induction generator wind turbine during connection to the local grid. Generation, Transmission & Distribution, IET. 2008;2:301-9.

[33] Goel PK, Singh B, Murthy SS, Kishore N. Isolated wind–hydro hybrid system using cage generators and battery storage. IEEE Transactions on Industrial Electronics. 2011;58:1141-53.

[34] Domínguez-García JL, Gomis-Bellmunt O, Trilla-Romero L, Junyent-Ferré A. Indirect vector control of a squirrel cage induction generator wind turbine. Computers & Mathematics with Applications. 2012;64:102-14.

[35] Chen H, Aliprantis DC. Analysis of squirrel-cage induction generator with Vienna rectifier for wind energy conversion system. Energy Conversion, IEEE Transactions on. 2011;26:967-75.

[36] Akhmatova V, Nielsenb AH, Pedersenc JK, Nymannc O. Variable-speed wind turbines with multi-pole synchronous permanent magnet generators. Part I: Modelling in dynamic simulation tools. Wind Engineering. 2003;27:531-48.

[37] Burton T, Sharpe D, Jenkins N, Bossanyi E. Wind energy handbook. Chichester, UK: John Wiley & Sons; 2001.

[38] Lampola P. Directly driven, low-speed permanent-magnet generators for wind power applications. Acta Polytechnica Scandinavica, Electrical Engineering Series, No.101, Espoo: Finnish Academies of Technology; 2000.

[39] Cavagnino A, Lazzari M, Profumo F, Tenconi A. A comparison between the axial flux and the radial flux structures for PM synchronous motors. Industry Applications Conference, 2001 Thirty-Sixth IAS Annual Meeting Conference Record of the 2001 IEEE: IEEE; 2001. p. 1611-8.

[40] Grauers A. Design of direct-driven permanent-magnet generators for wind turbines: School of Electrical and Computer Engineering, Chalmers University of Technology; 1996.

[41] Weh H. Transverse flux (TF) machines in drive and generator application. IEEE Power Tech International Symposium on Electric Power Engineering1995. p. 75-80.

[42] Bang D, Polinder H, Shrestha G, Ferreira JA. Review of generator systems for direct-drive wind turbines. European Wind Energy Conference & Exhibition, Belgium2008. p. 1-11.

[43] Leban K, Ritchie E, Argeseanu A. Design preliminaries for direct drive under water wind turbine generator. Electrical Machines (ICEM), 2012 XXth International Conference on: IEEE; 2012. p. 190-5.

[44] Spooner E, Williamson A. Direct coupled, permanent magnet generators for wind turbine applications. IEE Proceedings-Electric Power Applications. 1996;143:1-8.

[45] Hansen LH, Helle L, Blaabjerg F, Ritchie E, Munk-Nielsen S, Bindner HW et al. Conceptual survey of generators and power electronics for wind turbines. Denmark: Forskningscenter Risoe. Risoe-R No. 1205(EN); 2002.

[46] Sethuraman L, Venugopal V, Mueller M. Drive-train configurations for Floating wind turbines. Ecological Vehicles and Renewable Energies (EVER), 2013 8th International Conference and Exhibition on: IEEE; 2013. p. 1-7.

[47] Caricchi F, Crescimbini F, Mezzetti F, Santini E. Multistage axial-flux PM machine for wheel direct drive. IEEE Transactions on Industry Applications. 1996;32:882-8.

[48] Shrestha G, Polinder H, Bang D-J, Ferreira JA. Structural flexibility: A solution for weight reduction of large direct-drive wind-turbine generators. IEEE Transactions on Energy Conversion. 2010;25:732-40.

[49] Paulsen US, Vita L, Madsen HA, Hattel J, Ritchie E, Leban KM et al. 1 st DeepWind 5 MW Baseline design. Energy Procedia. 2012;24:27-35.

[50] Borgen E. Introduction of the sway turbine ST10. IQPC 3rd international conference drivetrain concepts for wind turbines. Swissôtel Bremen, Germany,22-24 October 2012.

[51] Kirschneck M, Polinder H, Van Ostayen R, Van Kempen F, Rixen D. Structural dynamic topology optimisation of a direct-drive single bearing wind turbine generator. WCSMO-11: Proceedings of the 11th World Congress on Structural and Multidisciplinary Optimization, Sydney, Australia: ISSMO; 7-12 June 2015.

[52] Stander J, Venter G, Kamper M. Structural mass reduction by integrating active material in direct drive generator design. Structural and Multidisciplinary Optimization. 2015;52:405-16.

[53] Chew K-H, Tai K, Ng E, Muskulus M. Optimization of offshore wind turbine support structures using an analytical gradient-based method. Energy Procedia. 2015;80:100-7.

[54] Kalsi SS, Weeber K, Takesue H, Lewis C, Neumueller H-W, Blaugher RD. Development status of rotating machines employing superconducting field windings. Proceedings of the IEEE. 2004;92:1688-704.

[55] Lewis C, Muller J. A direct drive wind turbine HTS generator. Power Engineering Society General Meeting, 2007 IEEE: IEEE; 2007. p. 1-8.

[56] Quddes M, Sekino M, Ohsaki H, Kashima N, Nagaya S. Electromagnetic design study of transverse flux enhanced type superconducting wind turbine generators. Applied Superconductivity, IEEE Transactions on. 2011;21:1101-4.

[57] Keysan O, Mueller MA. A homopolar HTSG topology for large direct-drive wind turbines. Applied Superconductivity, IEEE Transactions on. 2011;21:3523-31.

[58] Abrahamsen AB, Mijatovic N, Seiler E, Zirngibl T, Træholt C, Nørgård PB et al. Superconducting wind turbine generators. Superconductor Science and Technology. 2010;23:034019.

[59] Lesser M, Muller J. Superconductor technology generating the future of offshore wind power'. Renewable Energy World Conf, Cologne, Germany2009. p. 1-10.

[60] Wang J, Qu R, Tang Y, Liu Y, Zhang B, He J et al. Design of a superconducting synchronous generator with LTS field windings for 12 MW offshore direct-drive wind turbines. IEEE Transactions on Industrial Electronics. 2016;63:1618-28.

[61] Arand SJ, Ardebili M. Multi-objective design and prototyping of a low cogging torque axial-flux PM generator with segmented stator for small-scale direct-drive wind turbines. IET Electric Power Applications. 2016;10:889-99.

[62] Lu B, Li Y, Wu X, Yang Z. A review of recent advances in wind turbine condition monitoring and fault diagnosis. Power Electronics and Machines in Wind Applications, 2009 PEMWA 2009 IEEE: IEEE; 2009. p. 1-7.

[63] Kazemtabrizi B, Hogg S. A New Simulation and Control Model for a Variable Speed Variable Pitch Direct Drive Large Offshore Wind Turbine Generator With Integrated Energy Storage. ASME Turbo Expo 2014: Turbine Technical Conference and Exposition. Düsseldorf, Germany: American Society of Mechanical Engineers; June 16 – 20, 2014. p. V03BT46A013-V03BT46A.

[64] Novotny DW, Lipo TA. Vector control and dynamics of AC drives: Clarendon Press Oxford; 1996.

[65] Strachan NP, Jovcic D. Dynamic modelling, simulation and analysis of an offshore variable-speed directly-driven permanent-magnet wind energy conversion and storage system (WECSS). OCEANS 2007-Europe: IEEE; 2007. p. 1-6.

[66] Zhang K, Duan Y, Wu J, Qiu J, Lu J, Fan S et al. Low voltage ride through control strategy of directly driven wind turbine with energy storage system. Power and Energy Society General Meeting, 2011 IEEE: IEEE; 2011. p. 1-7.

[67] Gong X, Qiao W. Current-based mechanical fault detection for direct-drive wind turbines via synchronous sampling and impulse detection. IEEE Transactions on Industrial Electronics. 2015;62:1693-702.

[68] Qiao W, Lu D. A survey on wind turbine condition monitoring and fault diagnosis—Part II: Signals and signal processing methods. IEEE Transactions on Industrial Electronics. 2015;62:6546-57.

[69] Chowdhury MM, Haque ME, Das D, Gargoom A, Negnevitsky M. Modeling, parameter measurement and sensorless speed estimation of IPM synchronous generator for direct drive variable speed wind turbine application. International Transactions on Electrical Energy Systems. 2015;25:1814-30.

[70] Nerg J, Rilla M, Pyrhonen J. Thermal analysis of radial-flux electrical machines with a high power density. IEEE Transactions on Industrial Electronics. 2008;55:3543-54.

[71] Alexandrova Y, Semken RS, Pyrhönen J. Permanent magnet synchronous generator design solution for large direct-drive wind turbines: Thermal behavior of the LC DD-PMSG. Applied Thermal Engineering. 2014;65:554-63.

[72] Buhagiar D, Sant T. Steady-state analysis of a conceptual offshore wind turbine driven electricity and thermocline energy extraction plant. Renewable Energy. 2014;68:853-67.

[73] Slemon GR. On the design of high-performance surface-mounted PM motors. IEEE Transactions on Industry Applications. 1994;30:134-40.

[74] Nerg J, Ruuskanen V. Lumped-parameter-based thermal analysis of a doubly radial forced-air-cooled direct-driven permanent magnet wind generator. Mathematics and Computers in Simulation. 2013;90:218-29.

[75] Negm HM, Maalawi KY. Structural design optimization of wind turbine towers. Computers & Structures. 2000;74:649-66.

[76] Jonkman JM. Dynamics modeling and loads analysis of an offshore floating wind turbine: NERLTechnical Report, NREL/TP-500-41958 , November 2007

[77] Nikitas G, Vimalan NJ, Bhattacharya S. An innovative cyclic loading device to study long term performance of offshore wind turbines. Soil Dynamics and Earthquake Engineering. 2016;82:154-60.

[78] Carroll J, McDonald A, McMillan D. Failure rate, repair time and unscheduled O&M cost analysis of offshore wind turbines. Wind Energy. 2016;19:1107-19.

[79] Perez-Collazo C, Greaves D, Iglesias G. A review of combined wave and offshore wind energy. Renewable and Sustainable Energy Reviews. 2015;42:141-53.

[80] Ho A, Mbistrova A. The European offshore wind industry-key trends and statistics 1st half 2015. available at :https://www.ewea.org/ (accessed in September 2017): A report by the European Wind Energy Association-2015.

[81] Kallehave D, Byrne BW, Thilsted CL, Mikkelsen KK. Optimization of monopiles for offshore wind turbines. Phil Trans R Soc A. 2015;373:20140100.

[82] Musial W, Butterfield S, Boone A. Feasibility of floating platform systems for wind turbines. 23rd ASME Wind Energy Symposium, Reno, NV2004.

[83] Pecher A, Foglia A, Kofoed JP. Comparison and sensitivity investigations of a CALM and SALM type mooring system for wave energy converters. Journal of Marine Science and Engineering. 2014;2:93-122.

[84] Guo Z, Wang L, Yuan F. Quasi-Static Analysis of the Multicomponent Mooring Line for Deeply Embedded Anchors. Journal of Offshore Mechanics and Arctic Engineering. 2016;138:011302.

[85] Henderson AR, Zaaijer M, Bulder B, Pierik J, Huijsmans R, van Hees M et al. Floating windfarms for shallow offshore sites. The Fourteenth International Offshore and Polar Engineering Conference. Toulon, France: International Society of Offshore and Polar Engineers; 23-28 May 2004.

[86] Butterfield CP, Musial W, Jonkman J, Sclavounos P, Wayman L. Engineering challenges for floating offshore wind turbines. 2005 Copenhagen Offshore Wind Conference Copenhagen. Denmark, October 26–28, 2005.

[87] Karimirad M, Moan T. Extreme dynamic structural response analysis of catenary moored spar wind turbine in harsh environmental conditions. Journal of Offshore Mechanics and Arctic Engineering. 2011;133:041103.

[88] Sethuraman L, Xing Y, Venugopal V, Gao Z, Mueller M, Moan T. A 5 MW direct-drive generator for floating spar-buoy wind turbine: Drive-train dynamics. Proceedings

of the Institution of Mechanical Engineers, Part C: Journal of Mechanical Engineering Science. 2017;231:744-63.

[89] Snyder B, Kaiser MJ. Ecological and economic cost-benefit analysis of offshore wind energy. Renewable Energy. 2009;34:1567-78.

[90] Laura C-S, Vicente D-C. Life-cycle cost analysis of floating offshore wind farms. Renewable Energy. 2014;66:41-8.

[91] Kaldellis J, Apostolou D, Kapsali M, Kondili E. Environmental and social footprint of offshore wind energy. Comparison with onshore counterpart. Renewable Energy. 2016;92:543-56.

[92] Jover Rodríguez PV, Belahcen A, Arkkio A, Laiho A, Antonino-Daviu JA. Air-gap force distribution and vibration pattern of Induction motors under dynamic eccentricity. Electrical Engineering. 2007;90:209-18.

[93] Jang S-M, Lee S-H, Cho H-W, Cho S-K. Analysis of unbalanced force for high-speed slotless permanent magnet machine with Halbach array. IEEE Transactions on Magnetics. 2003;39:3265-7.

[94] Gustavsson RK, Aidanpää J-O. The influence of nonlinear magnetic pull on hydropower generator rotors. Journal of Sound and Vibration. 2006;297:551-62.

[95] Bang D, Polinder H, Ferreira J, Van Rooij RPJOM. New active speed stall control compared to pitch control for a direct-drive wind turbine. EWEC 2007 Conference Proceedings. Milan,Italy: EWEA European Wind Energy Association; May 7-10, 2007.

[96] Guo D, Chu F, Chen D. The Unbalanced Magnetic Pull and Its Effects on Vibration in a Three-Phase Generator with Eccentric Rotor. Journal of Sound and Vibration. 2002;254:297-312.

[97] Bywaters G, Mattila P, Costin D, Stowell J, John V, Hoskins S et al. Northern power NW 1500 direct-drive generator. Northern Power Systems Inc, Waitsfield, VT,

National Renewable Energy Laboratory, Subcontract Report NREL/SR-500-401772007.

[98] Sethuraman L, Venugopal V, Zavvos A, Mueller M. Structural integrity of a direct-drive generator for a floating wind turbine. Renewable Energy. 2014;63:597-616.

[99] McDonald A, Mueller M, Polinder H. Structural mass in direct-drive permanent magnet electrical generators. IET Renewable Power Generation. 2008;2:3-15.

[100] Binns K, Dye M. Identification of principal factors causing unbalanced magnetic pull in cage induction motors. Proceedings of the Institution of Electrical Engineers: IET; 1973. p. 349-54.

[101] Summers EW. Vibration in 2-pole induction motors related to slip frequency. Transactions of the American Institute of Electrical Engineers Part III: Power Apparatus and Systems. 1955;74:69-72.

[102] Von Kaehne P. Unbalanced Magnetic Pull in Rotating Electric Machines: ERA Technology Limited; 1963.

[103] Belmans R, Geysen W, Jordan H, Vandenput A. Unbalanced magnetic pull in three phase two pole induction motors with eccentric rotor. Proceedings of IEE-International Conference on Electrical Machines-Design and Applications1982. p. 65-9.

[104] Belmans R, Geysen W, Jordan H, Vandenput A. Unbalanced magnetic pull and homopolar flux in three phase induction motors with eccentric rotors. Proceedings of International Conference on Electrical Machines1982. p. 916-21.

[105] Smith A, Dorrell D. Calculation and measurement of unbalanced magnetic pull in cage induction motors with eccentric rotors. Part 1: Analytical model. IEE Proceedings-Electric Power Applications. 1996;143:193-201.

[106] DeBortoli M, Salon S, Burow D, Slavik C. Effects of rotor eccentricity and parallel windings on induction machine behavior: A study using finite element analysis. IEEE Transactions on Magnetics. 1993;29:1676-82.

[107] Salon S, DeBortoli M, Burow D, Slavik C. Calculation of circulating current between parallel windings in induction motors with eccentric rotors by the finite element method. Proceedings of ICEM'92. 1992:371-5.

[108] Wagner R, Courtney M, Gottschall J, Lindelöw-Marsden P. Accounting for the speed shear in wind turbine power performance measurement. Wind Energy. 2011;14:993-1004.

[109] White DL. New method for dual-axis fatigue testing of large wind turbine blades using resonance excitation and spectral loading: National Renewable Energy Laboratory,Technical Report, NREL/TP-500-35268 2004.

[110] Colwell S, Basu B. Tuned liquid column dampers in offshore wind turbines for structural control. Engineering Structures. 2009;31:358-68.

[111] Chandrasekaran S, Jain A. Triangular configuration tension leg platform behaviour under random sea wave loads. Ocean Engineering. 2002;29:1895-928.

[112] Massel SR. Ocean surface waves: their physics and prediction: Vol. 36. World scientific; 2013.

[113] Hasselmann K, Barnett T, Bouws E, Carlson H, Cartwright D, Enke K et al. Measurements of wind-wave growth and swell decay during the Joint North Sea Wave Project (JONSWAP). Ergänzungsheft 8-12. 1973.

[114] Johannessen K, Meling TS, Hayer S. Joint distribution for wind and waves in the northern north sea. The Eleventh International Offshore and Polar Engineering Conference. Stavanger, Norway: International Society of Offshore and Polar Engineers; 17-22 June 2001.

[115] Nie D, Jiang W, Li N. Numerical study of microwave backscattering from time-evolving JONSWAP-type mixed ocean waves. Remote Sensing Letters. 2017;8:1034-41.

[116] Molander M, Garcia-Gabin W. Evaluation of wave resistances estimated using wave spectra and a ship model. Control and Automation (MED), 2017 25th Mediterranean Conference on: IEEE; 2017. p. 322-7.

[117] Torsethaugen K. A two peak wave spectrum model. 12th Intl Conf on Offshore Mechanics & Arctic Engng. Glasgow, UK: ASME; 20-24 June 1993.

[118] Uys P, Farkas J, Jarmai K, Van Tonder F. Optimisation of a steel tower for a wind turbine structure. Engineering Structures. 2007;29:1337-42.

[119] Adhikari S, Bhattacharya S. Dynamic analysis of wind turbine towers on flexible foundations. Shock and Vibration. 2012;19:37-56.

[120] Jonkman J, Matha D. Dynamics of offshore floating wind turbines—analysis of three concepts. Wind Energy. 2011;14:557-69.

[121] Robertson AN, Jonkman JM. Loads analysis of several offshore floating wind turbine concepts. The Twenty-first International Offshore and Polar Engineering Conference. Maui, Hawaii, USA: International Society of Offshore and Polar Engineers; 19-24 June,2011.

[122] Si Y, Karimi HR, Gao H. Modelling and optimization of a passive structural control design for a spar-type floating wind turbine. Engineering Structures. 2014;69:168-82.

[123] Lackner MA, Rotea MA. Passive structural control of offshore wind turbines. Wind energy. 2011;14:373-88.

[124] Lackner MA, Rotea MA. Structural control of floating wind turbines. Mechatronics. 2011;21:704-19.

[125] Byrne B, McAdam R, Burd H, Houlsby G, Martin C, Zdravković L et al. New design methods for large diameter piles under lateral loading for offshore wind applications. 3rd International Symposium on Frontiers in Offshore Geotechnics (ISFOG 2015), Oslo, Norway, June2015. p. 10-2.

[126] Prendergast LJ, Gavin K, Doherty P. An investigation into the effect of scour on the natural frequency of an offshore wind turbine. Ocean Engineering. 2015;101:1-11.

[127] WindEnergie G. Overall damping for piled offshore support structures, guideline for the certification of offshore wind turbines. Germanischer Lloyd WindEnergie. 2005.

[128] Carswell W, Johansson J, Løvholt F, Arwade S, Madshus C, DeGroot D et al. Foundation damping and the dynamics of offshore wind turbine monopiles. Renewable Energy. 2015;80:724-36.

[129] Morató A, Sriramula S, Krishnan N, Nichols J. Ultimate loads and response analysis of a monopile supported offshore wind turbine using fully coupled simulation. Renewable Energy. 2017;101:126-43.

[130] Wang W, Gao Z, Li X, Moan T. Model Test and Numerical Analysis of a Multi-Pile Offshore Wind Turbine Under Seismic, Wind, Wave, and Current Loads. Journal of Offshore Mechanics and Arctic Engineering. 2017;139:031901.

[131] Larsen TJ, Hanson TD. A method to avoid negative damped low frequent tower vibrations for a floating, pitch controlled wind turbine. Journal of Physics: Conference Series: IOP Publishing; 2007. p. 012073.

[132] Zhang Z, Nielsen SR, Blaabjerg F, Zhou D. Dynamics and control of lateral tower vibrations in offshore wind turbines by means of active generator torque. Energies. 2014;7:7746-72.

[133] Arany L, Bhattacharya S, Macdonald JH, Hogan SJ. Closed form solution of Eigen frequency of monopile supported offshore wind turbines in deeper waters

incorporating stiffness of substructure and SSI. Soil Dynamics and Earthquake Engineering. 2016;83:18-32.

[134] Sopanen J, Ruuskanen V, Nerg J, Pyrhonen J. Dynamic torque analysis of a wind turbine drive train including a direct-driven permanent-magnet generator. IEEE Transactions on Industrial Electronics. 2011;58:3859-67.

[135] Pyrhönen J, Kurronen P, Parviainen A. Permanent magnet 3 MW low-speed generator development. Proc of ICEM. Crete, Greece2006.

[136] Heikkinen JE, Sopanen JT, Ruuskanen VV, Nerg JK. Dynamic Analysis of a Direct-Driven Permanent Magnet Generator Drive Train Including Flexible Turbine Blades. ASME 2011 International Design Engineering Technical Conferences and Computers and Information in Engineering Conference. Washington, DC, USA: American Society of Mechanical Engineers; August 28-31 2011. p. 921-31.

[137] Ruzzo C, Failla G, Collu M, Nava V, Fiamma V, Arena F. Operational Modal Analysis of a Spar-Type Floating Platform Using Frequency Domain Decomposition Method. Energies. 2016;9:870.

[138] Bae Y, Kim M. Turbine-floater-tether coupled dynamic analysis including second-order sumfrequency wave loads for a TLP-type FOWT (floating offshore wind turbine). Proceedings of the ASME 2013 32nd International Conference on Ocean, Offshore and Arctic Engineering, no OMAE2013-11261. Nantes, France June 9-14, 2013.

[139] Struggl S, Berbyuk V, Johansson H. Review on wind turbines with focus on drive train system dynamics. Wind Energy. 2015;18:567-90.

[140] Robertson AN, Jonkman JM. Loads analysis of several offshore floating wind turbine concepts: National Renewable Energy Laboratory, US Department of Energy, Office of Energy Efficiency and Renewable Energy; 2011.

[141] Skaare B, Hanson TD, Nielsen FG, Yttervik R, Hansen AM, Thomsen K et al. Integrated dynamic analysis of floating offshore wind turbines. 2007 European Wind Energy Conference and Exhibition2007.

[142] Utsunomiya T, Matsukuma H, Minoura S, Ko K, Hamamura H, Kobayashi O et al. At sea experiment of a hybrid spar for floating offshore wind turbine using 1/10-scale model. Journal of Offshore Mechanics and Arctic Engineering-The Transactions of ASME. 2013;135:034503.

[143] Zavvos A, McDonald A, Mueller M. Structural optimisation tools for iron cored permanent magnet generators for large direct drive wind turbines. Renewable Power Generation (RPG 2011), IET Conference on: IET; 2011. p. 1-6.

[144] Jonkman JM. Definition of the floating system for phase IV of OC3: National Renewable Energy Laboratory Golden, CO, USA, Technical Report, NREL/TP-500-47535; May 2010.

[145] Teng W, Jiang R, Ding X, Liu Y, Ma Z. Detection and Quantization of Bearing Fault in Direct Drive Wind Turbine via Comparative Analysis. Shock and Vibration. 2016;2016.

[146] Pezzani CM, Bossio JM, Castellino AM, Bossio GR, De Angelo CH. A PLL-based resampling technique for vibration analysis in variable-speed wind turbines with PMSG: A bearing fault case. Mechanical Systems and Signal Processing. 2017;85:354-66.

[147] Sadarangani C. Electrical machines: Design and Analysis of induction and permanent magnet motors: Division of Electrical Machines and Power Electronics, School of Electrical Engineering, Royal Inst. of Technology; 2006.

[148] Zarko D, Ban D, Vazdar I, Jarica V. Calculation of unbalanced magnetic pull in a salient-pole synchronous generator using finite-element method and measured shaft orbit. IEEE Transactions on Industrial Electronics. 2012;59:2536-49.

[149] Petrinić M, Tvorić S, Car S. The effects of pole number and rotor wedge design on unbalanced magnetic pull of the synchronous generator. Electrical Machines (ICEM), 2014 International Conference on: IEEE; 2014. p. 316-22.

[150] Wang T, Coton FN. A high resolution tower shadow model for downwind wind turbines. Journal of Wind Engineering and Industrial Aerodynamics. 2001;89:873-92.

[151] Munduate X, Coton FN, Galbraith RAM. An investigation of the aerodynamic response of a wind turbine blade to tower shadow. Journal of Solar Energy Engineering. 2004;126:1034-40.

[152] Dolan DS, Lehn PW. Simulation model of wind turbine 3p torque oscillations due to wind shear and tower shadow. Power Systems Conference and Exposition, 2006 PSCE'06 2006 IEEE PES. September 2006;21:2050-7.

[153] Chattot J-J. Tower shadow modelization with helicoidal vortex method. Computers & Fluids. 2008;37:499-504.

[154] Fadaeinedjad R, Moschopoulos G, Moallem M. The impact of tower shadow, yaw error, and wind shears on power quality in a wind–diesel system. IEEE Transactions on Energy Conversion. 2009;24:102-11.

[155] Bayındır C. Compressive spectral method for the simulation of the nonlinear gravity waves. Scientific reports. 2016;6:22100.

[156] Slunyaev A, Kokorina A. Soliton groups as the reason for extreme statistics of unidirectional sea waves. arXiv preprint arXiv:170400804. 2017.

[157] Raed K, Karmakar D, Soares CG. Long-term assessment of the wave load acting on semi-submersible wind turbine support structure. Proceedings of the 3rd

International Conference on Maritime Technology and Engineering. Lisbon, Portugal,: Maritime Technology and Engineering III; 4-6 July 2016.

[158] Dematteis G, Grafke T, Vanden-Eijnden E. Rogue Waves and Large Deviations in Deep Sea. arXiv preprint arXiv:170401496. 2017.

[159] Kim E, Manuel L, Curcic M, Chen SS, Phillips C, Veers P. On the Use of Coupled Wind, Wave, and Current Fields in the Simulation of Loads on Bottom-Supported Offshore Wind Turbines during Hurricanes: March 2012-September 2015. National Renewable Energy Lab.(NREL), Golden, CO (United States) Technical Report, NREL/TR-5000-65283; ,June 2016.

[160] Guo Y, Keller J, La Cava W, Austin J, Nejad A, Halse C et al. Recommendations on Model Fidelity for Wind Turbine Gearbox Simulations: Preprint. the Conference for Wind Power Drives (CWD),Aachen, Germany: National Renewable Energy Laboratory (NREL), Golden, CO. ,Conference Paper, NREL/CP-5000-63444; March 3–4, 2015.

[161] Jonkman JM, Butterfield S, Musial W, Scott G. Definition of a 5-MW reference wind turbine for offshore system development. National Renewable Energy Laboratory Golden, CO, USA,Technical Report, NREL/TP-500-38060 February 2009.

[162] Turi MB, Marks CS. Bearing selection techniques as applied to mainshaft direct and hybrid drives for wind turbines. The Timken Company Publishing, Technical Paper; September 2010.

[163] Ragheb A, Ragheb M. Wind turbine gearbox technologies. Nuclear & Renewable Energy Conference (INREC), 2010 1st International. Amman, Jordan21-24 March 2010.

[164] Ishida Y, Yamamoto T. Linear and nonlinear rotordynamics: a modern treatment with applications. Weinheim, Germany John Wiley & Sons; 2013.

[165] Bouheraoua M, Wang J, Atallah K. Rotor Position Estimation of a Pseudo Direct-Drive PM Machine Using Extended Kalman Filter. IEEE Transactions on Industry Applications. 2017;53:1088-95.

[166] McDonald A, Bhuiyan NA. On the optimization of generators for offshore direct drive wind turbines. IEEE Transactions on Energy Conversion. 2017;32:348-58.

[167] Poore R, Lettenmaier T. Alternative Design Study Report: WindPACT Advanced Wind Turbine Drive Train Designs Study; November 1, 2000--February 28, 2002. National Renewable Energy Laboratory (NREL), Golden, CO.Subcontractor report, NREL/SR-500-33196 2003.

[168] Fingersh L, Hand M, Laxson A. Wind turbine design cost and scaling model. National Renewable Energy Laboratory (NREL), Golden, CO. Technical Report, NREL/TP-500-40566 December 2006.

[169] Malcolm D, Hansen A. WindPACT turbine rotor design study. National Renewable Energy Laboratory, Golden, CO, Subcontract Report, NREL/SR-500-32495 Revised April 2006

[170] Li HJ, Hu S-LJ, Jakubiak C. H 2 active vibration control for offshore platform subjected to wave loading. Journal of Sound and Vibration. 2003;263:709-24.

[171] Ditlevsen O. Stochastic model for joint wave and wind loads on offshore structures. Structural Safety. 2002;24:139-63.

[172] Arany L, Bhattacharya S, Hogan S, Macdonald J. Dynamic soil-structure interaction issues of offshore wind turbines. Proceedings of the 9th international conference on structural dynamics, EURODYN2014. p. 3611-8.

[173] He W, Ge SS. Vibration control of a nonuniform wind turbine tower via disturbance observer. IEEE/ASME Transactions on Mechatronics. 2015;20:237-44.

[174] Géradin M, Rixen DJ. Mechanical vibrations: theory and application to structural dynamics. 2rd ed. New York, NY: John Wiley & Sons; 1997.

[175] Kirk C, Wiedemann S. Natural frequencies and mode shapes of a free–free beam with large end masses. Journal of Sound and Vibration. 2002;254:939-49.

[176] van der Tempel J, Molenaar D-P. Wind turbine structural dynamics–a review of the principles for modern power generation, onshore and offshore. Wind engineering. 2002;26:211-22.

[177] Yilmaz OC. The Optimization of Offshore Wind Turbine Towers Using Passive Tuned Mass Dampers. Masters Theses May 2014, - current 54. 2014.

[178] Goupee AJ, Koo BJ, Kimball RW, Lambrakos KF, Dagher HJ. Experimental comparison of three floating wind turbine concepts. Journal of Offshore Mechanics and Arctic Engineering. 2014;136:020906.

[179] Gueydon S, Weller S. Study of a floating foundation for wind turbines. Journal of Offshore Mechanics and Arctic Engineering. 2013;135:031903.

[180] Koo BJ, Goupee AJ, Kimball RW, Lambrakos KF. Model tests for a floating wind turbine on three different floaters. Journal of Offshore Mechanics and Arctic Engineering. 2014;136:020907.

[181] Ye K, Ji J. The effect of the rotor adjustment on the vibration behaviour of the drive-train system for a 5 MW direct-drive wind turbine. Proceedings of the Institution of Mechanical Engineers, Part C: Journal of Mechanical Engineering Science. 2018;232:3027-44.

Publications

International journal publications:

1) Ye K, Ji J. The effect of the rotor adjustment on the vibration behaviour of the drive-train system for a 5 MW direct-drive wind turbine. *Proceedings of the Institution of Mechanical Engineers*, *Part C: Journal of Mechanical Engineering Science*. 2018, vol.232, pp.3027-44.
2) Ye K, Ji J. Natural Frequency Analysis of a Spar-Type Offshore Wind Turbine Tower With End Mass Components. *ASME Journal of Offshore Mechanics and Arctic Engineering.* 2018, vol.140(6), pp.064501-064501-5.
3) Ye, K. and Ji, J. Current, wave, wind and interaction induced dynamic response of a 5 MW spar-type offshore direct-drive wind turbine. *Engineering Structures*, 2019, vol.178, pp.395-409.

Manuscript under review:

1) "Overview of offshore direct-drive wind turbines and their related dynamic performances". (submitted)